Effect of Compressive Force on PEM Fuel Cell Performance

by

Colin Stephen MacDonald

A thesis
presented to the University of Waterloo
in fulfillment of the
thesis requirement for the degree of
Master of Applied Science
in
Mechanical Engineering

Waterloo, Ontario, Canada, 2009

Author's Declaration

I hereby declare that I am the sole author of this thesis. This is a true copy of the thesis, including any required final revisions, as accepted by my examiners.

I understand that my thesis may be made electronically available to the public.

Colin Stephen MacDonald

Abstract

Polymer electrolyte membrane (PEM) fuel cells possess the potential, as a zero-emission power source, to replace the internal combustion engine as the primary option for transportation applications. Though there are a number of obstacles to vast PEM fuel cell commercialization, such as high cost and limited durability, there has been significant progress in the field to achieve this goal. Experimental testing and analysis of fuel cell performance has been an important tool in this advancement. Experimental studies of the PEM fuel cell not only identify unfiltered performance response to manipulation of variables, but also aid in the advancement of fuel cell modelling, by allowing for validation of computational schemes.

Compressive force used to contain a fuel cell assembly can play a significant role in how affectively the cell functions, the most obvious example being to ensure proper sealing within the cell. Compression can have a considerable impact on cell performance beyond the sealing aspects. The force can manipulate the ability to deliver reactants and the electrochemical functions of the cell, by altering the layers in the cell susceptible to this force. For these reasons an experimental study was undertaken, presented in this thesis, with specific focus placed on cell compression; in order to study its effect on reactant flow fields and performance response.

The goal of the thesis was to develop a consistent and accurate general test procedure for the experimental analysis of a PEM fuel cell in order to analyse the effects of compression on performance. The factors potentially affecting cell performance, which were a function of compression, were identified as:

- Sealing and surface contact
- Pressure drop across the flow channel
- Porosity of the GDL

Each factor was analysed independently in order to determine the individual contribution to changes in performance.

An optimal degree of compression was identified for the cell configuration in question and the performance gains from the aforementioned compression factors were quantified. The study provided a considerable amount of practical and analytical knowledge in the area of cell compression and shed light on the importance of precision compressive control within the PEM fuel cell.

Acknowledgements

This work was supported by the Natural Sciences and Engineering Research Council of Canada. I would also like to thank my supervisor, Dr. Xianguo Li, for his guidance in the production of this thesis. Furthermore, I would like to thank Jae Wan Park for his tireless efforts to guide me in the fuel cell lab. Thank you to my family and brother for their encouragement through all of my endeavors. Most importantly, I would like to thank Lindsay Wood for her patience, understanding, and unwavering support throughout the completion of my degree.

Table of Contents

List of Figures

List of Tables

Nomenclature

A_c	Bipolar plate channel cross sectional area, m^2
a	Bipolar plate channel width, m
ar	Bipolar plate channel aspect ratio; (b/a)
b	Bipolar plate channel depth, m
C	Friction constant
Cu	Curvature ratio; (r_m/D_h)
D	Nominal bolt diameter, in
D_h	Hydraulic diameter, m
E_{rev}	Reversible cell potential, V
F	Faraday's constant, 9.6485309×10^4 C $mole^{-1}$
F_c	Clamping force, N
f	Friction coefficient
g	Acceleration due to gravity, m s^{-2}
$\Delta\bar{g}_f$	Gibbs free energy, J $mole^{-1}$
h_f	Head loss due to friction, m
h_m	Head loss due to minor losses, m
J	Current density, A m^{-2}
K	Minor loss coefficient
L	Bipolar plate channel length, m
L_s	Distance between consecutive channel bends, m
N	Number of bolts

$\dot{N}_{gas}$ Molar flow rate of gas,

$\dot{N}_{vap}$ Molar flow rate of vapour

n Number of electrons

P Pressure, kPa

P_f Pressure loss due to friction, Pa

P_{gas} Gas partial pressure

P_m Pressure loss due to minor losses

P_T Total mixture pressure

P_{TL} Total pressure loss

P_{vap} Vapour partial pressure

Q Volumetric flow rate, $m^3\ s^{-1}$

Re_{Dh} Reynold's number based on hydraulic diameter

r_m Mean channel bend radius, m

T Temperature, ˚C

V Average velocity, $m\ s^{-1}$

w Bipolar plate channel land width, m

Greek

ε Porosity

ε_k Porosity in phase k

μ Viscosity, $kg \cdot m^{-1} \cdot s^{-1}$

ρ Density, $kg\ m^{-3}$

Ψ_k General bulk property in phase k

Ψ_k^{eff} Effective general property in porous phase k

Chapter 1
Introduction

The transportation sector is a vital component to North American society. Currently the majority of transportation is powered by the internal combustion engine, run on fossil fuel derivatives. In recent years, a heightened awareness of the environmental impact of carbon emissions, combined with growing energy demands and the finite supply of fossil fuels have sparked the need for a zero-emission vehicle. There exist two options that meet the power requirements for such a vehicle, batteries and fuel cells. Though both satisfy the zero-emission condition, at point of operation, batteries have the disadvantage of long recharge times and limited driving range. Only fuel cells have the ability to match the convenience and range of internal combustion power train vehicles [1].

Though many types of fuel cells exist, the proton exchange membrane (PEM) fuel cell is best suited for transportation applications [2]. Their low temperature operation, in the range of 70-80 ˚C, allows for quick start times, comparable to those of the internal combustion engine. While the solid polymer electrolyte construction makes the cell mechanically robust, allowing for movement while eliminating the risk of electrolyte leakage. The PEM fuel cell also delivers net power density comparable to that of the internal combustion engine, with values of 1.13 kW/L reported by manufacturers [3]. However, there exist a number of factors inhibiting vast commercialization of this technology, one of the foremost being the lack of a hydrogen refuelling infrastructure. Refuelling stations in Canada are currently limited to the Hydrogen Highway, in lower mainland BC [4]. Other inhibiting factors are those associated with the fuel cell construction itself, specifically increasing durability and performance while reducing cost. These challenges must be met before fuel cell technology will become commercially competitive [5].

Much of the recent work in the advancement of fuel cell technology has focused on the fuel cell computational model. Advancements from Rowe and Li [6] and Baschuk and Li [7] and their consistent and systematic approach to mathematical modelling, has allowed for

better understanding of the immeasurable phenomenon within the restricted confines of the PEM fuel cell. However, mathematical and empirical models have their limitations. Due to the vast number of mass transfer and electrochemical processes occurring within the cell, it is difficult for one to develop an all encompassing model without first prioritizing these processes followed by the simplification or elimination of those found to be of less significance. Through this process, one tends to lose sight of the bigger picture of overall fuel cell improvement, as the focus is on singular fuel cell process simulation. As well, while in some cases the simplification can lead to an elegant design, as in the case of Baschuk and Rowe, it can also lead to a crude, inaccurate offering, which emphasizes unimportant phenomenon. Experimental studies of the PEM fuel cell are essential, not only in identifying unfiltered performance response to manipulation of variables, but also in the advancement of fuel cell modelling, by allowing for validation of their schemes.

While individual fuel cell component design has received much attention, such as flow channel layout and GDL construction, very little attention has been paid to the manner in which these components are assembled or compressed. Compressive force can play a significant role in how affectively these components function, the most obvious example being to ensure proper sealing within the cell. For these reasons an experimental study was undertaken, with specific focus placed on cell compression in order to study its effect on reactant flow fields and performance response. This chapter will elaborate on the goals of this thesis research and provide an outline for the document itself. First, background on the function of a PEM fuel cell will be provided, with insight into factors affecting performance.

1.1 Background

The PEM fuel cell is an electrochemical device that converts chemical energy of reactants, both fuel and oxidant, directly into electrical energy [2]. The fuel for the cell is pure hydrogen while the oxidant is oxygen, provided in the form of air or pure oxygen. A PEM fuel cell contains two bipolar plates, or flow plates, and a single membrane electrode assembly (MEA), as illustrated in Figure 1.1. The function of the bipolar plates is to deliver

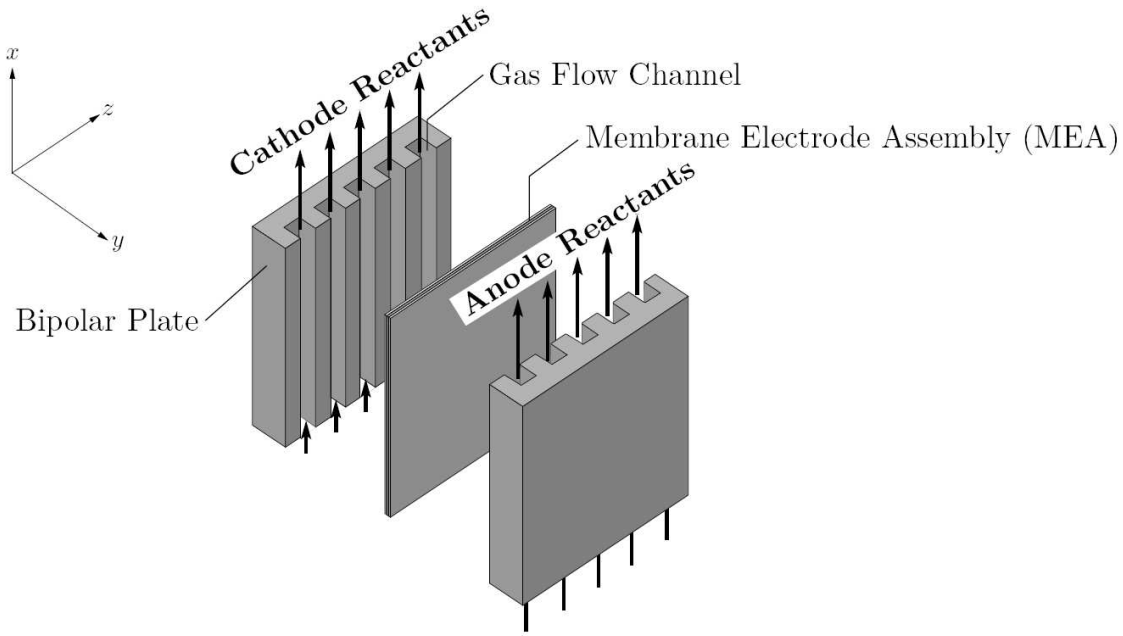

Figure 1.1: Simple representation of the PEM fuel cell construction

the cathode and anode reactant flows through their respective channels while also allowing for current conduction away from the reaction surface. For this reason the plates are made from an electrically conductive material, typically graphite or metal. The flow channel is rectangular and is approximately 1 mm in width and depth, or smaller. The channel layout has a number of common configurations, including serpentine, interdigitated, and parallel [8]. The channels are laid out in a manner so as to ensure that the reactants will be distributed evenly over the reactant surface. The electrochemical reaction, which generates the electricity extracted from the fuel cell, occurs within the MEA. The MEA consists of five layers; two gas diffusion layers (GDL), or porous electrodes, two catalyst layers, and the polymer electrolyte membrane layer, as illustrated in Figure 1.2. While the catalyst and electrolyte layers are almost always fastened to one another, the GDL can be fastened or is frequently provided as a separate entity within the cell. The gas diffusion layers, as the name suggests, facilitate mass transfer from the flow channel to the catalyst layer, the reaction site. In addition, the gas diffusion layer is the electrical conductor that transports electrons to and

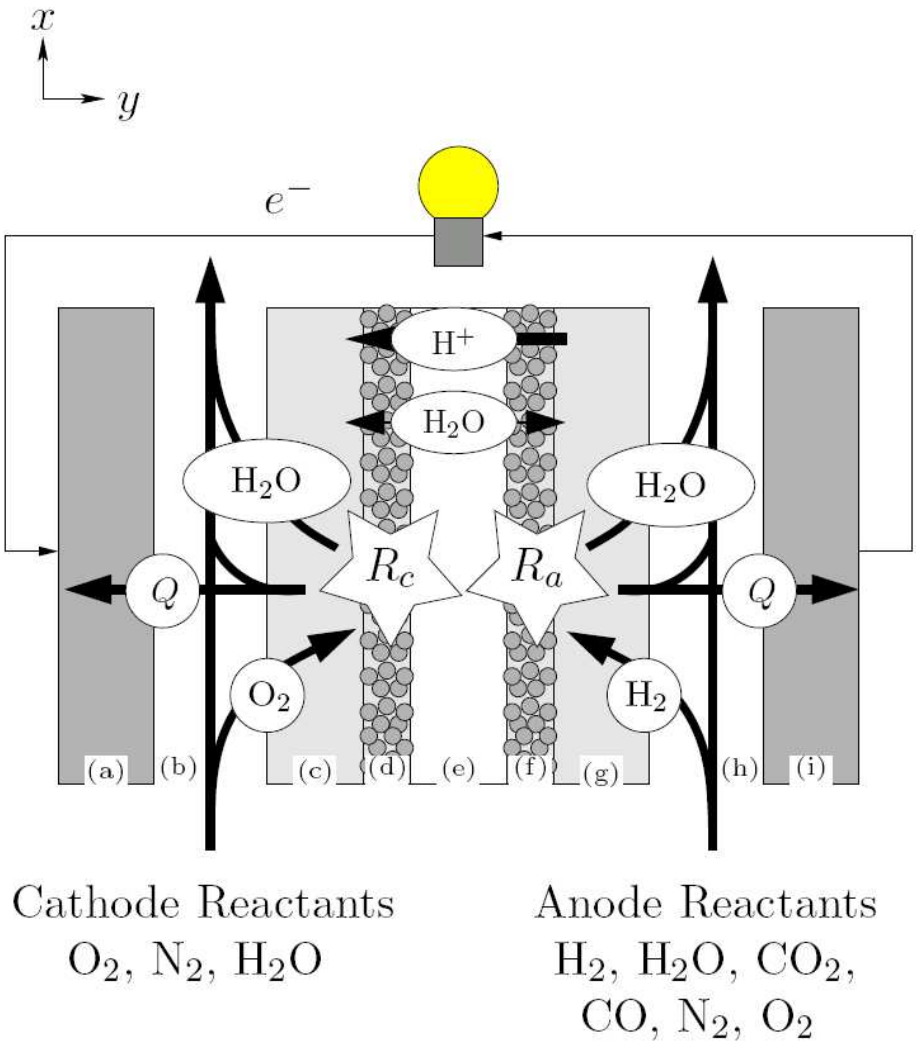

Figure 1.2: The components of a PEM fuel cell and the processes occurring within each component. The PEM fuel cell is composed of the (a) cathode bipolar plate, (b) cathode gas flow channel, (c)cathode electrode backing layer, (d) cathode catalyst layer, (e) polymer electrolyte membrane layer,(f) anode catalyst layer, (g) anode electrode backing layer, (h) anode gas flow channel, and (i) anode gas flow channel.[7]

from the catalyst layer. Typically, diffusion layers are constructed from porous carbon paper, or carbon cloth, with a thickness in the range of 100–300 μm. The gas diffusion layer also assists in water management by allowing an appropriate amount of water vapour to reach, and be held at, the membrane for hydration. These layers are also typically designed

to be hydrophobic and are treated with a polytetrafluoroethylene (PTFE or Teflon) coating to ensure that the pores of the GDL do not become congested with liquid water [9]. The catalyst layer is a carbon film (Vulcan X-72 and Vulcan 72) laced with platinum or platinum alloys, referred to as carbon-supported platinum catalysts [2]. The platinum loading is typically below 0.4 mg Pt/cm^2, with values reported as low as 0.014 mg Pt/cm^2 attained through the use of sputtering techniques [9]. However, considering practical fabrication process of MEAs, platinum loading of 0.1-0.2 mg Pt/cm^2 is desirable to maintain good repeatability of the membranes [2, 10]. The anode and cathode catalyst layers are divided by the electrolyte membrane layer. The polymer electrolyte membrane facilitates the transfer of the positive ions from the anode to the cathode and is made of a sulfonated fluoropolymer, similar to Teflon. The layer also serves as a barrier to the transfer of electrons, which are forced away from the anode catalyst layer, through the current collection pathway, to the cathode catalyst layer. In order for proton conduction to occur the membrane layer must be humidified. The hydrogen protons become mobile only after bonding to water molecules, becoming hydronium ions. Hydronium ions are then capable of moving between the sulfonic acid sites, through the membrane. The most commonly employed polymer electrolyte membrane is Nafion, manufactured by DuPont.

The net fuel cell reaction occurs in two parts with reaction sites at the anode and cathode catalyst layers. The reactions at these sites are referred to as half-cell reactions. The anode reaction is the oxidation of a hydrogen molecule into hydrogen protons and electrons, as illustrated in equation 1.

$$H_2 \rightarrow 2H^+ + 2e^- \tag{1}$$

Following the hydrogen oxidation reaction (HOR) the hydrogen protons are transported through the electrolyte layer while the electrons are forced to travel an external electrical circuit. At the cathode half cell reaction site, an oxygen molecule is reduced to produce a water molecule, as illustrated in equation 2. This half cell reaction is referred to as the oxygen reduction reaction (ORR).

$$\frac{1}{2}O_2 + 2H^+ + 2e^- \rightarrow H_2O_{(\ell)} \tag{2}$$

The combination of the two half cell reactions, the HOR and the ORR, results in the overall PEM fuel cell reaction, provided in equation 3.

$$\frac{1}{2}O_2 + H_2 \rightarrow H_2O_{(\ell)} + Heat + Electrical\ Energy \tag{3}$$

The reversible cell potential for the full cell reaction is 1.229 V, and is determined as a function of Gibbs free energy, as illustrated in equation 4.

$$E_{rev} = -\frac{\Delta\bar{g}_f(T,P)}{nF} \tag{4}$$

However, due to the presence of a number of irreversibilities, the cell does not operate at this reversible potential. Figure 1.3 displays a comparison of the cells reversible potential and the potential, or polarization curve, of a typical PEM fuel cell. It can be seen that potential is a function of the current drawn, or current density, while the reversible potential is independent of the current density, as it is constant over the entire domain.

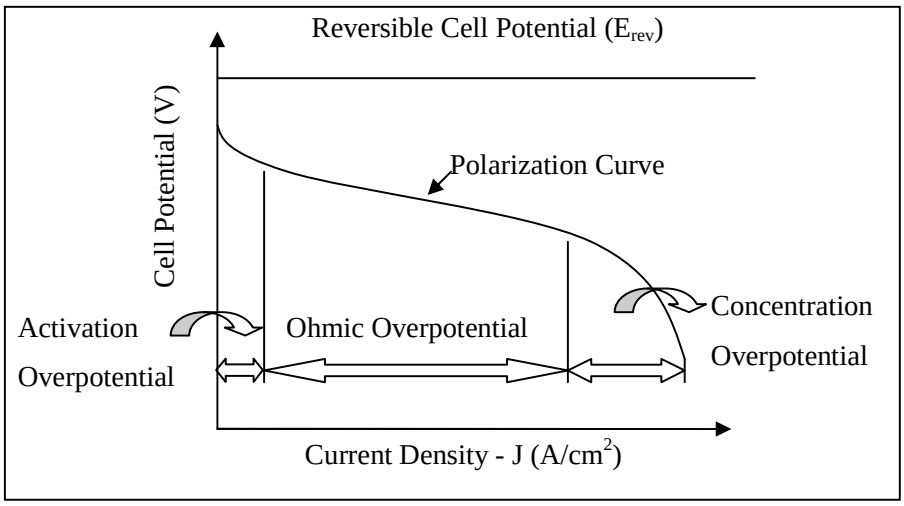

Figure 1.3: Polarization curve for a typical PEM fuel cell illustration reversible cell potential and sources of over potential

As current is initially drawn, in the low current density portion of the curve, losses are due to activation overpotential. Activation overpotential is caused by the slow moving reactions on the electrode surfaces. Since these reactions do not occur readily, a proportion of the voltage generated is lost as these electrochemical reactions are driven from equilibrium. This voltage drop, as illustrated in Figure 1.3, is highly non-linear.

As the electrical current load increases, activation overpotential is less of a factor and ohmic losses increase at a greater rate, the curve enters the region characterized by ohmic overpotential. This voltage loss is caused by the resistance to the flow of electrons through the material of the electrodes and the various connections in the current collection pathway, as well as the resistance to the flow of ions through the electrolyte. These losses are proportional to current density, and are essentially linear.

The high current density voltage losses in the cell can be mainly attributed to concentration overpotential. This rapid voltage drop is cause by a depletion of the half cell reactants in the vicinity of the active reaction sites as mass transport is limited. The mass transport limitations are due to diffusion limitations in the electrode backing and catalyst layers, and the phenomena of water flooding. At high current densities, the amount of water produced at the cathode catalyst layer is greater than the amount that can be removed by the flow moving through the flow plate channel. The accumulation of liquid water in the porous diffusion layer limits the amount of oxygen that can reach the reaction surface, effectively choking the ORR.

1.2 Thesis Objectives and Outline

The performance of a PEM fuel cell is dependent on its response to activation, ohmic, and concentration polarization. These losses can be directly linked to varying electrical and mass transfer properties of cell components in the MEA. While proper design of these components is an important factor in obtaining optimal operational conditions, once in the cell, the degree of compression can significantly affect their properties and the resultant

performance response. The overall goal of this thesis research was to perform an experimental analysis on fuel cell performance, with emphasis on cell compression and its effect on performance and flow field response.

Specifically the thesis objectives were identified as follows

- To develop a consistent and accurate general test procedure for the experimental analysis of a PEM fuel cell
- To determine the general effect of varying degrees of compression on PEM fuel cell performance and identify factors contributing to this performance response
- To develop a precise compression testing technique that would allow for the isolation of the factors contributing to variation in performance response
- To determine the individual effect of each contributing factor on PEM fuel cell performance with the goal of identifying the dominant limiting parameter in the cell performance as a result of compression
- To determine the sensitivity of compression related performance response to changes in catalyst platinum loading.

Through these objectives this study offers insight into the compression related performance response, while also enabling the progression of PEM fuel cell development toward the ultimate goal of vast commercialization.

Chapter 2 summarizes the studies, currently present in literature, that analyze the effects of compression on PEM fuel cells. Chapter 3 will systematically present the experimental apparatus used, as well as the techniques applied in this study. Chapter 4 presents and discusses the results of the experimental testing. The thesis conclusions are summarized in chapter 5. Chapter 6 provides recommendations, which include design modifications and concepts to be studied in future work.

Chapter 2
Literature Review

Over the past two decades, significant efforts have been made to investigate PEM fuel cells as a possible zero emission power source for transportation applications. A vast number of research studies were undertaken in the hopes of improving PEM fuel cell performance, with the ultimate goal of advancing the system to a point where it can compete with the internal combustion engine. Experimental testing has played a considerable role in this advancement. These experimental studies, through the optimization of fuel cell components and operating conditions, have improved power density while reducing cost. Before one can identify an area of potential research one must first be fully aware of the current state of PEM fuel cell research. Also, knowledge of these works is critical in order to identify key variables affecting cell performance. This chapter will present several of these works, from published literature, and establish the current state of PEM fuel cells. In addition, the limitations of these works and areas requiring further investigation will be established.

2.1 Operating Conditions

A significant amount of fuel cell research has focused on optimising the operational conditions of the cell. These conditions include temperature, reactant pressure, relative humidity and stoichiometry. Manipulating cell operating temperature has been found to have a considerable effect on cell performance. Paganin et al. [11] studied the performance of an experimental fuel cell assembly over the temperature range of 50-80 ˚C. It was found that an increase in temperature resulted in increased performance. This performance increase was in both the ohmic and concentration overpotential region. The ohmic gains were quantified through a measurement of cell resistance, defined as the total current resistance that all cell components contribute to. The increase in temperature was found to drastically reduce this resistance. While the concentration polarization gains were a result of

the decrease in flooding within the cell. The increase in temperature resulted in higher vapour capacity within the cell, thus evaporating excess water and drastically increasing supply of reactants, which resulted in an increase in the limiting current density. A number of other studies including those performed by Jang et al. [12] and Q. Yan et al. [13] as well as others [14, 15] confirmed the performance findings of Paganin et al. [11] in that temperature range. The performance gains in the concentration overpotential region, due to an increase in temperature, were also examined by Sakai et al. [16 17] and K. Broka and P. Ekdunge [18]. These studies focused on the impact of a temperature increase on O_2 permeability in the Nafion membrane. It was found, in both these studies, that for consistent relative humidity an increase in temperature resulted in a significant increase in O_2 permeability, which also contributes to an increase in the limiting current density. While in this moderate temperature range, 50-80 ˚C, increase in temperature was found to have a positive impact on performance, excessive cell operating temperature has been found to have a detrimental effect. Williams et al. [19] investigated the resultant cell performance beyond this temperature range, in the region of 80-120 ˚C. It was found that excessive temperature increase, into this range, had a negative impact on PEM fuel cell performance. This drop in performance was attributed to a resultant decrease in relative humidity. As was previously mentioned, when cell temperature increased, the vapour capacity of the reactant flows would also increase, in other words, the relative humidity of the reactant flows would decrease. Should the capacity reach an excessive level, resulting from temperatures exceeding 80 ˚C, the reactant flows would extract moisture from the membrane layer, inhibiting reactant permeability and proton transfer.

The operating conditions within a cell are often dependent on one another, as was illustrated with relative humidity and temperature, as is the case with most phenomena involving ideal gas flows. A decrease in the relative humidity of the reactant flows, as a result of temperature increase, was found to negatively impact cell performance. A number of studies have analysed the impact of changing relative humidity of the reactant flows, independent of temperature change, including Q. Yan et al. [13]. This study examined the changes in performance over a relative humidity domain of 70-100% for the anode side and

10-100% for the cathode side. It was found that fully humidified reactant streams resulted in the highest peak performance. It was also found that at lower cell temperature operation, below 75 ˚C, the fully humidified flows supplied the highest peak performance, but they also resulted in a drop in limiting current density when compared to lower humidification levels, specifically 70 and 80%. However, this was not the case for higher cell temperature operation, which displayed highest peak power output as well as maximum limiting current density. The drop in limiting current density was attributed to liquid water build up from the condensation of the humidified reactant flows when they came into contact with the cell, operating at a lower temperature. These findings were confirmed by Nguyen and White [20] through modelling and experimental techniques as well as several others [12, 14, 21].

The effect of reactant flow pressures on cell performance has also been studied in depth. Larminie and Dicks [22] present a theoretical argument that the increase in partial pressure of the reactant flow will result in an increase in the reactivity of the gas, therefore increasing cell potential. This derivation was performed through a manipulation of the Nernst equation. However this increase was quantified to be small in scale for even large increases in pressure. Paganin et al. [11] experimentally confirmed this Nernst relationship between reactivity and pressure. It was found that an increase in pressure resulted in an increase in open circuit voltage and limiting current density for the experimental cell assembly. This increase was from anode/cathode pressure of 1/1 atm to 2/5 atm. Practical studies have found that an increase in pressure can have other secondary positive performance effects, beyond reactant activity. Bernardi and Verbrugge [23] studied the water transport properties of a PEM fuel cell. It was presented that an increase in flow pressure, while imposing a gradient between the anode and cathode, with the cathode experiencing higher pressure, would encourage the transport of water across the Nafion membrane to the anode side. This improved water management technique, which humidified the anode side of the membrane and reduced water build-up on the cathode side, was found to improve limiting current density. Squadrito et al. [24] examined this water transport and performance response to pressure. This study confirmed the findings of Paganin and Bernardi and also identified a temperature dependence on this water transport phenomenon, suggesting that at elevated

temperature, the evaporation of membrane moisture is the dominant factor and the pressure gradient cannot overcome this phenomenon. In all these studies the performance of the cell was more sensitive to increases in O_2 pressure as opposed to increases in H_2 supply pressure. Also in these cases it was presented that the marginal increase in performance would not be sufficient to satisfy the increase in parasitic load due to elevated pumping power requirements. No general consensus has been reached with regards to optimal pressure settings.

The concentration of the reactants supplied, commonly referred to as stoichiometry, can also have an effect on the performance of the PEM fuel cell. Li [2] presents theory that losses due to decreasing reactant concentration in the fuel cell can incur significant performance losses. These losses arises from the fact that cell potential will adjust to the lowest electrode potential given by the Nernst equation for the various reactant compositions at the exit of the anode and cathode channels. This loss, also referred to as Nernst loss can be quantified through a modified form of the Nernst equation, presented in equation 5.

$$\eta_N = \frac{RT}{nF} \ln \frac{K_{out}}{K_{in}} \tag{5}$$

Nernst loss is dependent on flow channel alignment as well as total reactant consumption. Should the flow channels be aligned such that both the anode and cathode outlets are in the same vicinity, this would maximize Nernst losses. In addition this equation reveals that should the reactants be fully consumed, the Nernst loss would be extremely large, approaching infinity. A stoichiometry of 1.2 for H_2 supply and 2 for O_2 supply should be used in typical operation to prevent these losses. The stoichiometry number represents the ratio of molar flow rate supplied to the cell versus the flow rate consumed in the cell. Practical studies by Jang et al. [12] and others [14, 15] found little benefit to increasing the stoichiometry beyond this value for static load conditions. Dynamic load studies by Qu et al. [25] and Kim et al. [26] present that for lower stoichiometries or ‘starved’ conditions, the cell displays poor dynamic load response compared to cases where excess reactant stoichiometries were provided.

2.2 Component Optimization

A significant number of studies have focused on the optimization of the design of individual cell components. Components of greatest interest are the MEA, GDL, and bipolar plate. This section will summarize the studies presented in literature dealing with the optimization of these components and the findings there in.

The bipolar plate is a vital component of PEM fuel cells, as it provides fuel and oxidant flow to the reaction surface, removal of the reaction products, current collection and mechanical support for the cells in the stack. Bipolar plates constitute more than 60% of the weight and 30% of the total cost in a fuel cell stack. For this reason, the weight, volume and cost of the fuel cell stack can be reduced, significantly, by optimizing the layout configuration of the flow field and use of lightweight materials. Different combinations of materials, flow-field layouts and fabrication techniques have been developed for these plates to achieve the aforementioned functions efficiently, with the aim of obtaining, both, performance and economic gains [8]. While resin impregnated graphite is the most commonly used bipolar plate material, its brittle nature and lack of mechanical strength combined with relatively poor cost effectiveness for large volume manufacturing make it a less than ideal option [8, 27]. Alternatives to this material have been investigated in depth. Metals as a bipolar plate material have received much attention as of late, however due to their highly reactive nature, and resultant susceptibility to corrosion, coatings and treatments are required [27]. Woodman et al. [28] claim a 60% reduction of mass and 56% reduction in thickness through the application of corrosion resistant, coated aluminium bipolar plates. Other proposed bipolar plate materials include titanium, chromium, stainless steel, and niobium [29-32].

In an attempt to optimize reactant distribution various, bipolar plate, flow field layouts have been investigated. Earlier attempts at flow channel designed involved mostly a straight channel orientation, as was presented by Pellegri and Spaziance [33] with their parallel straight channel flow field. These straight designs had a number of shortcomings, including flow stagnation points, leading to water build-up, and inadequate pressure drop, resulting in

poor reactant distribution. To remedy this Watkins et al.[34, 35] developed a continuous style flow channel, referred to as a serpentine design. This channel allowed for better water management as a result of the increased pressure drop. Also this layout resulted in as much as a 50% increase in power output. This layout has further been modified to include parallel cooling circuits, as presented by Fletcher et al. [36] and segmented serpentine circuits which allow for better reactant distribution, as presented by Cavalca et al. [37].

The design of a complete membrane electrode assembly, including GDL, is a delicate balancing of transport media. Conductance of gas, electrons, and protons must be optimized to provide efficient transport to and from the electrochemical reactions [9]. Optimization of the MEA can be difficult as isolation of a single parameter is near impossible, as these transport mechanisms are oft dependent on one another. However a number of general developments have been made in membrane design. Paganin et al. [11] present a study analyzing three Nafion membrane thicknesses. The three membranes analyzed were Nafion 112, 115, and 117 with respective thicknesses of 50, 125, and 175 μm. It was found that the thinnest membrane, Nafion 112, provided the best cell performance, offering both lower resistance and increased limiting current density than its two counter parts, Nafion 115 and 117. These findings were further validated in a study presented by Akalycin and Kaytakoglu [38]. Also, as was previously stated, reactant humidification is a key factor in optimizing membrane layer functionality. In order to optimize both reactant permeability and proton transport the membrane requires humidification. This is achieved by fully humidifying reactant flows [12-14, 21, 39]. Paganin et al. [11] also investigated the effect of platinum loading on cell performance, citing optimal parameters of 20 Wt% Pt/C while revealing a trend of increasing performance for increasing platinum loading, a function of platinum distribution per unit surface area, with the units mg Pt/cm^2.

While increased platinum loading results in increased performance, much of the research in the field of catalysts has been aimed towards the reduction of this loading. The emphasis has been on efficient platinum distribution techniques in order to reduce overall fuel cell costs. It has been found that reducing this loading can significantly reduce economic barriers while minimally reducing cell performance. The platinum loading is typically

below 0.4 mg Pt/cm^2, with values reported as low as 0.014 mg Pt/cm^2 attained through the use of sputtering techniques and the use of carbon support particles [9, 40, 41]. However, considering practical fabrication process of MEAs, platinum loading of 0.1-0.2 mg Pt/cm^2 is desirable to maintain good repeatability of the membranes [2, 10].

Another factor affecting catalyst function is carbon monoxide (CO) poisoning. PEM fuel cell performance degrades significantly when CO is present in the fuel gas. The CO consumes active catalyst layer sites and therefore inhibits the hydrogen oxidation reaction on the anode side. Oetjen et al. [42] found that even small CO concentrations in the fuel supply resulted in a significant drop in cell performance. There are several affective methods to mitigate CO poisoning. One such method is the application of platinum alloys to promote CO oxidation. Oetjen et al. [42] and Schmidt et al.[43] both found that the use of platinum-ruthenium (Pt-Ru) alloy in the catalyst layer improved performance considerably for fuel cells with a H_2/CO fuel source. The presence of the Ru results in the formation of a water derived hydroxide (OH) group. This OH group can then be used to oxidize the CO to CO_2, effectively cleaning the catalyst surface. A second technique that has been affective at improving CO tolerance is the operation of the fuel cell at elevated temperatures. Zawodzinski et al. [44] found that elevated temperatures, exceeding 100 ˚C, were equally as effective as the introduction of Ru at the mitigation of CO poisoning. The dependence of CO tolerance on cell temperature was explained by the strong temperature dependence of the adsorption equilibrium constant of CO on Pt. The Pt surfaces being freed from CO by either marginal thermal desorption or electrochemical oxidation rates explained the increase in tolerance with respect to the increased loading [45]. However this technique is not practical for CO tolerance in PEM fuel cells, as the increase in temperature results in membrane dehydration and poor cell performance. Introduction of oxygen into the fuel supply has also been found to improve CO tolerance. The presence of O_2 on the anode side has been found to accelerate the CO oxidation process. Gottesfeld and Pafford [46] found that with O_2 bleeding, the PEM fuel cell could tolerate CO concentrations of 500 ppm in the fuel supply. Another affective form of oxidation introduction is through the use of hydrogen peroxide

(H_2O_2) in the anode humidifier, as presented by Schmidt et al. [47]. This method has the added safety benefit of avoiding the potentially volatile H_2 and O_2 supply gas mixture.

The GDL also plays a complex, multifaceted role within the PEM fuel cell. Diffusion layers facilitate mass transfer, which includes both reactant and vapour flows, from the flow channel to the catalyst layer, the reaction site in the cell. In addition, the gas diffusion layer is the electrical conductor that transports electrons to and from the catalyst layer. The ability to effectively transport mass through the GDL is typically quantified using permeability. While there exist a number of studies that measured GDL permeability for the application in computational modelling, as presented by Gostick et al. [48] and Feser et al. [49], minimal experimental work has been presented on varying permeability and the resultant performance response. Williams et al. [19] studied some effects of varying GDL permeability and found weak proportionality between permeability and performance. However this study chose to vary permeability by changing the GDL media. This resulted in the influence of factors, such as polytetrafluoroethylene (PTFE) loading, and GDL fibre construction on the performance trend. An important recent advance in GDL technology is the use of a micro porous layer (MPL) on the catalyst side of the GDL. The MPL consists of carbon black powder and a hydrophobic agent. It has been reported that the MPL increases the catalyst utilization and the overall fuel cell performance depending on its structure [50-54]. Lin and Nguyen [54] found that the addition of a MPL on the GDL offered better fuel cell performance even when exposed to a lower air stoichiometry. To ensure proper mass transfer the diffusion layer must provide a clear transport pathway, as such, the effective function of the GDL depends on preventing liquid water build-up. To facilitate mass transfer and prevent water build up, diffusion layers are treated with a PTFE adhesive coating. Studies of the influence of this coating on cell performance found that the optimal loading value of PTFE was 15-30 Wt% [11, 52, 55, 56]. Poorer performance at higher PTFE was attributed to the lack of hydrophilic pathways in the diffusion layer, which prevented the flow of product water on the cathode side to the bipolar plate flow channel, resulting in electrode flooding.

2.3 PEM Fuel Cell Compression

Compression of the fuel cell can affect a number of operational parameters within the cell. The degree of cell compression controls the GDL thickness, contact resistance, and sealing force. Increased compressive force reduces the electrical contact resistance within the cell, through improved interfacial contact. It also increases the compression of silicone gaskets, thus increasing the sealing force at flow interfaces within the cell. Compression of the GDL can have a significant affect on its physical properties. Increasing the compressive force changes the porous structure within the GDL, reducing the proportion of void space. Gostick et al. [48] presented that this reduction of void space will change the diffusion properties of the cell as well as its electrical conductivity. The study found a consistent inverse proportionality between porosity and permeability values of the GDL. This trend was correlated by Tomadakis et al. [57] in a study of a multitude of porous materials. Given a known GDL structure Tomadakis could provide permeability as a function of porosity to within 25% of experimentally calculated values. Few studies have presented experimental data on compression. Barber et al [58] studied contact resistance for varying compressive load. It was found that surface contact was optimized at the maximum allowable compressive force. Chang et al. [59] also presented an experimental study in fuel cell compression but performance data was not generated. Contact resistance and conductivity were quantified for an irregular cell configuration. A number of computational studies on inhomogeneous GDL compression have been performed [60-63]. Zhou and Wu [63] analyzed the mass transfer properties of the GDL surrounding the land area in the bipolar plate. Due to the ribbed design of the flow plate, compression at excessive levels can lead to inhomogeneous compression of the GDL. The land area compresses the GDL while the channel offers no resistance; as a result the GDL protrudes into the channel cross-section. This formation was found to limit diffusive mass transfer and current density locally, at the point of over compression. However, these limitations were balanced by reactant cross flow, where excessive pressure gradient between adjacent channels resulted in the flow bypassing the channel through the GDL. This phenomenon encouraged convective mass transfer and promoted better reactant delivery [60, 63]. Lee et al. [64] and Ge et al. [65] presented GDL

compression studies, however these studies chose to operate their cells for extended periods, and introduce factors such as component degradation and excessive liquid water build-up. The trend of inverse proportionality between compression and performance could not be solely attributed to the compressive effects as it was also a function of time.

There clearly exists the need to perform a thorough PEM fuel cell compression study. This would allow for the study of all compression related parameters, including surface contact and sealing pressure, and their effect on fuel cell performance. This research would also allow for the investigation of GDL permeability and conductivity as a performance variable, independent of other GDL factors such as PTFE loading and fibre construction. This work would offer valuable insight into optimal compression techniques for fuel cell operation, as well, provide data to be applied to future computational models.

Chapter 3
Experimental Apparatus and Conditions

The experimental setup included a PEM fuel cell, with an active area of 100 cm^2, and test station. The cell was an in-house design and the specifications for all components, including bipolar plates, current collectors, MEA, end plates, and sealing media are presented in detail in this chapter. The test rig was a Fuel Cell Automated Test Station (FCATS), designed and constructed by Hydrogenics, Inc. This chapter will discuss the test station design and will offer an uncertainty analysis of the data collected. To ensure consistent test conditions and repeatable results, a deliberate and precise assembly procedure was required for the test fuel cell. This chapter will present the assembly and disassembly techniques for all tested fuel cell configurations. Repeatable data also relies on a consistent test procedure. Identical test procedures were applied to each test cell assembly, which included three test phases. First, the integrity of the cell had to be ensured by testing for the presence of leakage. Once proper sealing had been established the flow field of the cell was analysed by the investigation of flow channel pressure drop data. The final phase was the performance test, where cell potential data was collected for a consistent current density domain. The detailed methodology of the three test phases will be presented in this chapter.

3.1 Fuel Cell Components

Due to the large number of parts and layered construction of the PEM fuel cell, a great deal of precision was required in the design of the fuel cell components in order to ensure proper cell performance. This section will outline the design of the fuel cell used in the study and all of its components. The overall assembly presented was selected not only for its robust design, but to allow for the continuation of past experimental research. This specific assembly has been used in previous performance and flow tests presented in literature [15, 66]. As well, some of the components used in the assembly were provided at no cost, as part

of contractual agreements with the Fuel Cell and Green Energy Group, specifically the MEA, which provided significant economic incentive for their use. The complete PEM fuel cell assembly is depicted in Figure 3.1.

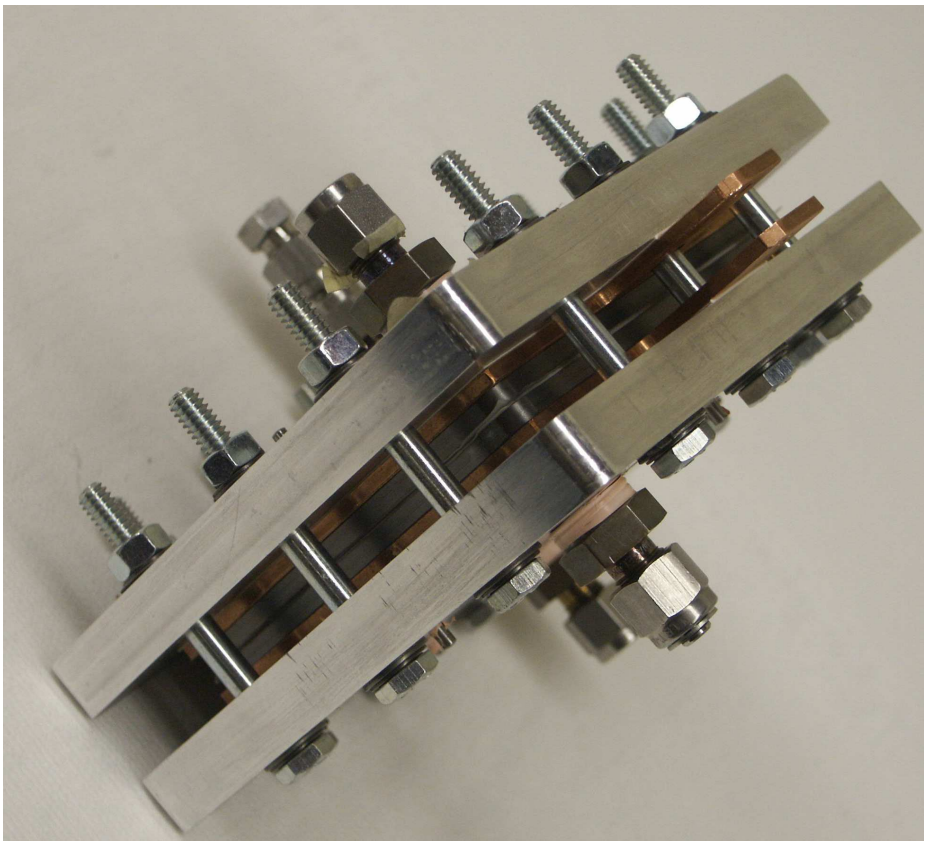

Figure 3.1: PEM fuel cell assembly

3.1.1 Bipolar Plate

The bipolar plates were machined from resin impregnated graphite plates. Though graphite is brittle and can be difficult to machine, it offers a number of desirable properties for a fuel cell flow channel material. The carbon structure is stable and is therefore resistant to corrosion in the hostile fuel cell operating conditions. Also, the material provides favourable electrical conduction, which is important for proper cell function as the flow plate is a component of the current collection pathway. In addition the graphite has a low density, and

therefore adds little weight to the overall assembly. Another option for bipolar plate was metal, specifically aluminium, titanium, or even stainless steel. Though steps have been taken to develop plates of these materials a number of obstacles are still present. Metal provides vastly superior electrical and thermal conductivity; however the production of an oxide layer on the plate surface of these metals drastically inhibits electron transfer, effectively increasing cell resistance. Efforts to create light weight metal alloys that have been processed so as to avoid this oxide build-up have proven to be expensive and have produced excessive pressure losses, such as perforated or foamed metal. An effective low-weight and low-cost metal bipolar plate has yet to be developed for commercial applications.

The bipolar plates were machined with a serpentine flow channel layout, as illustrated in Figure 3.2. The layout design has its advantages and disadvantages. The single channel construction creates a relatively long reactant flow path and therefore can result in substantial pressure drop and a large parasitic power load. However, the advantages are significant, as this channel arrangement has superior water management capabilities. The single serpentine flow field eliminates areas of stagnant flow that are pervasive in other flow channel layouts, such as the parallel or pin-type flow fields. The lack of flow stagnation eliminates liquid water build-up as all water droplets are forced through the channel to the flow field outlet [8]. In addition, the large pressure drop within the channel can aid in the removal of product water in vapour form. The relation of molar flow rate for water vapour and reactant gas is illustrated in equation 6 [8]. It can be seen from this equation that as total pressure decreases, the capacity for vapour flow rate increases. Should

$$\frac{\dot{N}_{vap}}{\dot{N}_{gas}} = \frac{P_{vap}}{P_{gas}} = \frac{P_{vap}}{P_T - P_{vap}} \tag{6}$$

sufficient pressure drop exist in the anode channel, this phenomenon has been found to draw water from the cathode side, through the membrane, to the anode flow channel, where it is exhausted from the cell and results in significantly improved performance at high current densities [67]. Table 3.1 summarizes the dimensions and flow parameters for the bipolar

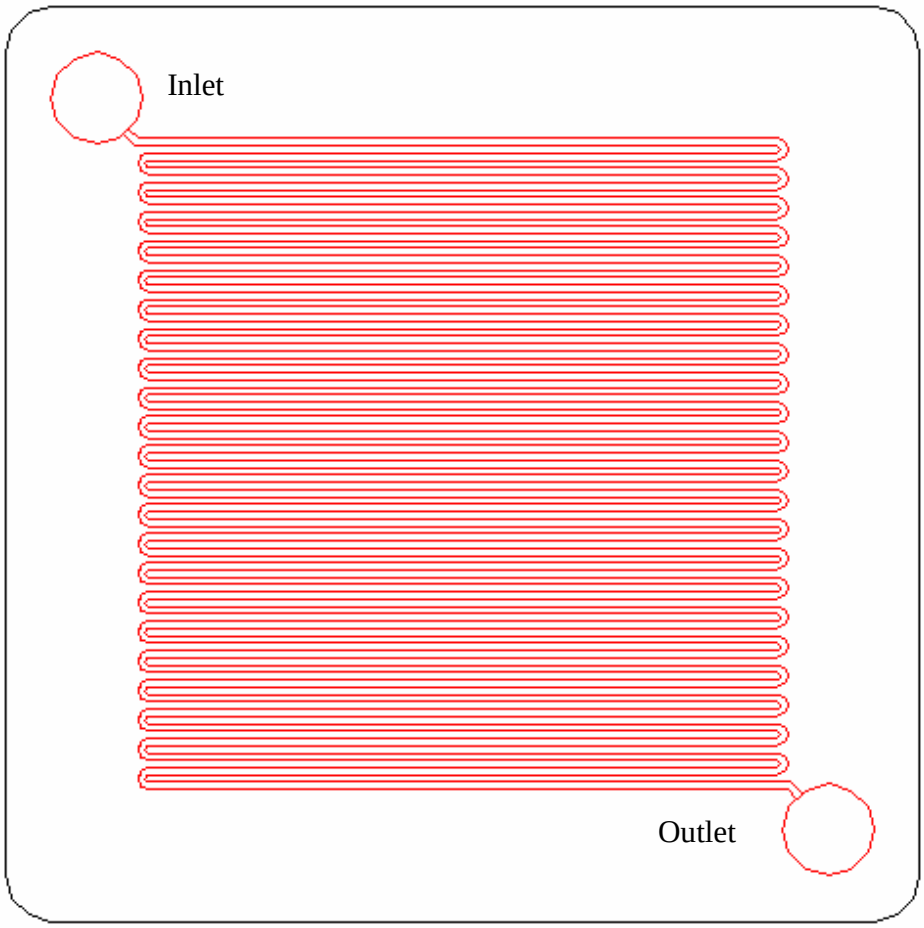

Figure 3.2: Bipolar plate serpentine flow channel layout

Table 3.1: Bipolar Plate Flow Channel Dimensions and Flow Parameters

Dimensions		Flow Parameters	
Width - a (mm)	1.0	Cathode Flow Rate (sccpm)	1994
Depth - b (mm)	1.1	Cathode Re_{Dh}	2110
Land Width - w (mm)	1.0	Cathode Entrance Length (mm)	133
Channel Length (m)	5.1	Anode Flow Rate (sccpm)	502
Number of Turns	50	Anode Re_{Dh}	724
		Anode Entrance Length (mm)	45

plate channel. The flow parameters are calculated at the current density of 0.6 A/cm^2. To allow for a general cell temperature measurement a 1/16 inch diameter hole was drilled into the top, inlet side, of the cathode bipolar plate. During cell operation the hole would be occupied by the cell temperature thermocouple and would allow for temperature regulation.

3.1.2 Membrane Electrode Assembly (MEA)

The membrane manufacturer, SolviCore, offered two electrode assembly constructions; a five layer MEA and a three layer MEA. Both constructions included a membrane layer and two catalyst layers. But the five layer construction included two, fastened gas diffusion layers, that were hot pressed to the membrane layer, while the three layer assembly required external gas diffusion layers to be placed on the MEA during the cell assembly process. Though the five layer MEA was initially supplied, ultimately the three layer MEA was selected for the final experimental cell configuration. The change in MEA was made following preliminary tests and the reasons behind this decision are presented in section 4.1. In this section the specifications for the three layer MEA will be presented.

The MEA, displayed in Figure 3.3, was manufactured using Nafion 115. Nafion is a sulfonated tetrafluorethylene copolymer created by DuPont. The naming convention for Nafion uses the equivalent weight, the weight of Nafion per mole of the sulfonic acid group, and thickness to distinguish between varying types. For this experiment, Nafion 115, describes Nafion containing 1100 g equivalent weight of Nafion at a thickness of 5 thousandths of an inch, or 127 μm. The catalyst layers were carbon supported platinum, with a platinum content of 0.4 mg Pt/cm^2 for both the anode and cathode catalyst. While virtually all of the MEAs were constructed with the 0.4 mg Pt/cm^2 a few assemblies with catalyst layers loaded at 0.2 mg Pt/cm^2 per electrode were also used in the study during the platinum loading sensitivity testing.

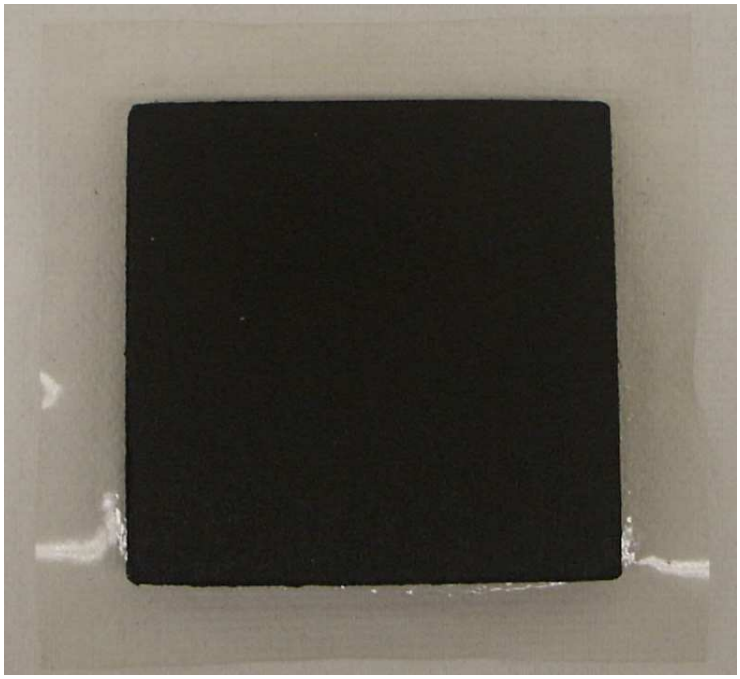

Figure 3.3: Membrane electrode assembly with 3 layer construction, Nafion 115 with 0.4 mg Pt/cm^2 per electrode

3.1.3 Gas Diffusion Layer (GDL)

The gas diffusion layers were also supplied by SolviCore. The GDLs were manufactured using carbon fibre filaments, 7 μm in diameter, arranged randomly in the surface plane and stacked through the GDL thickness, as illustrated in Figure 3.4. The carbon filament is bound using a carbon based adhesive and is coated with a 30 wt% PTFE treatment to make the porous layer hydrophobic. The surface in contact with the catalyst layer was coated with a microporous layer (MPL). The MPL consists of carbon black powder and approximately 10 wt% PTFE, which acts as a hydrophobic agent and to bind the powder. The porosity of the diffusion layer was given to be 78%, which is the ratio of void space to total GDL volume. The resistivity of the layer was provided as 80 mΩ-cm as determined through 4 point probe measurement. Due to proprietary reasons no other GDL properties were provided by the manufacturer. In order to gain further insight into the structure of the GDL scanning electron microscope (SEM) images were captured for both the carbon fibre layer

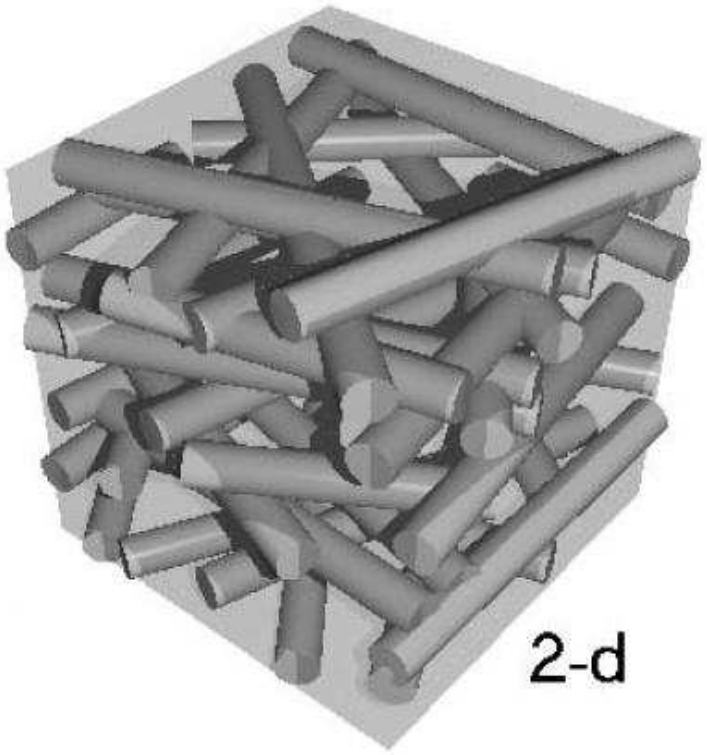

Figure 3.4: GDL filament arrangement with two dimensional random fibre structure [57]

and the MPL, as illustrated in Figures 3.5 - 3.8. The GDL material was supplied in large 30 x 30 cm sheets and individual GDLs used in the cell assembly were cut from these sheets. Templates were designed to ensure identical GDL dimensions for all cases. The individual layers were designed to be square with dimensions of 105 x 105 mm. These dimensions would allow for the diffusion layer to overhang the edge of the channel area by 2.5 mm, and would allow for a slight margin of error in the assembly procedure while maintaining complete coverage.

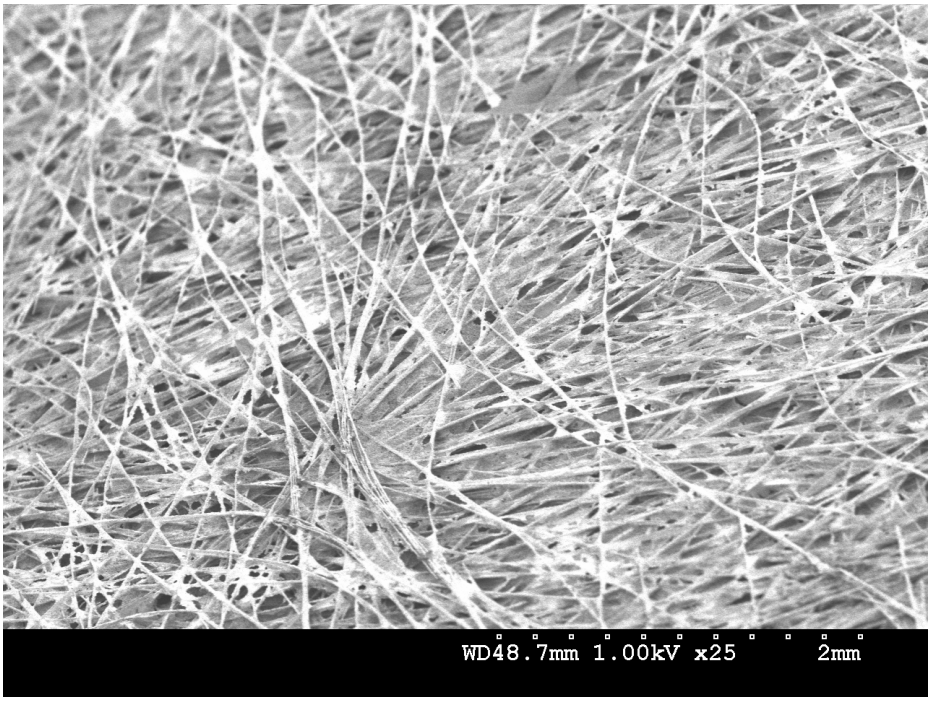

Figure 3.5: SEM image of GDL carbon fibre layer 25x magnification

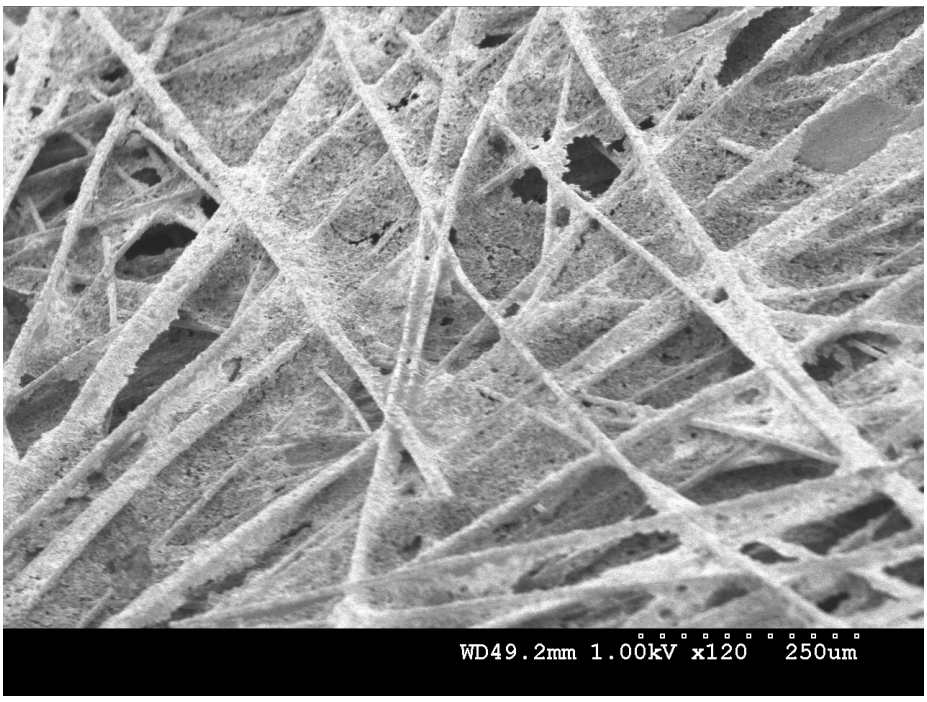

Figure 3.6: SEM image of GDL carbon fibre layer 120x magnification

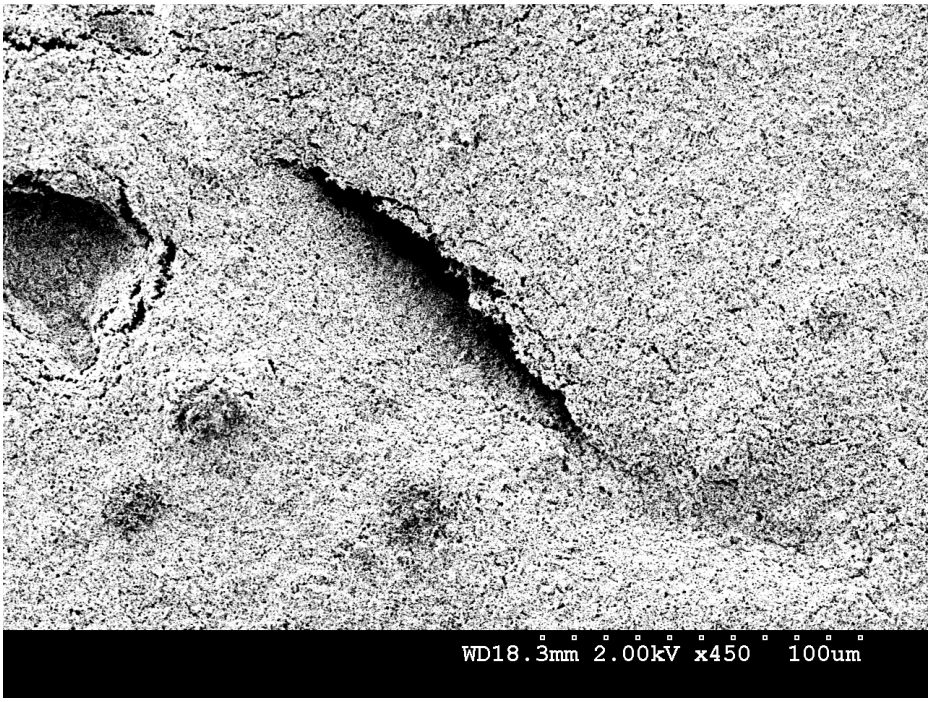

Figure 3.7: SEM image of GDL MPL 450x magnification

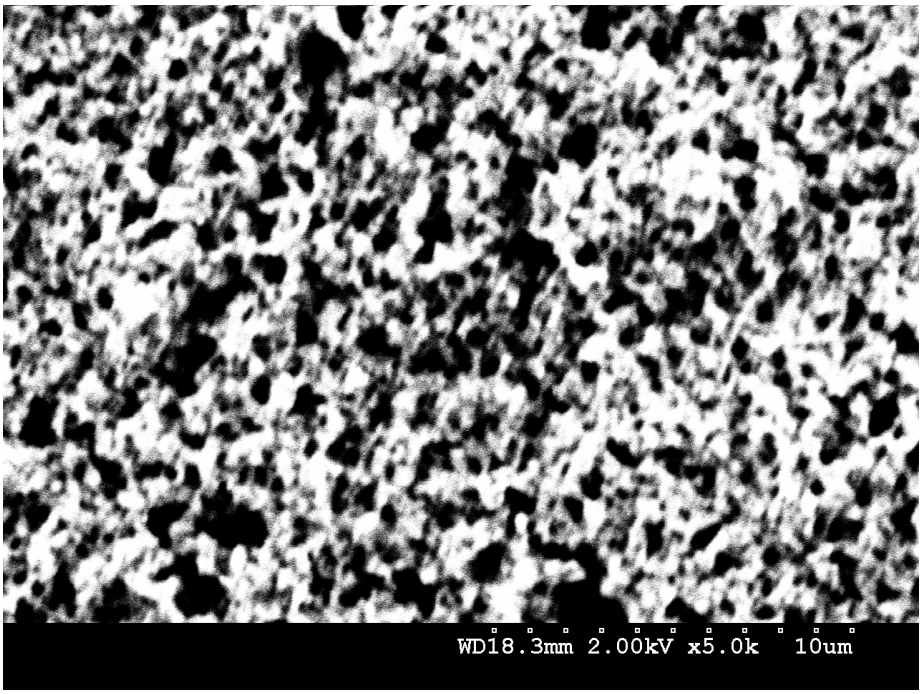

Figure 3.8: SEM image of GDL MPL 5000x magnification

3.1.4 End Plates

The fuel cell end plates were custom manufactured from an Aluminium alloy, 6061. This material satisfied the functional requirements of the end plate, high strength (125 MPa tensile strength) and high thermal conductivity (180 W/m-K) [68]. High strength was required so as to ensure that the end plate would not deflect under the fuel cell sealing force, therefore the compression force would be distributed evenly over the entire cell surface. While high thermal conductivity was required in order to facilitate heat transfer from external heating pads that were required to heat the cell to its operational temperature. Aluminium 6061 is easily machined and is used in a number of practical applications, including automotive parts, and was therefore readily available. Also it was relatively cheap compared to other aluminium alloys. The aluminium end plate used for the PEM fuel cell assembly is shown in Figure 3.9.

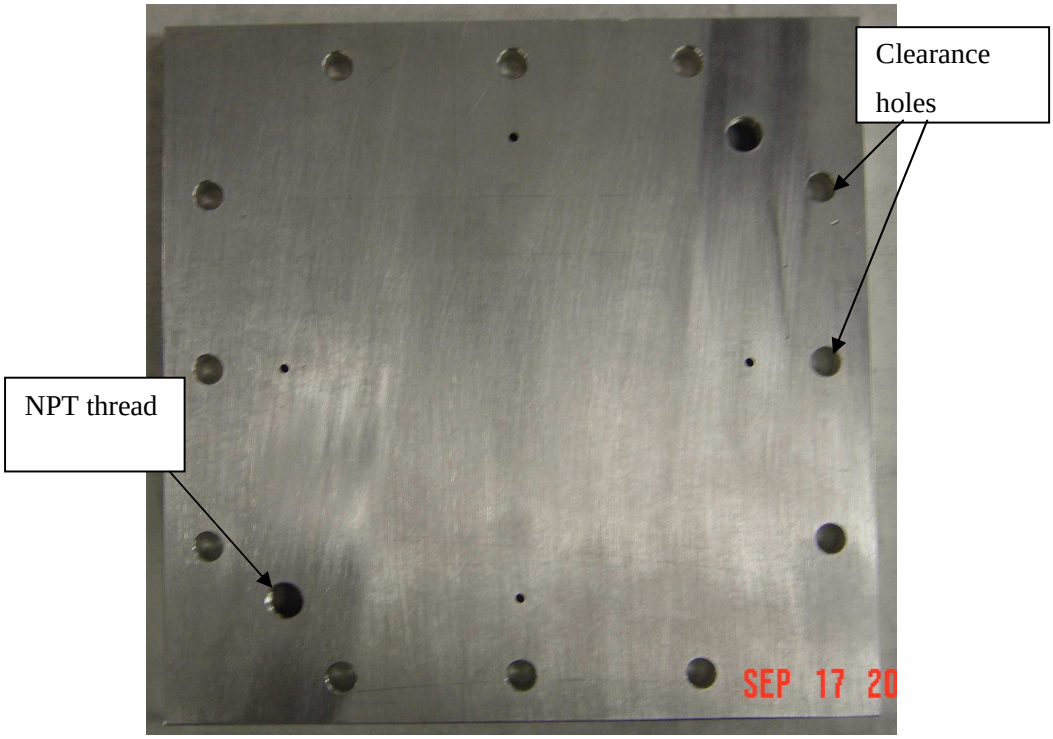

Figure 3.9: PEM fuel cell aluminium end plate

End plates for both the cathode and anode side were manufactured identical to one another. Twelve clearance holes were machined along the perimeter of the plate, three to a side, as illustrated in Figure 3.9. These holes were sized for a free fit to accommodate ¼" SAE 8 bolts. Two ¼" NPT threads were tapped in opposite corners of the plate, designed to accommodate flow connectors for the reactant inlet and outlet flows. Two male ⅜" to ¼" NPT fittings were attached to both the inlet and outlet ports. The copper current collector, outlined in the following section, was fastened directly to the end plate interior surface. To isolate the current collector electrically from the end plate an EPMD rubber gasket was placed between the plates. Though electrically isolated, the rubber allowed for a thermal connection between the surfaces which facilitated in the heating of the fuel cell assembly to operational temperature, via the external heat pads.

3.1.5 Current Collector

The current collectors used for the PEM fuel cell experimental assembly were designed in house and were machined in the Engineering Machine Shop, one such collector is displayed in Figure 3.10. The collectors were manufactured from C15720 copper, which contains 99.6 wt% copper. The copper provided both excellent electrical and thermal conductivity with 89 S/m and 353 W/m-K respectively, measured at 20 ˚C [68]. Through holes were drilled at opposite corners of the collector to allow for reactant gas flow, with spacing identical to that of the aluminium end plate, as illustrated in Figure 3.10. A terminal was machined at the top of the plate to accommodate an external load connection. The load terminal was fastened with a ¼" bolt and clearance hole for this connection was required at the top of the collector terminal. Also an additional clearance hole was machined for the compression bolt that passed through the connection plate terminal. These clearance holes are also identified in Figure 3.10. As was previously mentioned, the current collector was fastened to the aluminium end plate. A rubber gasket was employed between these surfaces to isolate the plates electrically while also ensuring proper sealing for the inlet and outlet reactant flows. Silicone gaskets were employed to seal the reactant flow between the current

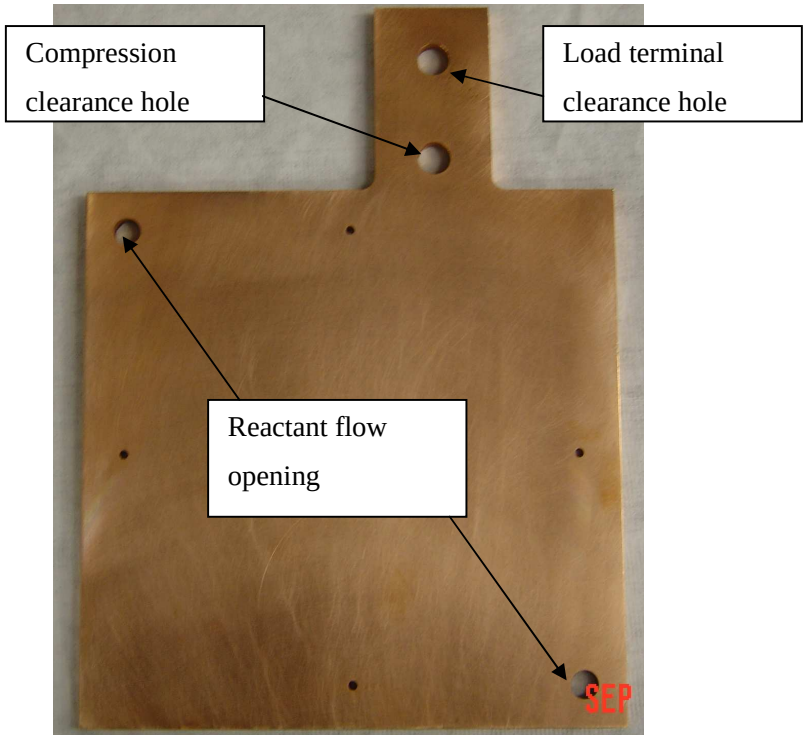

Figure 3.10: PEM fuel cell copper current collector

collector and the bipolar plate. These gaskets had the undesirable effect of isolating the current collector electrically from the bipolar plate and effectively cut the current collection pathway. The gaskets prevented the current collector from making contact with the bipolar plate surface. In order to remedy this, GDLs were placed in the centre of the current collector plate and would allow for contact with the bipolar plate when the assembly was compressed. As previously mentioned, the GDL was constructed from carbon fibre and is electrically conductive, thus completing the load circuit.

3.1.6 Bolts and Sealing Hardware

The fuel cell assembly was sealed using twelve ¼" SAE 8 bolts. To allow for even distribution of the bolt compression force and to ensure locking of the nuts, Belleville and flat washers were incorporated on both the nut and bolt head sides of the cell.

Reactant gas flow between the solid layer interfaces of the PEM fuel cell was sealed by the application of silicone gaskets. These interfaces included the reactant flow ports between the current collector and the bipolar plate and around the perimeter of both GDLs, sealing the membrane layer and the bipolar plate. Additional gaskets were positioned around the perimeter of the current collector in order to maintain a uniform seal between the collector and the bipolar plate. Also a GDL was placed to fit in the centre of these gaskets, fixed to the bipolar plate, so as to ensure electrical contact between these two surfaces, as illustrated in Figure 3.11. The gasket material was a thin gauge silicone, with a thickness of 250 μm. The silicone was available in sheets of dimensions 25 x 25 cm, and individual gaskets were cut from this larger stock. The GDL gasket was cut to fit snugly around the GDL perimeter and was designed with interior dimensions of 106 x 106 mm, allowing for 0.5 mm spacing, and exterior dimensions of 122 x 122 mm, as illustrated in Figure 3.12. To maintain consistent gasket dimensions templates were designed using AutoCAD and were employed in the fabrication process.

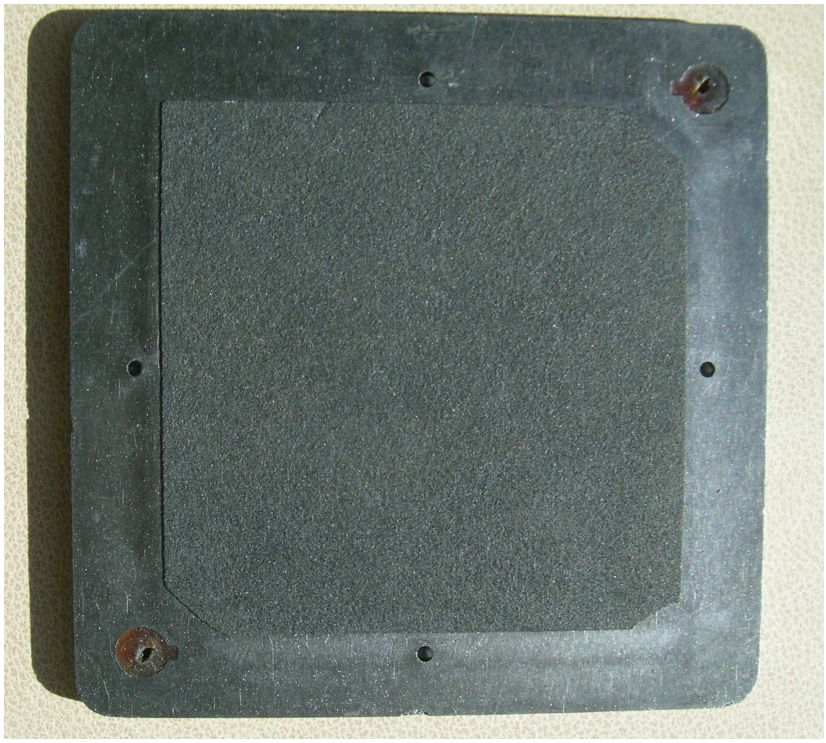

Figure 3.11: Bipolar plate with GDL current collector fastened on back face

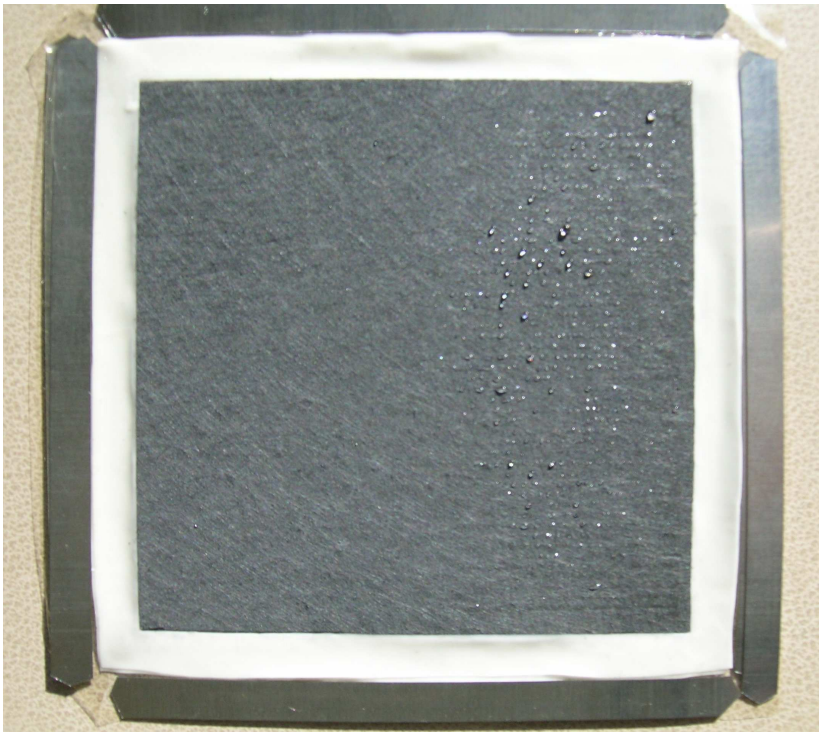

Figure 3.12: GDL gasket configuration

3.1.7 Shims

During the precision compression control portion of the experimental study, shims were incorporated in the fuel cell assembly to limit GDL thickness and control the degree of compression. The shims were positioned in the same plane as the GDL around the perimeter of the GDL, between the membrane layer and the bipolar plate, as illustrated in Figure 3.13. The shims, constructed from high strength rigid material, would stop bipolar plate compression of the GDL at the shim surface, thus maintaining GDL thickness equal to the shim thickness regardless of the compressive force applied. By changing the thickness of the shim used in the assembly, the thickness, and therefore degree of compression, of the GDL could be manipulated in a precisely controlled fashion. Shim stock was available in brass and stainless steel. The brass stock was not selected due to its high ductility. The brass shim was prone to deformation under the compressive stress of the fuel cell and

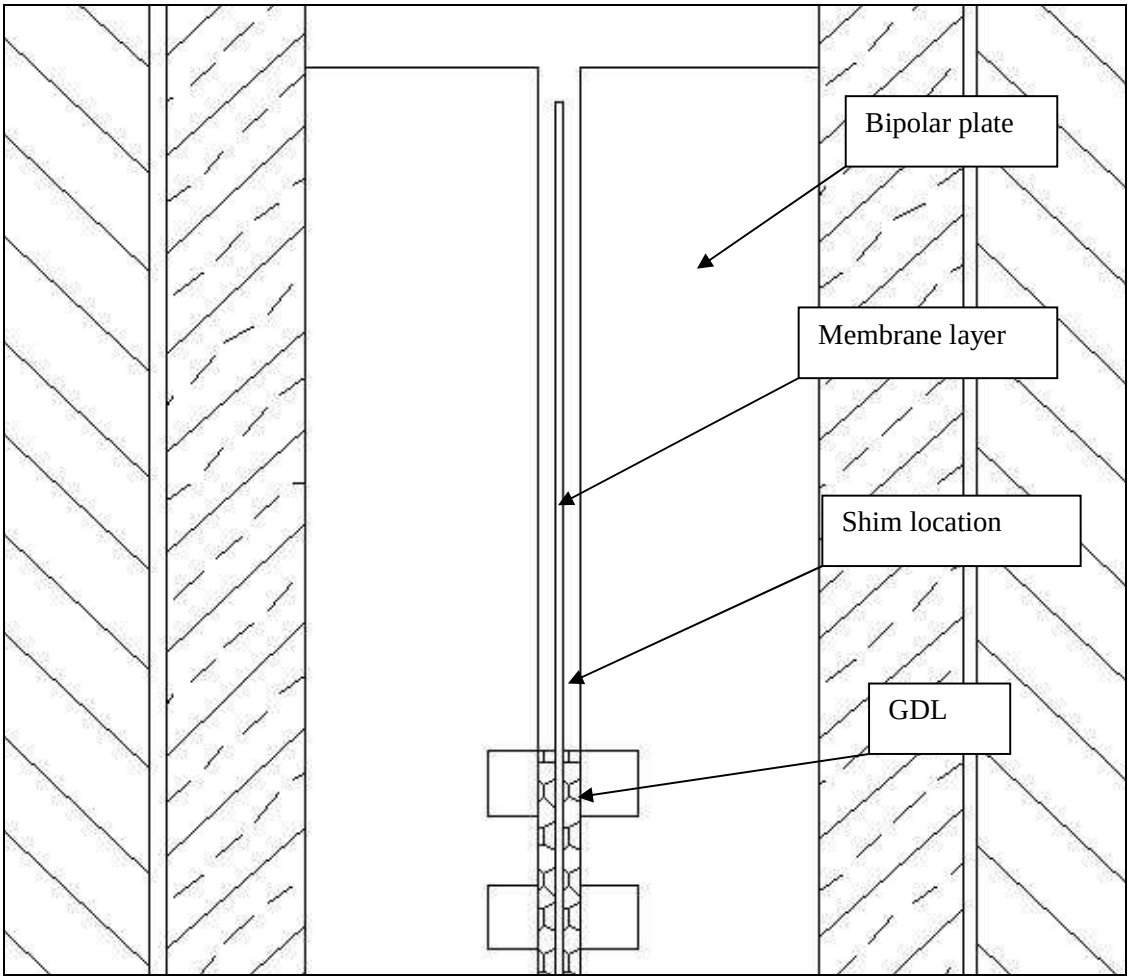

Figure 3.13: PEM fuel cell cross section identifying shim location

was therefore not be a reliable method of GDL thickness control. The stainless steel stock had the advantage of high strength and high corrosion resistance. Resistance to corrosion is especially important due to the hostile environment present in the fuel cell. The high moisture content and high fuel cell operating temperature are conditions that can accelerate the corrosive process. The high strength of the steel ensured minimal shim deformation under the compressive force and therefore guaranteed precise and repeatable control of the degree of compression. Since the gas diffusion layer is designed for slight compression, to ensure complete surface contact, shim thickness that were all less than the thickness of the

GDL, 240 μm, were selected. Stainless steel shim stock was available in thickness of 8, 6 and 4 thousandths of an inch, 200, 150, and 100 μm respectively. When fabricated, the individual shims, as designed for insertion into the cell, were cut at 10 cm lengths with a width of 8 mm, so as not to extend beyond the membrane surface. Also the sharp edges of the shims had to be filed down, as these edges could potentially damage the fragile membrane layer.

3.2 Fuel Cell Assembly Procedure

In order to minimize the presence of unwanted performance variables and ensure repeatable experimental results, a consistent and deliberate cell assembly methodology was applied. This assembly methodology is presented in this section. To arrive at such a methodology was an experimental process in itself. Numerous attempts were made before a final precise procedure was developed. The greatest difficulty was ensuring proper alignment of the cell components without contaminating the reaction or diffusion surfaces. The key to overcoming these obstacles was found to be proper cell component design and preparation along with a great deal of patience.

The cell assembly procedure is as follows

1. The first step was to prepare all single use cell components. This included the GDLs, the GDL gaskets, and the MEA. The diffusion layer and the gaskets were cut to their specified dimensions with the aid of templates, created using AutoCAD. An extremely sharp utility knife was used to cut the components which allowed for precision along with the exertion of little physical effort, as extensive force would damage the diffusion layer. The MEA packaging was cut open, but the MEA was not yet removed so as not to contaminate its surface.
2. Using the assembly jig, the twelve compression bolts were aligned upright, with the bolt head side down. The jig kept the bolts aligned in the desired pattern as the components were stacked on top. The cathode side end plate was the first layer to

be placed on the jig, with care taken to align the bolts through the proper clearance holes.

3. The bipolar plate was then placed on the current collector plate. The plate was aligned such that the inlet and outlet flow paths in the bipolar plate were in line with their respective current collector flow paths. The bipolar plate and current collector had identical dimensions so proper alignment was guaranteed by ensuring that that two plate perimeters were flush and square with one another.

4. The following layer included the GDL and the GDL gasket. The GDL was placed directly on the bipolar plate flow channel, oriented such that the microporous layer was exposed. Care was taken to ensure complete coverage of the flow channel, including the inlet and outlet ports on the plate. The gasket was then set on the bipolar plate surrounding the GDL. Tweezers were used to finely tune the alignment of these components. The gasket's tacky surface made it easy to work with as it would stick to the bipolar plate surface when a slight compressive force was applied.

5. The MEA was then layered on top of the GDL and gasket. The MEA was removed from its protective casing and was centred directly over the GDL. Again, the tacky membrane and gasket surfaces worked as an adhesive when compressed to one another, securing the MEA in position.

6. The following layer was the anode GDL and gasket. This layer was the most difficult to assemble as the gaskets had to be aligned directly on top of one another while also aligning with the GDL and the bipolar plate. For the anode side of the cell the gasket was inserted first. Since the perimeter of the membrane layer was transparent, the cathode gasket was visible and was used as a reference to align the anode GDL gasket. To avoid contamination, tweezers were again used to adjust the alignment precisely. Once the gasket had adhered to the membrane layer, the GDL was placed in the void in the centre of the gasket, microporous side down. If

the gasket had been positioned correctly, the GDL would fit snugly into the opening, with 0.5 mm of clearance on all sides.

7. To align the bipolar plate on the GDL layer stainless steel guide bars were employed. The guide bars allowed for the bipolar plates to be aligned flush and square with one another. Due to the symmetric design of the cell, alignment of these components guaranteed proper alignment with the flow channel surface and the porous layer. The anode bipolar plate was identical to the cathode plate, such that when the two were assembled in the cell, with flow channel side in, the inlet ports were both at the top of the electrode assembly, but on opposite sides of the x axis, established in Figure 1.1.

8. The final layer was the anode end plate and current collector. First the clearance holes in the end plate had to be aligned with the compression bolts. The plate was lowered to a point such that the clearance holes had just engaged the bolts but the current collector had not yet contacted the bipolar plate. At this point the end plate would be carefully lowered so that the current collector edge was flush with the anode bipolar plate.

9. The washers were placed over the compression bolts and the nuts were threaded on and tightened by hand, so as not to fully compress the cell.

10. The next step was to insert the stainless steel shims. This was not done for every cell assembly, only those that required the precise compression control. Shims, all of equal thickness were inserted on either side of the membrane, inside the bipolar plates. The shims had to align directly on top of one another on either side of the membrane, with care taken to ensure that none of the shims extended beyond the membrane perimeter. Such a scenario could have resulted in a short circuit of the current collection pathway, or critical damage to the membrane layer, both of which would have significantly compromised the experimental results. Tweezers facilitated this shim alignment process a great deal.

11. Once the shims were in place, should they be required, the nuts were tightened using a torque wrench. Tightening was done in stages so as to evenly distribute the compressive force over the cell, without overloading one of the edges. Bolts were tightened to a minimum value of 50 in-lbs (5.65 N-m). The centre bolts on each edge were tightened first, alternating sides after each bolt. The same was done for the other two bolts on each edge. Once the initial compression was complete the cell was fully compressed. For assemblies with no shims, the cell was compressed by applying the desired torque value, again alternating sides for each bolt position. For shimmed assemblies, torque was applied at increasing increments of 5 in-lbs until the bipolar plates engaged the shims. Once the shims were fully engaged, the cell was fully compressed. Though in theory the introduction of the shims into the cell assembly meant that precise torque control was not required, so long as a minimum value to engage the shims was applied, the assembly could not be compressed passed the shim thickness. However extreme over compression was not desired as it could potentially result in the damage of the fragile MEA and the introduction of unwanted variables. For this reason the incremental torque application was instituted.
12. The final step was a visual inspection of the cell. The current collectors and bipolar plates were inspected to ensure they were flush and square. The membrane perimeter was checked for tears or other forms of damage. The shims were inspected to check that they had not shifted during the assembly process and were still in their desired positions. Following the visual inspection, the cell was ready for the test procedures.

3.3 Hydrogenics Fuel Cell Automated Test Station (FCATS)

The FCATS is a fully integrated fuel cell test station designed and manufactured by Hydrogenics Corporation. The basic system components include a gas supply system, an electronic load box, and a personal computer which runs the control and data logging

program, HyWare ®. Using a LabVIEW ™ interface, the station allows for the control of important cell parameters to more than acceptable tolerances. These parameters include the reactant flow conditions such as inlet pressure, inlet temperature, relative humidity, and flow rate, as well as overall cell temperature and the electrical load conditions, current and voltage. The system also monitors the stability of the cell and maintains safe operating conditions. Safety controls are an extremely important feature as the test rig can present a potentially explosive environment as it requires Hydrogen gas supply. The FCATS is displayed in Figure 3.14.

Figure 3.14: Hydrogenics' Fuel Cell Automated Test Station (FCATS)

The gas supply system consists of two separate inlet conditioning lines. The reactant gas is supplied by interchangeable external pressurized cylinders. For the study in question the cathode side was supplied with high purity hydrogen, while the anode was supplied with air, both with a zero moisture content. Other compositions including pure oxygen, or low purity hydrogen with either carbon dioxide or carbon monoxide can also be used. Figure 3.15 illustrates a schematic of the gas supply system. The nitrogen supply line is connected directly to both reactant streams and is used to purge the system when it is required, typically before and after performance testing. Steam generators are used to humidify the reactant streams, as the moisture content is essential to ensuring proper membrane function. Dry reactant gas is supplied so that this moisture content can be precisely controlled. The steam is supplied using a deionised water supply and a 1.5 kW bubbler steam generator. The

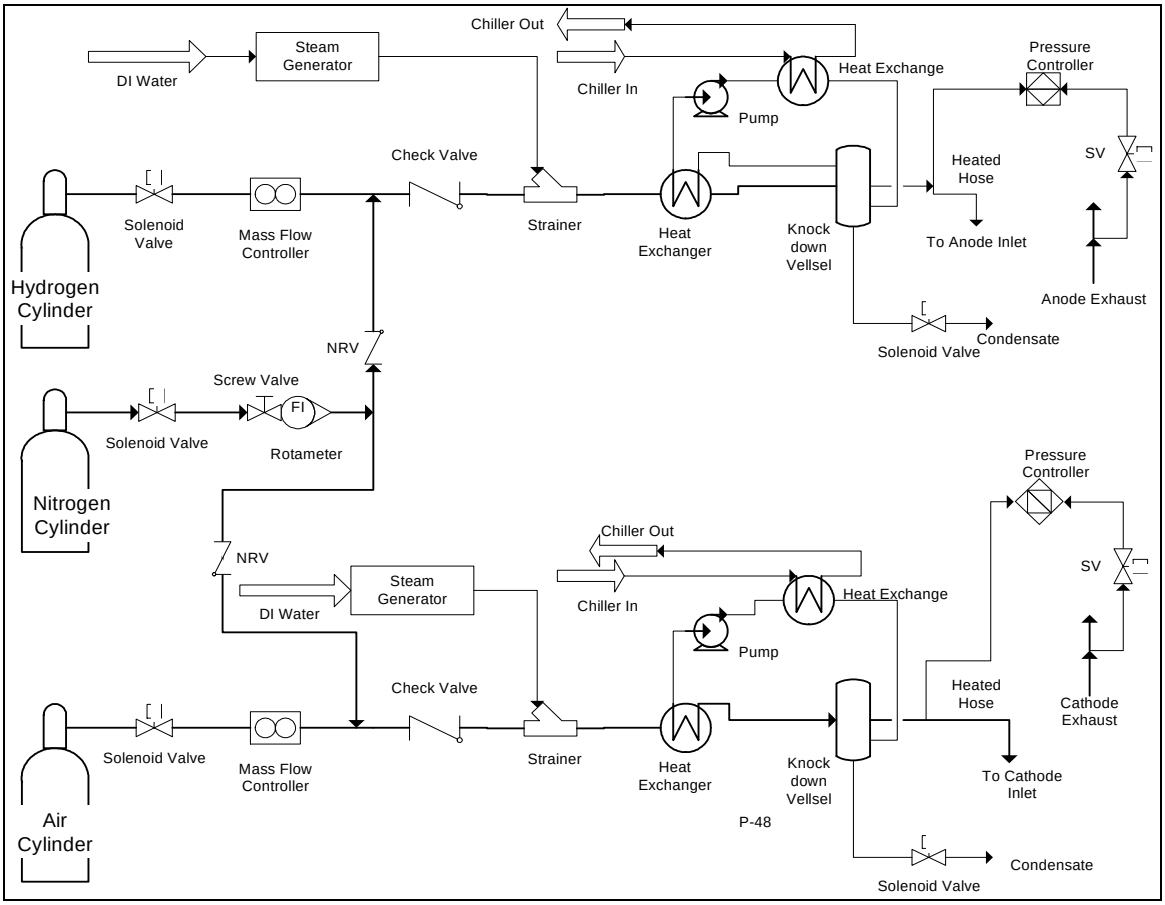

Figure 3.15: FCATS gas supply system schematic

precise moisture content is attained by condensing any excess vapour. This is accomplished by passing the reactant flow through a heat exchanger, which also contains a chilled water circulation. The heat exchange process creates a two phase flow, and the condensate can then be extracted. The supply is heated to its desired temperature, ideally the cell operating temperature, using the heated reactant supply hose.

To maintain overall cell operating temperature a simple temperature control system was implemented. Although the heated reactant gas supply and the current flow generated during cell operation would supply heat to the cell, these sources were insufficient as they could not rapidly achieve operating temperature and maintain it at a controlled level. The control system consisted of two flexible electric heat pads, fixed with a clamp to the cell end plate, a thermocouple, located in the cathode bipolar plate, and a fan placed in close proximity to the cell. The heat pads would rapidly raise the overall cell temperature, which would be monitored by the bipolar plate thermocouple. The bipolar plate location was selected, due to the fact that this was the closest site to the reaction surface that could accommodate a thermocouple. When the operating temperature was achieved, 80 ˚C for this study, the heat pads would shut off. Should the temperature reach an excessive level, over 81 ˚C, the fan would be engaged, rapidly increasing heat transfer to the surrounding environment.

The load controller was the SDI 1043 model, designed and manufactured by TDI Transistor Devices, USA. The load box specifications were for 50 V and 400 A, combining for 2000 W of power. The box is fully integrated with the HyWare control system, and can be controlled in both galvanostatic and potentiostatic modes. The most valuable function of the integrated system is the load follow mode for cell test operation. This mode allows for the inlet flows to be controlled through the desired load setting, according to the specified stoichiometry. This is the ideal method for generating consistent cell potential curves, as a function of current load, while maintaining consistent reactant flow rates.

3.3.1 Uncertainty Analysis

With any experimental procedure there will exist a certain level of uncertainty within the results. The uncertainty for the FCATS, as provided by the manufacturer [69], is summarized in Table 3.2. The uncertainty of the flow parameters is with reference to full scale (FS), or the maximum flow value. The test station is capable of measuring up to 350 kPa, however, the manufacturer recommends a maximum pressure of 250 kPa, and does not guarantee the accuracy of any results beyond this point. A similar condition existed for the fuel cell voltage parameter. While the station was capable of providing readings to 0 V, the manufacturer recommended that no readings below 0.35 V be taken, as accuracy could not be guaranteed below this point. There exist a number of sources of unquantifiable uncertainty, making it difficult to determine the true accuracy of results collected. However, consistent results were obtained. The procedures for each performance test configuration were repeated several times, with standard deviations in the range of 0.0008 – 0.004 V.

Table 3.2: Summary of parameter uncertainty for FCATS

Parameter		Units	Range	Uncertainty
Flow	Anode	sccpm	0 - 4000	± 1% FS
	Cathode	sccpm	0 - 16000	± 1% FS
Temperature		˚C	-20 - 100	± 2 ˚C
Pressure		kPa	0 - 350	± 3 kPa
Load	Voltage (high range)	V	10 - 50	± 0.25%
	Voltage (low range)		0 - 10	± 0.5%
	Current (high range)	A	5 - 400	± 0.25%
	Current (low range)		0 - 5	± 0.5%

3.4 Test Procedures

In order to ensure accurate and consistent experimental results, a precise and systematic test procedure was developed. This procedure involved three distinct test phases. First, the

integrity of the cell had to be ensured by testing for the presence of leakages. Once proper sealing had been established the flow field of the cell was analyzed by the investigation of flow channel pressure drop data. The final phase was the performance test, where cell potential data was collected for a consistent current density domain. The detailed methodology of the three test phases will be presented in this section.

3.4.1 Leakage Test

In order to ensure the integrity of the test assembly prior to the flow and performance tests a leakage test was implemented. This test identified leakages attributed to improperly sealed interfaces as well as reactant cross over. Improper sealing would have resulted in the leakage of reactant flow into the surrounding environment, thus reducing the capacity of the cell to properly deliver these reactants to the reaction surface and compromising cell performance. Reactant flow crossover is the phenomenon where reactant flow passes directly through the membrane layer, bypassing the reaction surface altogether, and is attributed directly to membrane integrity. The presence of this phenomenon would also compromise cell performance. The test process was a short but effective procedure. A pressure gauge, equipped with a flow valve, was inserted in the cathode inlet, while the cathode outlet was blocked. The cathode supply flow tube was then fastened to the pressure gauge on the cathode inlet. A small cathode reactant flow was initiated, 200 sccpm, after checking to ensure that the pressure gauge valve had been switched open. After approximately 100 kPa of pressure had accumulated the flow was terminated and the pressure gauge valve was closed. At this point the reading on the pressure gauge was monitored. Should a leakage or flow cross over occur the pressure reading on the gauge would drop. This process would be repeated for the anode side, should the cell pass the cathode side leakage test. If the cell should fail either of these tests then it would have to be adjusted. The more likely source of this pressure drop would be due to gasket leakage. Therefore the most appropriate immediate plan of action would be to disassemble the cell and replace the silicone gaskets. Should the cell fail a second leak test, then reactant

crossover would have to be investigated further. Since the membranes are significantly more expensive than the silicone gaskets discarding an MEA would have to be sufficiently justified. To specifically test for reactant cross over the same leak test procedure would be followed, however, with the addition of an anode outlet tube that would be placed with the exhaust end in a small container of water. During the test, should this glass bubble, then reactant cross over would be confirmed and the MEA should be discarded. It should be noted that no cell assembly failed consecutive leak tests and no reactant cross over was found to be present. In fact, once the assembly procedure had been finalized, no cell failed a single leak test.

3.4.2 Flow Test

The flow test was designed to identify changes in pressure response to flow rate as compression was manipulated. Also, flow test data was valuable in identifying other flow phenomenon, such as internal leakage resulting from insufficient surface contact. The procedure involved running the cell at gradually increasing reactant flow rates and collecting the corresponding flow channel pressure drop data. In order to isolate for the effects of changing flow field geometry the flow was provided with no humidification and each reactant flow, both anode and cathode, were run individually. This would effectively eliminate any liquid water build-up which could significantly affect the cells pressure response. Flow testing both the anode and cathode flow channels was found to be redundant. Due to cell symmetry, they both exhibit almost identical pressure drop response as a function of flow rate. Since the flow domain for the cathode side is more expansive during performance testing, it was selected to represent the overall cell flow channel pressure drop.

The steps of the procedure were as follows. The first step is to activate the entire test station, which includes activating power supplies and opening all flow valves. Then the cathode inlet and outlet tubes are attached to their respective fuel cell ports. The cathode reactant flow was initiated, starting at the value of 200 sccpm. Since the operational flow

domain occupies mostly the lower flow rate region, the incremental increase of flow rate for the flow test was smaller. As the flow rate increased past 1000 sccpm, the increment was increased, as flow data in this region was not as significant. For the range of 200 – 1000 sccpm the flow rate was increased at increments of 100 sccpm, for the range of 1000-3000 sccpm the flow rate was increased at increments of 500 sccpm. This generated a broad spectrum of pressure data, with finer detail in the region of greater interest. For each data point the cell was given sufficient time to reach steady state, 90 s. The maximum flow rate tested was 3000 sccpm, at which point the flow test was terminated.

3.4.3 Performance Test

The performance test was designed to allow for the inspection of cell potential and power density response, as a function of current density, to changes in cell compression. In addition the procedure was used to investigate the sensitivity of this performance response to changes in catalyst platinum loading. Each test cell was run at varying current load settings, increased incrementally, while cell potential was monitored, along with several other controlled parameters. The load follow control was used to manipulate flow rate and control the current domain, this was applied by changing the load setting and setting the appropriate flow stoichiometry. For a given load and stoichiometry value the test station would set the appropriate flow rate that satisfied these conditions. Stoichiometry in this case refers to the ratio of the molar flow rate of reactants supplied to the cell versus the molar flow rate of reactants consumed by the cell, as determined by the balanced chemical reaction equation. Simply put, stoichiometry provides a factor of how much excessive reactant is provided, for example, a stoichiometry of 2 means that twice the required amount of reactant is supplied. The initial current value was 5 A, which, for the given experimental cell, resulted in a current density of 0.05 A/cm^2. No consistent maximum current density was established as there were factors that effectively limited the domain depending on the cell construction and test conditions. These factors were flow channel inlet pressure and cell potential. As was mentioned in section 3.3.1, the test station was not stable at pressure values exceeding 250

kPa and cell potential values below 0.35 V. In each test case one or both of these factors limited the maximum current density set point. At higher flow rates, in the high current density region of the domain, pressure would clime to exceed 250 kPa or cell potential would drop below 0.35 V. When either of these points was reached the performance test would be terminated. In order to neutralize the effects of liquid water build-up and MEA degradation on the performance of the cell, each test assembly was run for only two consecutive performance tests. This would ensure that any changes in performance were not attributed to cell flooding or catalyst erosion or poisoning, and that every compression configuration would have a level playing field. Between consecutive test runs, the cell was cooled to ambient temperature, and purged, clearing any liquid water or reactant remnants from the cell. Following these two consecutive tests the cell was disassembled and single use components, such as the GDL, the GDL gasket, and the MEA were removed from the cell. No cell was disassembled immediately following a test as residual thermal stress from the layered cell construction posed a risk of damaging both disposal and permanent cell components. For this reason the cell was allowed to cool to ambient conditions and was fully purged prior to disassembly.

The performance test procedure was as follows;

1. The first step was to fully activate the test station. This included opening all water and gas supply lines and connecting all power supplies. Once the station had fully booted, the HyWare program was initialized and the LabVIEW interface was opened.

2. The fuel cell was then connected to the test station. This included inserting both inlet and outlet tubes for the anode and cathode flow channels, connecting the load terminals to the current collector plates, clamping the heat pads to either side of the cell on the end plate surface, and inserting the cell temperature thermocouple in the cathode bipolar plate. The cell was also wrapped with fibreglass insulation as this aided with heat retention and accelerated the cell warm-up process.

3. After cell hook-up was complete the appropriate operating parameters were set. The overall cell temperature was set to 80 ˚C, which initiated the electric heating pads. The steam generator was activated for both the anode and cathode flows and the appropriate flow parameters were set, outlined in Table 3.3, where relative humidity is represented by RH. Since the flow was controlled using the load follow setting, a minimum current density was used as the minimum flow rate parameter. The corresponding stoichiometry then established the associated flow rate that satisfied the current density setting. The minimum flow rate was established to ensure proper flow control, as the test station would not initiate a flow rate for current densities below 150 mA/cm^2, which corresponds to 0.15 A/cm^2 and 15 A for the experimental cell in question. This meant that lower current density domain values, 0.05 and 0.1 A/cm^2, would operate at slightly elevated stoichiometry, however at these low current density values, the increased stoichiometry had a negligible effect.

4. The cell would have to reach its operational temperature, 80 ˚C, before data collection could begin. To facilitate this process a small load was applied to the cell, 0.25 A/cm^2. Operating the cell would generate heat and allow the cell to reach operational temperature sooner. The warm-up process typically took between 60 and 90 minutes.

5. Once operational conditions had been achieved the performance data was collected. Just prior to data collection, the cell was fully purged as a precautionary step. This would ensure that all other factors, such as flooding would not compromise the data collected. The cell was run over a current density domain beginning at 0.05 A/cm^2 and increased at incrementally until it reached an operational limitation, outlined earlier in this section. During data collection cell temperature was monitored carefully and was maintained within the bounds of 80-81 ˚C. At each value in the current domain the cell was provided sufficient time to reach equilibrium, which was a minimum of 3 minutes. A datum point was collected for all relevant parameters at every 20 seconds.

6. When the operational limit had been reached, the data collection was terminated and the current load was removed. The cell was fully purged and left to cool to ambient temperature before a second run was performed or the cell was disassembled.

Table 3.3: Summary of test fuel cell flow parameters

Flow Channel	Min. Flow Rate (mA/cm^2)	Min. Flow Rate (sccpm)	Inlet Temp. (˚C)	RH (%)	Stoichiometry
Anode	150	126	80	100	1.2
Cathode	150	499	80	100	2

Chapter 4
Results and Discussion

The results from the experimental tests of numerous PEM fuel cell assemblies, performed at varying operating conditions, are presented and discussed in this chapter. The experiments place emphasis on the effects of compression on the performance of a PEM fuel cell. Following difficulties with the performance of the original fuel cell configuration, a preliminary design analysis was performed in order refine the experimental setup and procedure. This investigation compared two MEA configurations for the experimental assembly, a five and a three layer electrolyte assembly. The five layer MEA was the assembly used in the original fuel cell configuration, a more recent MEA design, while the three layer assembly was a design that had been used in previous fuel cell experiments. The cell was assembled with either MEA and the associated variations in performance were quantified.

Once the design had been finalized, the fuel cell test assembly was validated through a comparison with pre-existing fuel cell performance curves. The goal of this analysis was to establish the quality of the fuel cell assembly relative to peer tested and commercial PEM fuel cells. This was done in order to confirm the integrity of the experimental assembly in question and ensure results generated from this assembly were relevant to the advancement of fuel cell technology.

Following the validation of the cell design a preliminary compression analysis was performed. This compression study aimed to investigate changes in flow and performance behaviour as a result of increasing cell compression, varied through applied torque. A general performance and flow trends as a function of compression were identified. The factors potentially affecting cell performance, which were manipulated by cell compression, were identified as:

- Sealing and surface contact
- Pressure drop across the flow channel

- Porosity of the GDL

Each factor was analysed independently in order to determine the individual contribution to changes in performance. Poor sealing and surface contact are undesirable in any fuel cell operation and were therefore isolated and eliminated. Multiple modes of leakage were discussed, including external and internal leakage, and a method of identifying their presence was presented. A consistent symptom of incomplete surface contact was identified, it being a unique pressure response. The presence of this pressure response was then used to quantify the performance gain from proper sealing and surface contact.

In order to consistently ensure proper sealing and surface contact as well as precisely control the degree of compression, a revised compression technique was required. Varying the applied torque was not a reliable method as it was difficult to apply subtle changes in compression. Once surface contact was eliminated as a variable, the effects of compression would most significantly affect the flow field and the GDL physical properties, both a function of GDL thickness. A technique to control GDL thickness, as opposed to applied compression force was employed. By introducing stainless steel shims, parallel to the GDL, its thickness would be maintained regardless of applied torque, so long as a minimum value was applied. This would allow for the detailed analysis of compressive affects beyond the sealing and surface contact.

The detailed analysis was then performed using the shim compression control technique. The effect of varying pressure response, as a result of increased compression, was investigated as a performance variable. In order to gain a better understanding of the mode of pressure variation in the flow field, a theoretical model was developed to simulate a known flow scenario. This scenario was then compared to the pressure drop results for the experiment in order to identify a trend in pressure response. Once a trend was identified, increased pressure drop for increasing compression, the pressure could be manipulated via the test station for performance tests of cells with varying compression, on the scale that it changed in the various compression thicknesses, in order to ensure equal pressure. By

comparing the cells operating at equal pressure but varying compression, the performance contribution of pressure could then be quantified.

Following the quantification of the pressure response contribution to performance, the final remaining variable was GDL porosity. Compression of the GDL would decrease the porosity, as a compacted GDL would fold in on itself, filling the void space with its own solid media. The decrease in porosity would result in changes to the physical properties in the porous media. The properties of particular interest were permeability and electrical conductivity, as these have the greatest impact on cell performance. Changes in these properties, with respect to changes in porosity were estimated using correlations from literature. Once a general trend in physical properties was established, the effects of these changes on performance of the fuel cell were analysed. The performance behaviour was presented in terms of cell potential and power density data, collected through controlled compression, experimental testing. The limiting factor of fuel cell performance was identified and the benefits of precision fuel cell compression were quantified.

Finally, the sensitivity of cell compression, and the resultant performance response, to changes in platinum loading was investigated. The effect of reducing platinum loading on cells of varying degrees of compression was presented, with the goal of furthering commercialization through facilitation of cost reduction.

4.1 Membrane Electrode Assembly (MEA) Design Analysis

Originally the PEM fuel cell assembly included a five layer MEA, as this was the most recent version offered by the electrolyte supplier. However, after problems arose during both high and low compression tests, use of the five layer MEA had to be re-evaluated. As the three layer MEA has been used in past studies by the Fuel Cell and Green Energy Group, it was hoped that the three layer assembly would remedy these difficulties. The two assemblies differed in a number of aspects. The five layer MEA possessed two additional layers, GDLs, which were fastened to the assembly adjacent to the catalyst layer. It was this

restrictive design of the five layer MEA, with a fixed GDL, that resulted in poor performance. The three layer MEA possessed no such fastened GDL, and required an external GDL, which would be layered adjacent, but not fastened, to the catalyst layer. The two configurations also had different physical structures, while the five layer GDL possessed a fragile structure, with a porosity of 85%, the GDL supplied by the manufacturer for the three layer assembly was denser and more rigid, with a porosity of 78%. The two electrolyte assemblies were compared at two compression values, a high compression case, where the GDL thickness was controlled at 100 microns, and a low compression case, with a GDL thickness of 200 microns. A comparison of the three and five layer MEA dry flow test results for high compression test revealed no unexpected phenomena, as illustrated in Figure 4.1. Both experienced a close to linear progression of pressure as flow rate was increased. The larger pressure drop seen in the three layer MEA can be attributed to the denser carbon fibre arrangement in that GDL, discussed in more detail in the following sections.

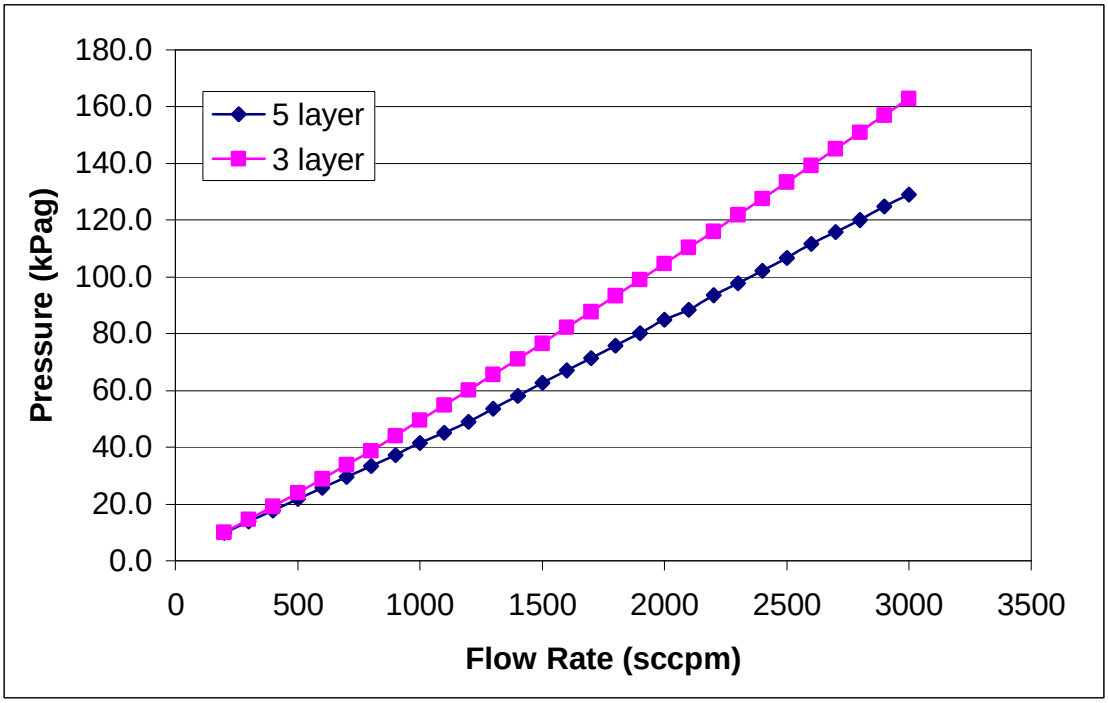

Figure 4.1: MEA design comparison for cathode pressure drop during dry flow test, 5 and 3 layer MEA with 0.4 mg Pt/cm^2

During the warm-up period for the high compression performance test the cell was exposed to constant anode and cathode flow rates, 125.2 and 498.6 sccpm respectively. Ordinarily a flow channel exposed to a constant flow rate and constant operating conditions would experience a constant pressure drop over the channel length. During the warm-up procedure the conditions within the cell were gradually changing, from dehumidified ambient conditions to a steady state temperature of 80 ˚C with a gas flow at 100% relative humidity, operating conditions. As a result the pressure drop across the channel was expected to see a nominal increase from initial conditions to operating conditions. The warm-up cycle for the high compression five layer configuration displayed a significantly larger pressure drop increase than was to be expected. Figure 4.2 displays a comparison of the cathode inlet pressure for a high compression three layer MEA cell assembly and that of the five layer MEA fuel cell. It can be seen that the two cells experienced similar pressure conditions up until ten minutes into the warm-up cycle, at which point the cathode pressure for the five layer MEA cell increased at a significantly greater rate. At the point where the

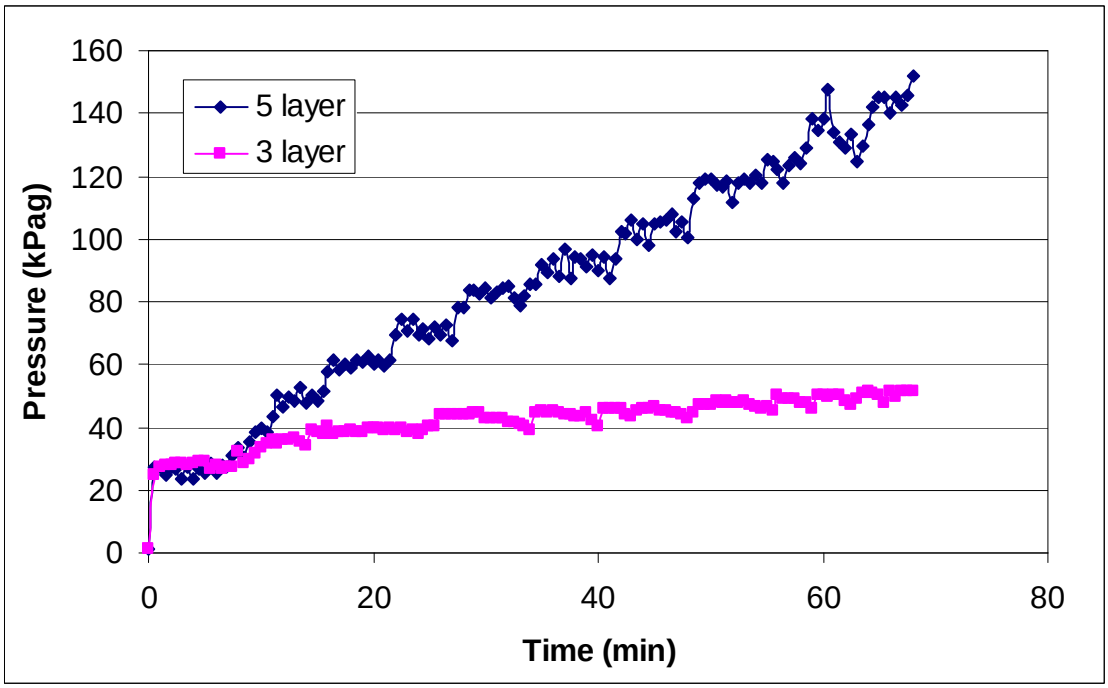

Figure 4.2: MEA design comparison for cathode pressure drop during fuel cell warm-up procedure, 5 layer and 3 layer MEA with 4 mg Pt/cm^2 (high compression)

cells have reached operating temperature, after roughly 70 minutes, the three layer MEA cell had a cathode pressure of 51 kPag, while the five layer assembly reached a cathode pressure drop of 152 kPag, an increase of 151% (101 kPag). This high pressure would have significantly limited one's ability to extract meaningful performance data as the test station would have reached its maximum pressure reading at a relatively low current density. The drastic change in pressure behaviour of the five layer cell from the dry flow test to the warm-up cycle would lead one to believe that the change in thermal conditions of the cell was a causal factor in this shift. This was confirmed upon disassembly, as the five layer MEA was examined and was found to have critical GDL structural damage, displayed in Figure 4.3 and Figure 4.4. The thermal expansion in the cell during the warm-up had distorted the GDL. With the GDL fastened to the membrane layer its ability to expand uniformly was restricted, that combined with the high cell compression, 100 microns, resulted in the distortion. This distortion and compression combined with the GDL's structural fragility resulted in the GDL being crushed and forced into the flow channels along the GDL perimeter thus inhibiting the flow through the channel and significantly increasing the pressure drop.

Figure 4.3: Damaged 5 layer MEA - 1

Figure 4.4: Damaged 5 layer MEA - 2

The low compression, five layer, cell assembly displayed better operational pressure performance. Figure 4.5 displays a comparison of the operational pressure curves for the five and three layer MEA cell assemblies, with 200 micron GDL thickness. The five layer MEA cell operated at only marginally lower pressure than the three layer cell, and there were no pressure spikes, which indicated that the five layer GDL had not incurred any catastrophic damage during the heating of the cell. The lower degree of compression allowed for greater mobility of the GDL within the assembly. However, an analysis of the performance results for the five layer MEA reaffirmed the shortcomings of this configuration, displayed in Figure 4.6 and Figure 4.7. Visual inspection of the graphs revealed that the three layer cell was capable of operating at a significantly larger current density before reaching the limiting cell voltage of 0.35 V and was therefore capable of attaining much greater power density. Direct comparison at a current density of 0.5 A/cm^2 reveals that the three layer cell operated at a 64% greater power density (0.12 W/cm^2). Upon examining the disassembled cell, following the test and a sufficient cool down period, the

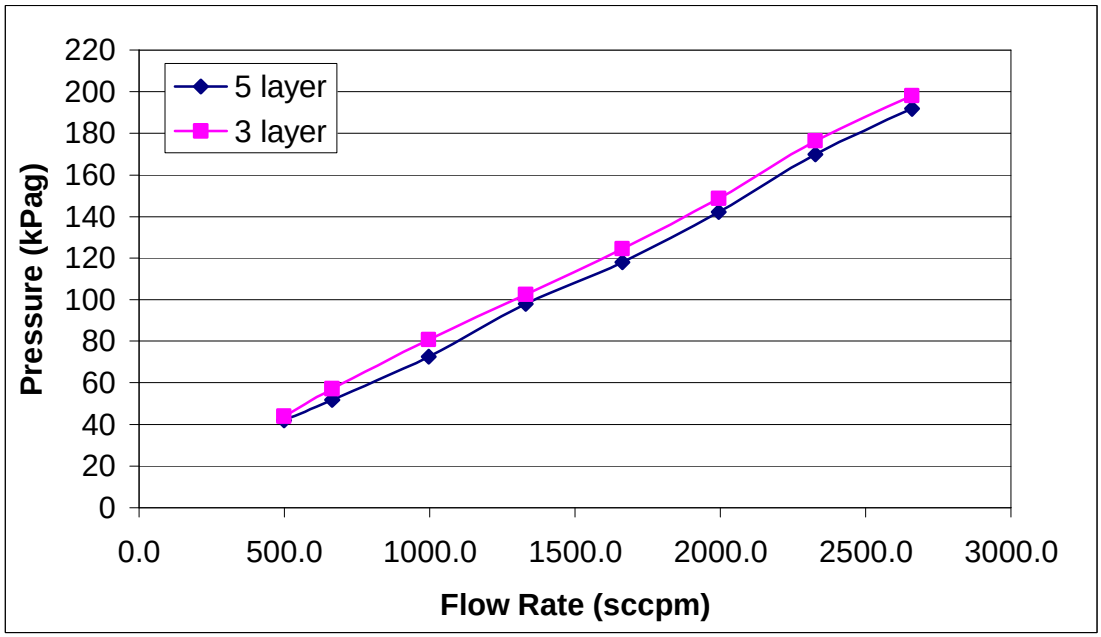

Figure 4.5: Comparison of operational cathode pressure for 5 and 3 layer MEA cell assemblies with 2 mg Pt/cm^2 (low compression)

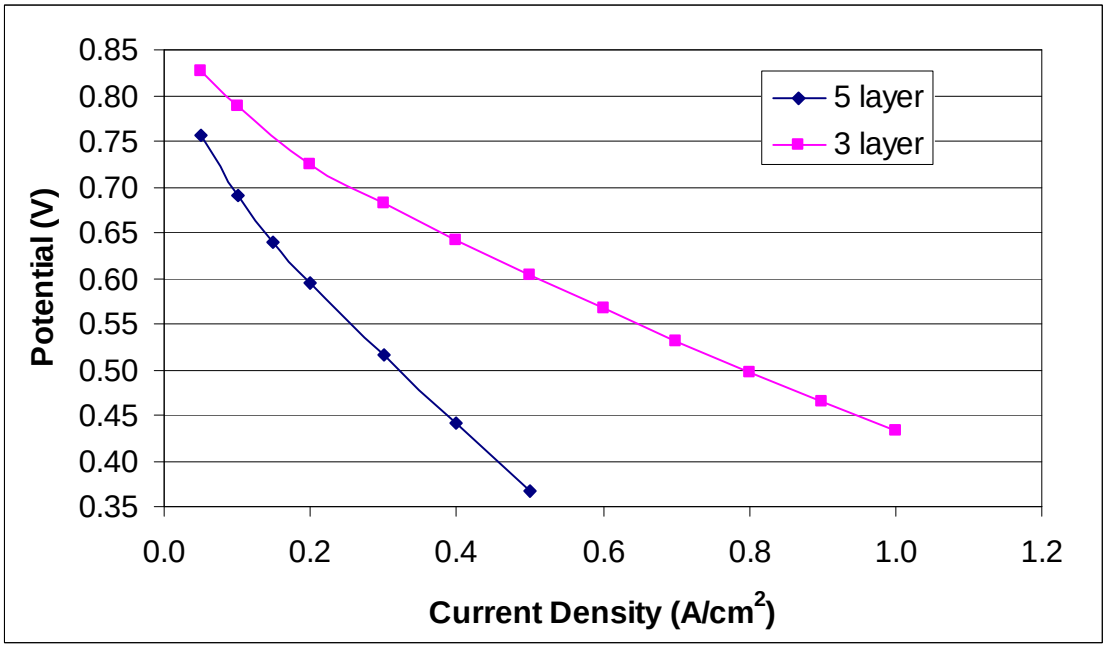

Figure 4.6: Comparison of cell performance for 5 and 3 layer MEA cell assemblies with 2 mg Pt/cm^2

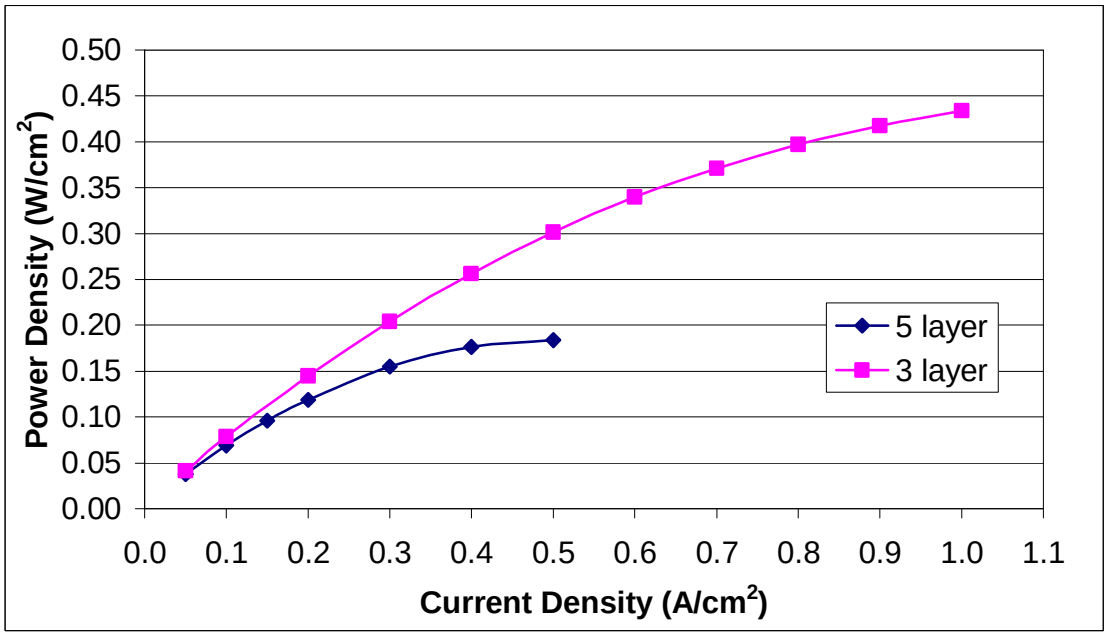

Figure 4.7: Comparison of cell performance for 5 and 3 layer MEA cell assemblies with 2 mg Pt/cm^2

lower compression five layer MEA also appeared to be physically deformed. The damage in this case was not a result of compression but rather membrane distortion. Thermal strain, created by the varying thermal expansion coefficients of cell components, caused the GDL to separate from the membrane layer and protrude out in the centre of the electrolyte assembly. This separation would have resulted in poor reactant delivery and was most likely the cause of the poor performance. In addition to the performance limitations the five layer MEA did not lend itself to the controlled compression procedure outlined later in this chapter. The design did not allow for measurements of the GDL to be made independent of the other membrane assembly components, and the restrictive nature of the assembly made it difficult to contain within the fuel cell. The five layer MEA was eliminated from the fuel cell design, as it was proven to be vastly inferior, and replaced with the three layer MEA with a separate micro porous GDL.

4.2 Fuel Cell Performance Validation

In order to ascertain the quality of the performance results obtained by the fuel cell assembly in question, a comparison of performance data produced by similar cell configurations, tested by peers, was performed. Figure 4.8 and Figure 4.9 display a comparison of the performance results of the current cell assembly, labelled MacDonald (2008) and that of a previous model, labelled Sabir (2004), which was designed and tested at the University of Waterloo. Sabir, a former colleague and member of the Fuel Cells and Green Energy group, built and tested his cell at the University of Waterloo as part of a MASc study [15]. This design was the basis for the current fuel cell design with only minor modifications in the components used and the assembly process. This offers an ideal scenario for comparison as the equipment used for the performance test were identical to that used to test the present fuel cell design, thus minimizing changes in variables affecting performance. As well, since the testing was performed in house, a detailed transcript of the test procedure and assembly variables was available for comparison.

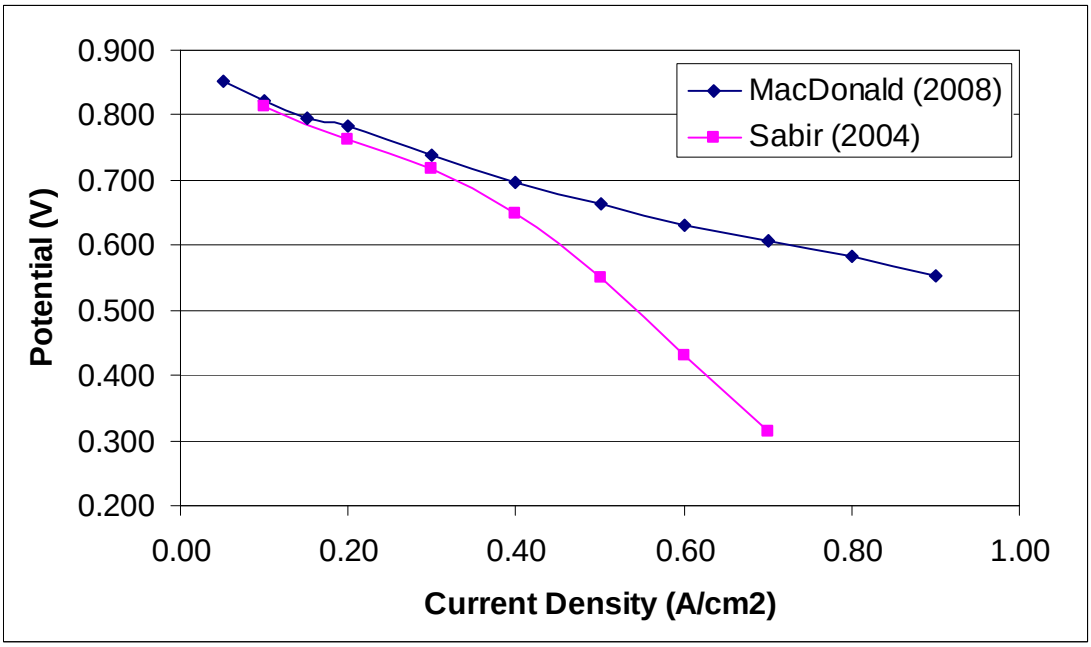

Figure 4.8: Performance comparison of current PEM fuel cell configuration with peer tested configuration

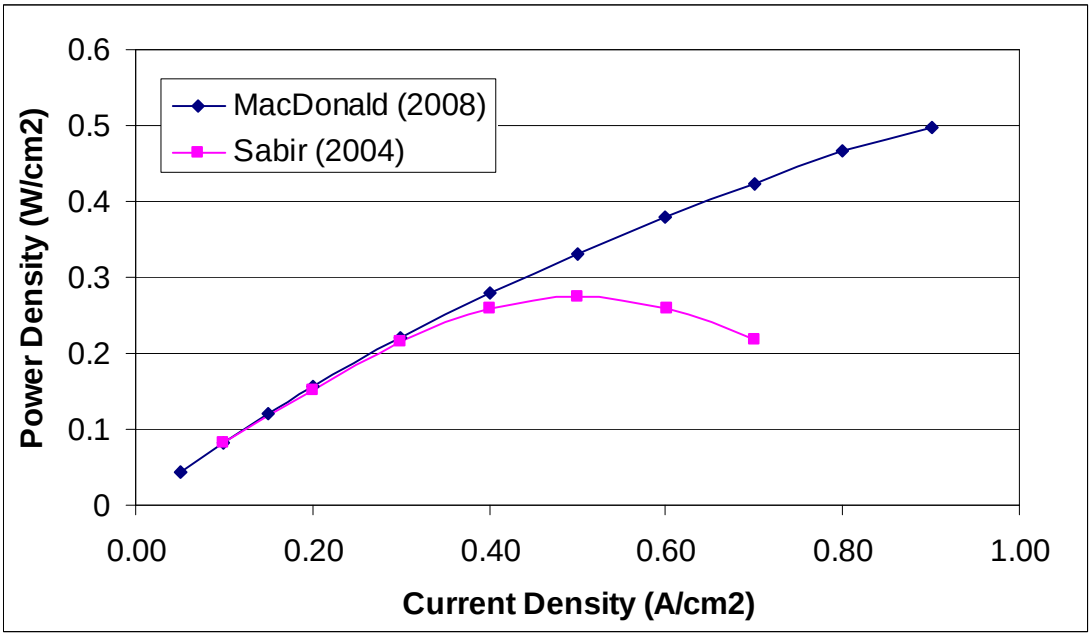

Figure 4.9: Power density comparison of current PEM fuel cell configuration with peer tested configurations

The case selected for comparison was chosen to be as similar to the peer tested cells as possible. Table 4.1 summarizes the test parameters for the two cases presented in the comparison. Though Sabir tested a number of configurations, in order to limit the affect of flow channel design, the comparison was limited a configuration that contained bi-polar plates with a single serpentine channel design. Visual inspection of Figure 4.8 and Figure 4.9 reveal that while the current assembly displayed similar performance to the Sabir design in the low current density range (< 0.3 A/cm^2) it displayed significantly higher cell potential and power output in the high current density range (>0.3 A/cm^2). This discrepancy was most likely due to the difference in the clamping force used in the two designs. The lower clamping force of the Sabir assembly would have a negative impact on cell performance, a phenomenon that will be discussed in more detail in the sections to follow. Other differences in cell parameters, such as 0.13 mg Pt/cm2 higher platinum loading and 0.3 higher anode stoichiometry would have benefited the Sabir design or had negligible impact. In order to further validate the present cell design, a second comparison with a commercially available

Table 4.1: PEM Fuel Cell Comparison Test Parameters

Case	MacDonald (2008)	Sabir (2004)
Pt. Loading (mg Pt/cm^2)	0.40	0.53
Cell Temperature (˚C)	80	80
Clamping Force (kN)	74.7	26.7
Cathode Stoichiometry	2.0	2.0
Anode Stoichiometry	1.2	1.5
Active Area (cm^2)	100	100

fuel cell power module was conducted, presented in Figure 4.10 and Figure 4.11 [70]. The Nexa™ Power Module, produced by Ballard, was selected for the comparison. The Nexa™ module was selected due to the availability of the performance data as well as the fact that Ballard is an industry leader in PEM fuel cell advancement and their cell performance would be indicative of the industry standard. Both cells operate on ultra high purity hydrogen as the fuel and air as the oxidant. Due to proprietary issues, very few cell parameters were

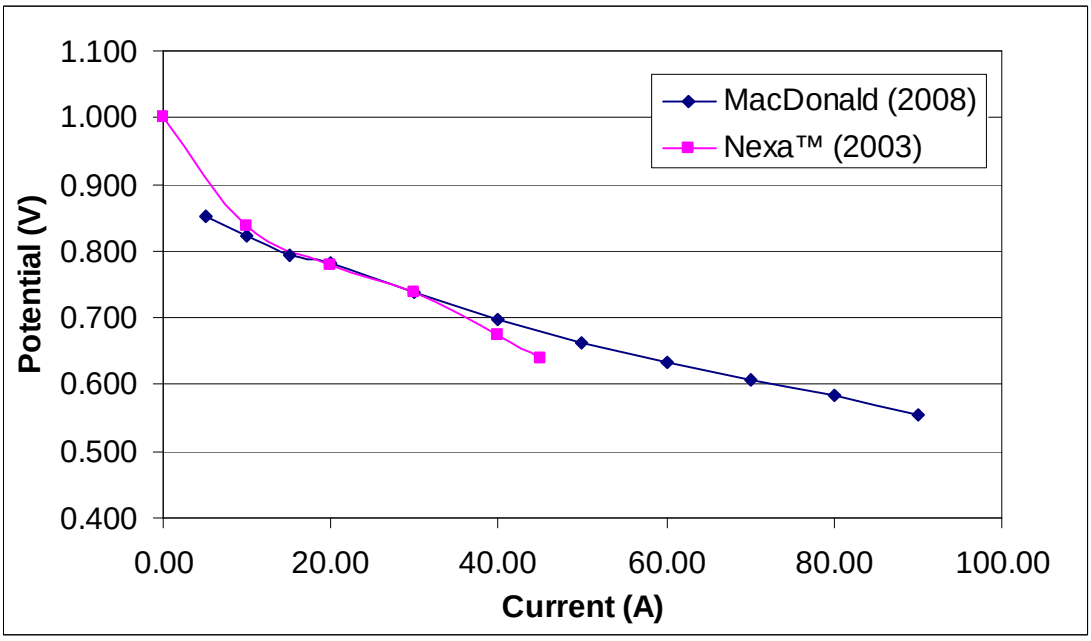

Figure 4.10: Performance comparison of current PEM fuel cell configuration with commercially available configuration

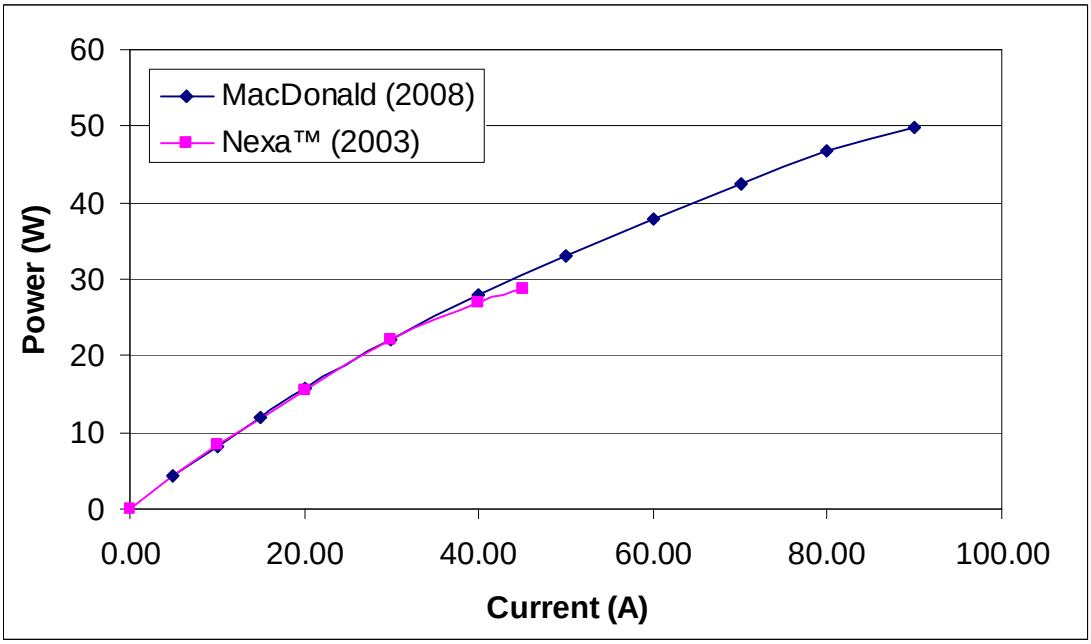

Figure 4.11: Power comparison of current PEM fuel cell configuration with commercially available configuration

provided with the module performance data; however for the purposes of this comparison, validation of the current design, the two assemblies were found to be sufficiently similar.

The data for the Ballard power module was extracted from performance data provided for the module stack, consisting of multiple cells arranged in series, and had to be scaled down to allow for comparison in terms of single cell performance. This process was facilitated by the availability of single cell operating reference points. The Nexa manual offered the complete stack power curve, along with the open circuit voltage (1 V) and approximate voltage at peak power (0.6 V) of a single cell. Since the cells are arranged in series, the total cell potential would be the sum of all the individual cell potentials. Dividing the total stack potential by the number of active cells, in this case forty three, would provide an estimate of the single cell potential and power. When compared to the reference data provided the estimated single cell performance showed excellent agreement, with a cell potential of 1 V and a peak power voltage approaching 0.6 V. Since no precise active area was provided for the Nexa™ module, although it was found to be close to 100 cm^2, data was presented in

terms of total current and power, as opposed to current density (A/cm^2) and power density (W/cm^2). Inspection of Figure 4.10 and Figure 4.11 reveals that the experimental design and the Nexa™ module yield similar cell potential and power outputs for the low current region of cell operation (<30A). The Nexa™ performance curve does not provide much information for the high current region (>30A), however the Nexa™ module appears to deviate slightly below the experimental fuel cell potential and power curves, indicating poorer performance beyond this region. The current experimental assembly performance was found to be in sufficient agreement with industry leading and peer tested designs and therefore was deemed to provide data relevant to the advancement of fuel cell research.

4.3 Preliminary Compression Analysis

Following the validation of the cell design a preliminary compression analysis was performed. This compression study aimed at investigating changes in flow and performance behaviour as a result of increasing cell compression, varied through applied torque. The factors potentially affecting cell performance, which were manipulated by cell compression, were identified. Once these factors were identified, they could then be analysed individually, in greater detail.

Using the assembly procedure, provided in section 3.2, several PEM fuel cells were assembled and sealed with varying torque values. The cells with varying compression were then run through the test procedure, including the flow and performance tests. The effect of this varying compression on cell performance will be discussed in this section. A general performance trend as a function of compression was identified. In addition, factors that are most greatly affected by cell compression were identified in order to identify all potential casual factors of this performance trend.

The fuel cell assembly was sealed with bolts tightened to four different torque values. The torque values ranged from 50-80 in-lbs and increased at an increment of 10 in-lbs. Fuel cell designs can vary significantly in the fasteners used in both size and number. Therefore

torque value alone does not offer a sufficient indication of the degree to which a cell has been compressed. It is imperative to offer a universal measurement that can be readily compared across a number of assemblies. For this reason the torque values were converted to a total clamping force using a bolt torque to clamping force conversion, provided in equation 7.

$$F_c = \frac{\tau \cdot N}{C \cdot D} \tag{7}$$

Where τ is the applied torque, N is the number of bolts used, D is the nominal bolt diameter, F_c is the resultant clamping force, and C is the friction coefficient. The friction coefficient has a value of 0.2, operating under the assumption that regular series nuts and bolts with rolled threads are used, acting on surfaces without lubrication. Table 4.2 summarizes the applied torque values and the resultant total clamping force.

Table 4.2: PEM Fuel Cell Clamping Force

Torque (in-lbs)	Total Clamping Force (kN)
50	53.4
60	64.1
70	74.7
80	85.4

The varying compression assemblies resulted in significantly different performance and power characteristics, displayed in Figure 4.12 and Figure 4.13. It can be seen from these figures that as compressive force increases, so too does cell performance, to a point. Beyond this optimal compression, cell performance dropped, revealing that over compression can hinder cell function. Another notable feature is the drastic increase in performance from the 64.1 kN cell and the 74.7 kN cell. Though both display similar performance in the activation region of the polarization curve, the 74.7 kN cell shows significantly increased performance in the mid and high current density regions, showing less sensitivity to ohmic and

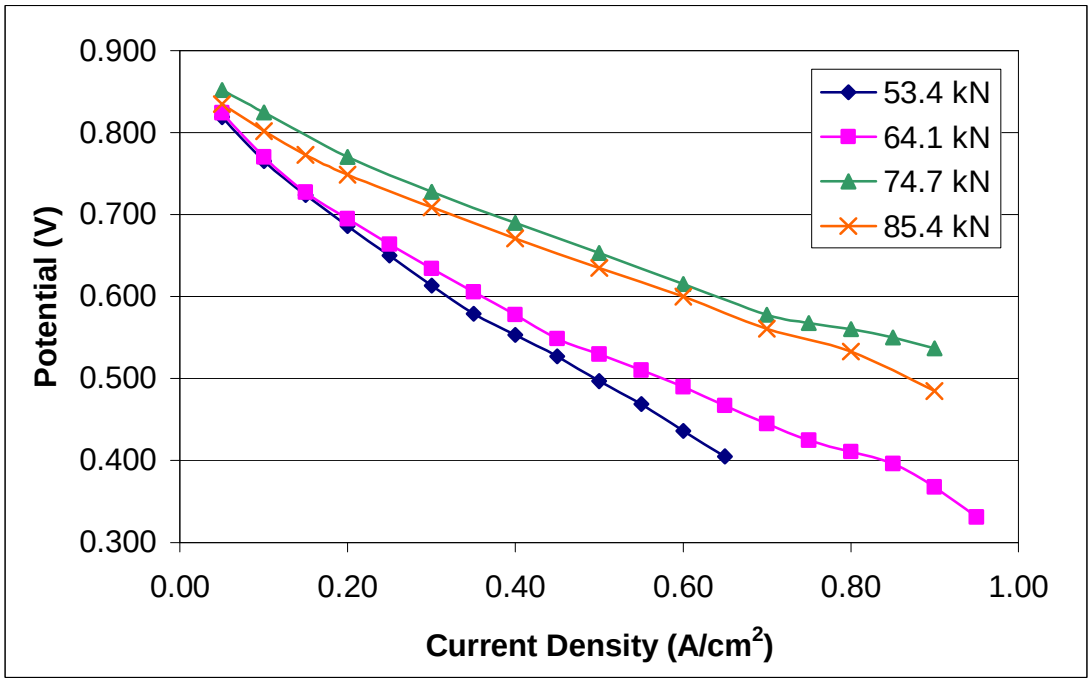

Figure 4.12: Effect of assembly torque on cell performance

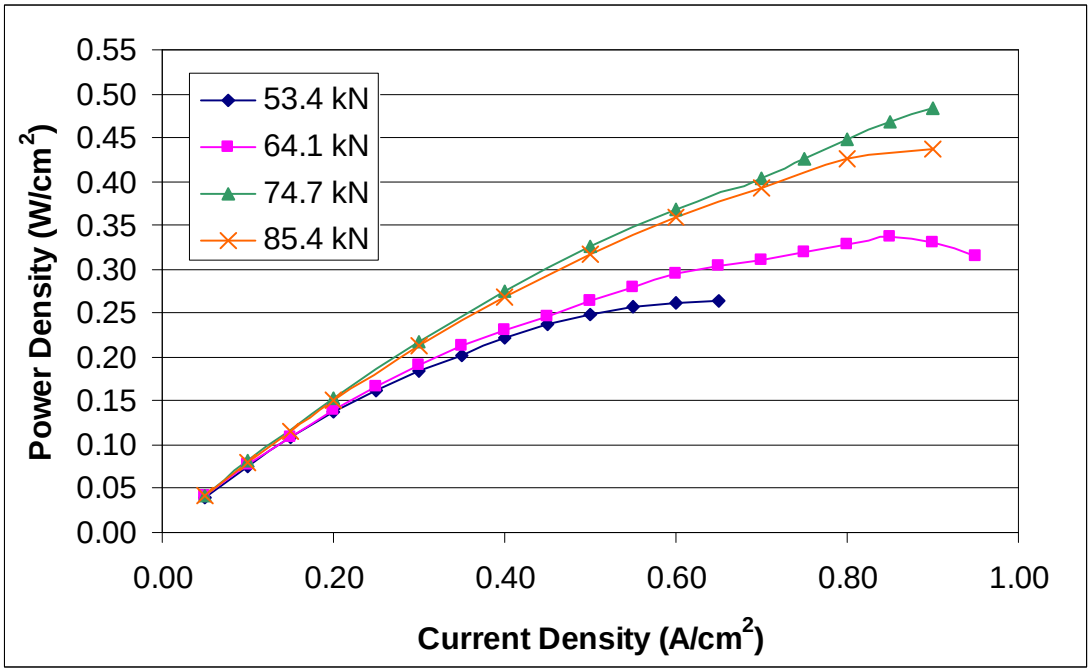

Figure 4.13: Effect of assembly torque on cell power density

concentration polarization. Inspection of the 74.7 and 85.4 kN curves reveals that the higher compression cell has only slightly reduced, but parallel performance over the low to mid current density region. However, in the high current density region (> 0.7 A/cm^2), the negative effects of the excessive compression became more evident. The 85.4 kN polarization curve begins to drop at an increased rate, resulting in the levelling off of the power curve, thus limiting peak power. The 74.7 kN displays an increasing power density curve in this high current density region due to the better performance entering the concentration region of the polarization curve.

To better understand this phenomenon of performance behaviour resulting from varying compression, one must understand the physical and environmental changes occurring within the cell during this compression. The physical structure within the cell undergoes significant change during compression. As the cell is compressed non-rigid materials within the cell compress, this would affect the gas diffusion layer and the silicon gaskets. Compression of

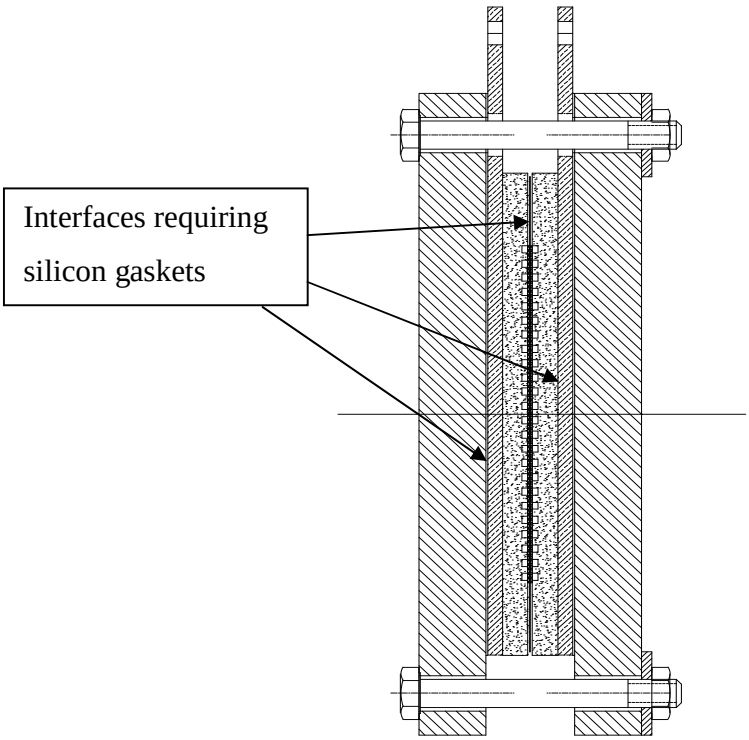

Figure 4.14: PEM fuel cell cross section

the silicon gaskets would result in increased sealing force, as it is the region where the gasket contacts solid cell materials where a tight seal is created. Figure 4.14 displays a fuel cell cross section and identifies the regions where this silicon sealing interface is required. Due to the multiple layer construction of a fuel cell assembly, proper sealing is critical in the proper delivery of the gas phase reactants to the reaction surface, the catalyst layer at the centre of the cell. In addition to improved sealing, increased compression in the silicon gasket would result in improved surface contact in the multi-layered cell. A lack of surface contact between the current collector and flow field plates or between the flow field plates and the GDL could drastically increase electrical resistance, thus limiting the ability of the cell to draw current and increasing voltage losses, effectively limiting cell power production.

Compression of the gas diffusion layer changes the physical properties of the GDL and the flow conditions within the cell. Increased compressive force results in a significant change to the flow field across the fuel cell flow channel, illustrated in Figure 4.15. The results displayed in Figure 4.15 were generated during the provided flow test procedure, by

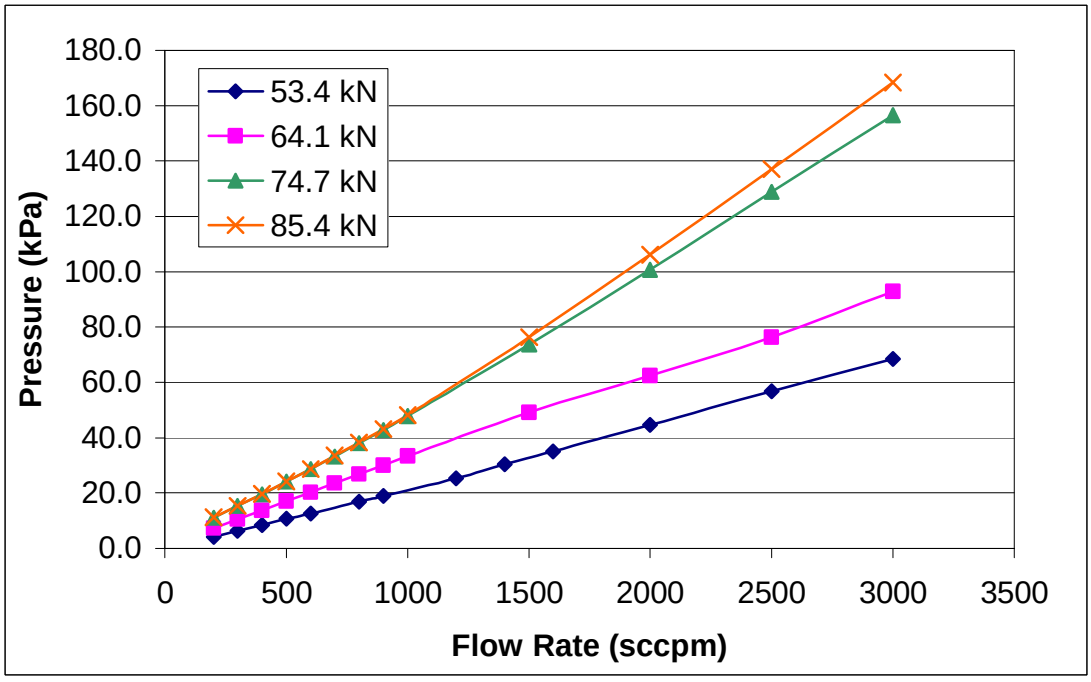

Figure 4.15: Effect of assembly torque on cathode pressure drop for dry air flow

applying an unconditioned air flow through the cathode flow channel. Examination of the results revealed that increasing compressive force resulted in an increased pressure drop across the flow channel, another factor possibly contributing to the varying performance results. The porous nature of the GDL would make it susceptible to changes in physical properties. Increased compression would result in a decrease of void space present in the GDL. The Bruggemann correction, forms of which are provided in equations 8 and 9, is a device typically used in modelling to relate the bulk physical properties to those displayed by a porous media. Here the correction is an effective tool used to display the effects of decreasing the void space, or porosity, on GDL physical properties.

$$\Psi_k^{eff} = \varepsilon_k^{1.5} \cdot \Psi_k \tag{8}$$

The form of the correction displayed in equation 8 would show the relation of properties found to be negatively affected by a decrease in porosity, such as diffusivity of a specific species, or more generally, permeability through the porous media. Another form of the equation, displayed in equation 9, is used to display the relation of properties positively affected by a decrease in porosity, such as electrical conductivity.

$$\Psi_k^{eff} = \left(1 - \varepsilon_k\right)^{1.5} \cdot \Psi_k \tag{9}$$

These changes in physical properties may also contribute to the performance behaviour displayed in cells of increasing compression, specifically permeability and electrical conductivity of the porous media.

To summarize, increased cell compression was found to result in increased fuel cell performance to an optimal point. Beyond this point increased compression was found to have a negative affect on the polarization and power curves. Critical factors resulting from the compression of the fuel cell, affecting these changes in performance, were identified to be, sealing force, pressure drop, permeability, and electrical conductivity. The effects of each of these factors on fuel cell performance will be analysed and their individual contribution to increased performance of a PEM fuel cell will be identified in the sections to

follow. Through this further study, it was hoped to identify whether each of these variables were a causal factor in the performance behaviour or were merely a neutral result of the cell compression.

4.4 Sealing and Surface Contact

Poor sealing and surface contact are undesirable in any fuel cell operation and were therefore isolated and eliminated. Multiple modes of leakage were discussed in this section, including external and internal leakage. A reliable method identifying their presence was also presented. A consistent symptom of incomplete surface contact was identified, it being a unique pressure response. The presence of this pressure response was then used to identify the presence of poor contact and quantify the performance gain as a result of proper sealing and complete surface contact.

Proper fuel cell sealing and surface contact are factors that can have a significant impact on fuel cell performance. A leak in the cell assembly can severely limit the ability of the cell to deliver the reactants to the reaction surface, drastically reducing cell efficiency. While a lack of sufficient surface contact can cause a significant increase in electrical resistance and result in voltage losses, thus limiting power production. However with proper cell design assembly techniques, these issues can be addressed.

The construction of a fuel cell assembly, consisting of multiple solid layer interfaces with gas transport between them, can make leak prevention difficult. Leaks have been broken into two modes, referred to by the author as external and internal. An external leak was defined as a leak between a sealed interface in the cell to the surrounding environment. This mode of leakage would most likely be caused by an opening in the silicone gasket, created by a tear or improper interface contact. It can also, but with less frequency, be caused by a physical deformation or crack in a solid layer of the fuel cell. This leakage occurs only in extreme cases and is more difficult to rectify as it usually requires a new part to be manufactured. An external leak was easy to identify as it was consistently detected using the

seal test procedure previously outlined. If pressure could not be maintained within a blocked cell flow channel then the cell had an external leak. This leak was rectified by disassembling the cell and replacing all silicone gaskets.

An internal leak was defined as a drastic deviation from the flow path inside the cell assembly. This type of leak can be more difficult to identify and precise care is required to prevent this phenomenon. The internal leak is typically the result of poor surface contact within the cell, specifically between the GDL and its surrounding solid media. This flow deviation is not to be confused with the flow deviation resulting from bulk motion into the GDL itself, but rather flow into an opening created by a gap between two media. As the flow will follow the path of least resistance, these gaps can cause the flow to completely bypass the reaction surface and significantly limit the cells performance. The gaps occur in two locations, around the perimeter of the GDL, between its edge and the interior gasket edge, illustrated in Figure 4.16, or between the GDL surface and the flow channel plate, shown in Figure 4.17. The perimeter gap is created by poor gasket and GDL design, simply put the GDL is too small or the gasket has been made too wide. This creates a gap around the GDL where flow can escape and bypass the reaction surface. To prevent this, extreme precision was ensured when cutting the media and assembling the cell. The GDL was designed for a precision fit, resting snugly on the interior gasket edge. Using gasket and GDL templates as a guideline was found to be an excellent practice to follow. This ensured consistent gasket and GDL sizes limiting variability to manufacturing tolerances. Another preventative measure was to develop a deliberate and precise assembly procedure so as to ensure that little unnecessary movement occurs when stacking the cell, outlined previously in the experimental procedure section.

Illustrated in Figure 4.17, the interface of the flow plate and the GDL is also a source of flow deviation. The gap could theoretically occur between the catalyst layer and the GDL, but pressure gradient in the through plane direction, created by the high pressure reactant flows, force the GDL onto the membrane surface. A gap at the flow plate surface is due to improper cell compression and insufficient surface contact. It can arise from the cell being under compressed, when the gaskets are not compacted to a thickness equal to that of the

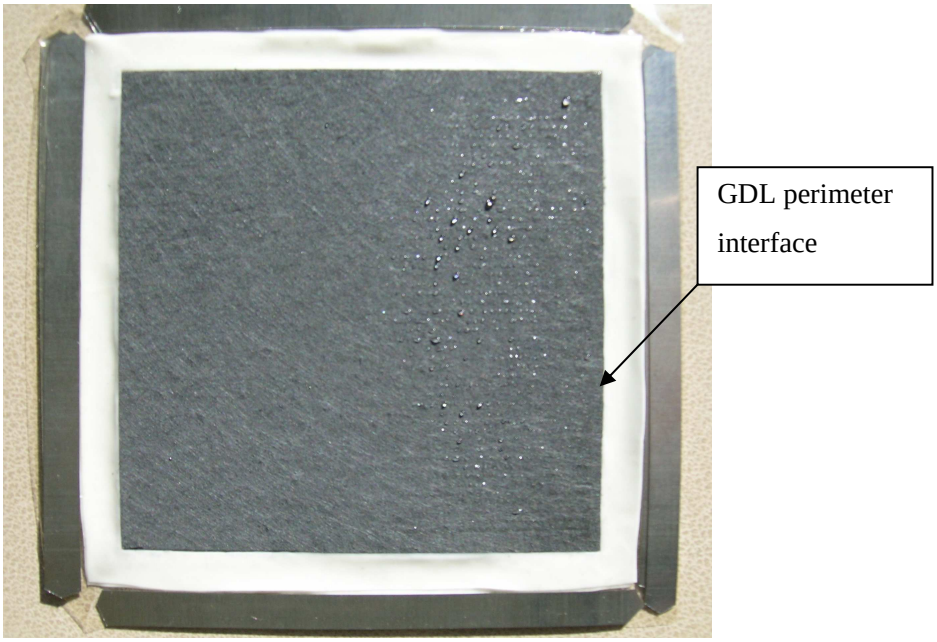

Figure 4.16: GDL and silicone gasket perimeter interface

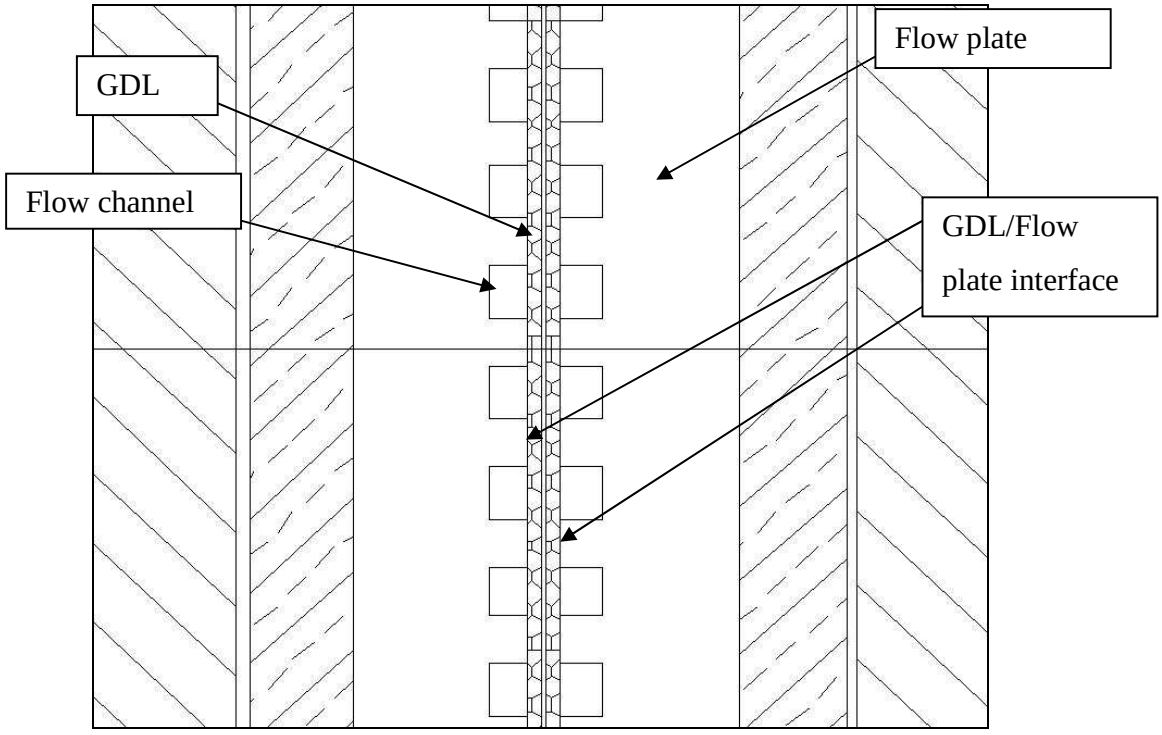

Figure 4.17: GDL and flow plate separation interface

GDL. A gap can also be created by uneven application of the compressive force. When one side of the cell assembly is over or under compressed, relative to the other edges, this can create a gap along the under compressed edge, resulting in a local flow deviation, limiting the ability of the cell to properly deliver reactants to the catalyst layer. As expected, this flow deviation would have a negative impact on performance.

In addition to creating a flow bypass, insufficient surface contact can significantly increase the resistance of the current collection circuit through the cell media. Proper current collection involves the transfer of electrons through the GDL to the flow plate and then through the flow plate onto the copper current collection plate. Improper contact at either of these surfaces would result in an increased electron flow path, and therefore would drastically increase resistance. If there was zero contact at these surfaces, the resistance would effectively increase to infinity, as the resistance to electron transfer through a gaseous media is extremely high. In both cases, increasing resistance would cause significant losses in cell potential, and negatively impact cell performance. Due to the relationship between proper surface contact and increased performance it was crucial to identify the flow behaviour resulting from these internal leakages, as well as identify the performance behaviour directly attributed to this lack of contact. Creating a scenario to identify the contribution of the contact to increased performance would allow for other compression factors, such as GDL compression, to be further analysed.

In an attempt to identify changes in flow and performance behaviour within the cell due to internal leakage and a lack of surface contact, the experimental cell data for cells with varying compression factors was compared against a control case. The control case was designed with specifications that would ensure poor surface contact. By creating a case where flow bypass and poor electrical conduction are guaranteed, one could identify similar behaviour in a cell where these phenomena were trying to be limited. To achieve these unfavourable conditions a change was made to the GDL gasket, increasing the thickness by 5 thousandths of an inch, or 127 microns. The increase in gasket thickness, while maintaining GDL thickness, would result in the presence of poor surface contact between the GDL and flow plate surface.

Figure 4.18 displays the results of the flow test for the control cell and those of the experimental compression cells. Inspection of the plot reveals excellent agreement of the pressure curve of the 254 μm assembly, with 53.4 kN compressive force, with that of the control case, with a 381 μm gasket. This suggests the presence of a similar flow field. Further examination reveals that the 254 μm cell with 64.1 kN compression possesses a pressure curve that is parallel to the 53.4 kN cell and the control case. Though the 64.1 kN case displays increased pressure drop, the parallel curve suggests similarity in the flow field. The similarity in the pressure curves indicates that the two lower compression experimental assemblies are also insufficiently sealed. The three similar, low pressure, cases display significantly different flow behaviour than the higher compression, 74.7 kN, case. The 74.7 kN cell has a higher pressure drop at the minimum flow rate, suggesting a different initial flow geometry. The flow also exhibits more sensitive pressure response to increased flow rate, as the rate of pressure drop increase with respect to flow rate is considerably larger than the two lower compression cases, 53.4 kN and 64.1 kN, and the control case.

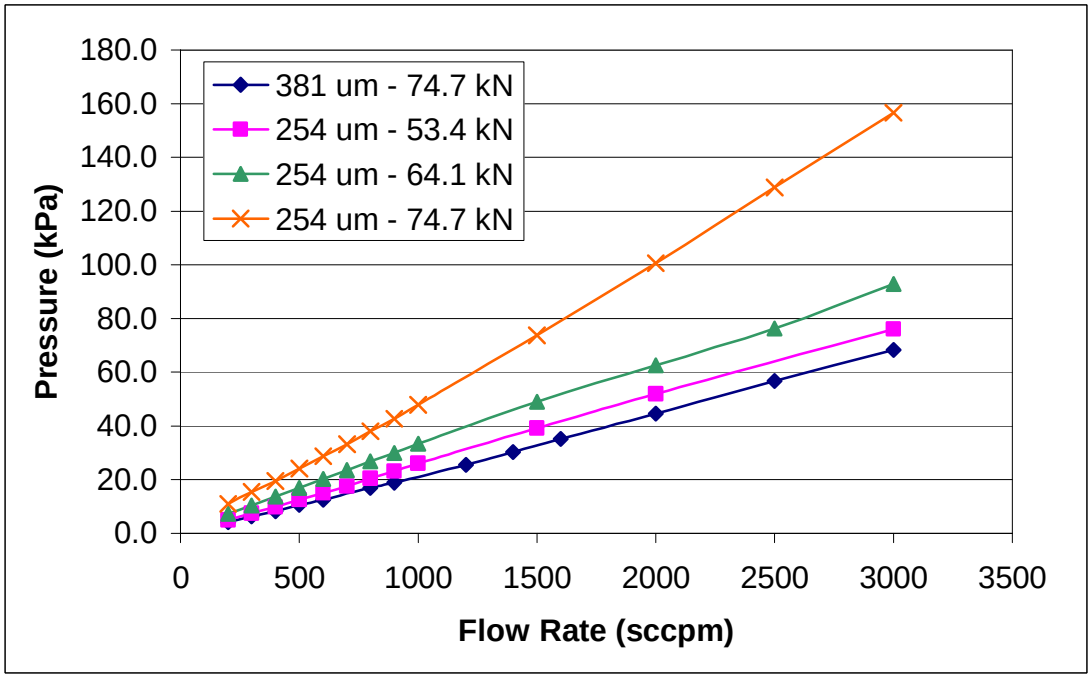

Figure 4.18: Effect of internal leakage on cathode pressure drop

The change in pressure response was due to a change in the flow field within the cell. The change in the flow field can most likely be attributed to proper surface contact and elimination of flow bypass. The presence of flow bypass resulted in reduced pressure response due to the fact that the flow, following the path of least resistance, was provided a flow path with significantly fewer obstacles. A flow with proper contact would force the flow through the narrow flow channel and would result in some degree of bulk motion through the porous GDL. Both of these paths offer greater resistance and pressure loss than an open flow field, created by a gap in the GDL/flow plate interface. This concept of changing flow fields due to changes in geometry as a result of varying compression will be discussed in greater detail in the section to follow.

This qualitative pressure analysis suggests that the lower pressure cases are improperly sealed while the high pressure case has sufficient surface contact and is properly sealed. Analysis of the performance results, displayed in Figure 4.19 and Figure 4.20, reinforced this hypothesis. The control case and the two low compression experimental cells display almost identical potential and power density response to increasing current density, with the 64.1 kN cell displaying marginally better performance at the high current density range, (CD > 0.5 A/cm^2). Due to the similarity in the performance response when compared to the control case, it was apparent that the two lower compression cases were also insufficiently compressed, possessed internal leaks, and lacked complete surface contact. Comparison of these poorly constructed cells with the highest compression configuration reveals the importance and significant benefits of proper sealing and complete surface contact. The 74.7 kN cell displays higher performance values over the entire current density domain, with the most significant gains in performance found in the middle to high current density region (CD>0.15 A/cm^2). These gains are due to decreases in ohmic and concentration polarization, losses that are dominant in those regions. The decrease in ohmic polarization can be attributed to the decrease in electrical resistance. This decreased resistance was a direct result of the proper surface contact in the high compression cell, providing a better flow path for the electrons extracted for current collection. The reduction of concentration

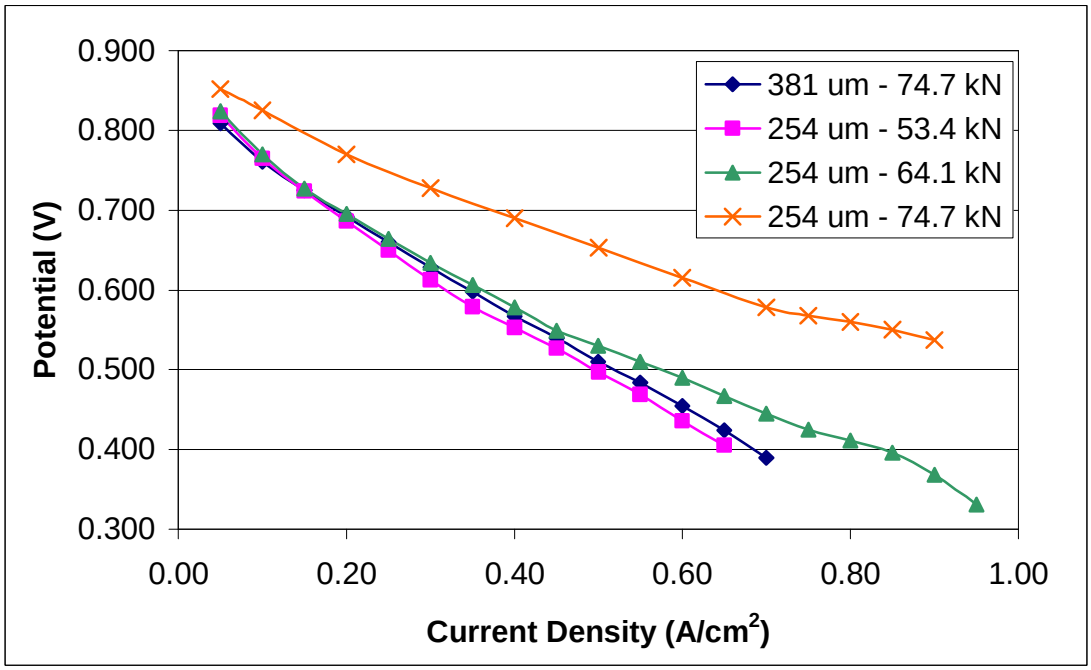

Figure 4.19: Effect of internal leakage on cell potential

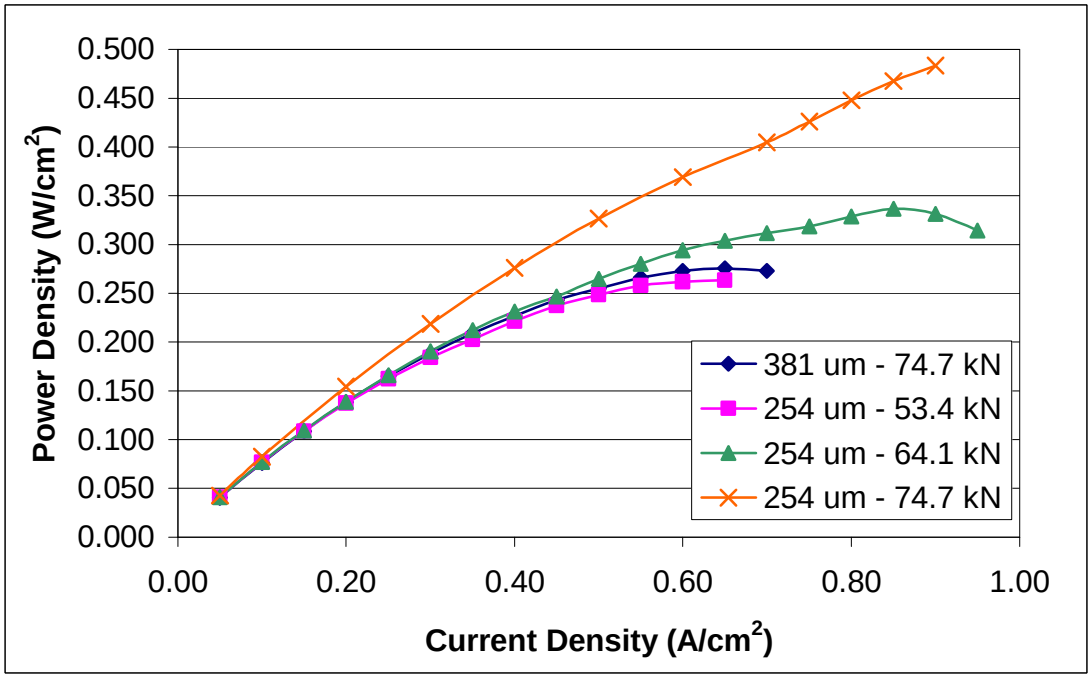

Figure 4.20: Effect of internal leakage on cell power density

polarization was due to the proper delivery of the cell reactants resulting from the elimination of flow bypass.

Poor sealing and surface contact within the fuel cell test assembly were isolated and eliminated. Multiple modes of leakage were identified and discussed, specifically external and internal leakage. A reliable method identifying their presence was presented and the performance gains attributed to proper contact was quantified. It was found that proper sealing and surface contact were essential to attaining optimal fuel cell performance. However, though sealing and surface contact were identified as dominate contributing factors to ensuring optimal performance, these performance gains could not be solely attributed to proper surface contact as other factors were not controlled. There exists the need to analyse the effect of the other factors affected by cell compression, specifically porosity in the GDL and pressure within the flow channel, independently, in a case where proper surface contact has been guaranteed.

4.5 Detailed Analysis

In order to consistently ensure proper sealing and surface contact as well as precisely control the degree of compression, a revised compression technique was required. Varying the applied torque was not a reliable method as it was difficult to apply subtle changes in compression. Once surface contact was eliminated as a variable, the effects of compression would most significantly affect the flow field and the GDL physical properties, both a function of GDL thickness. A technique to control GDL thickness, as opposed to applied compression force was employed. By introducing stainless steel shims, parallel to the GDL, its thickness would be maintained regardless of applied torque, so long as a minimum value was applied. This would allow for the detailed analysis of compressive affects beyond the sealing and surface contact. This section introduces the shim compression control design, and presents a brief study performed in order to confirm the integrity of the new shim assembly. Once the shim compression technique was validate the analysis of pressure and porosity contributions to changes in fuel cell performance was performed, both as a function

of cell compression. The results from this detailed analysis is provided in the subsections to follow.

It was found that proper sealing and surface contact were essential to attaining optimal fuel cell performance. However, beyond proper sealing, there were a number of factors previously identified to be affected by cell compression. It was found that subtle changes in assembly torque resulted in significant changes in flow field geometry and performance. This was due to the cell design that included twelve bolts contributing to the compressive force. Small changes in individual bolt torque values would multiply by a factor of twelve over the entire cell. As well, it was difficult to ensure even torque over the entire cell surface, as the precision of the wrench itself could not be guaranteed. Torque, alone, as a method to control compression was found to be insufficient. A new procedure that would ensure complete surface contact and ensure evenly applied compression was required. To satisfy these needs an assembly procedure that would control the thickness in the GDL, as opposed to compressive force, was applied. The control of thickness would ensure that proper contact was made, while also allowing for precise changes in compression without relying on precise torque application. The thickness was controlled through the application of stainless steel shims, placed in the gasket and GDL layer within the cell, illustrated previously in the apparatus description. The shims, selected at three thicknesses, all less than the GDL thickness, would offer resistance to compression, for any magnitude of applied torque, so long as it exceeded the value that was previously identified to provide proper sealing. For the GDL with an uncompressed thickness of 230 μm, shim thicknesses of 200, 150 and 100 μm, (8, 6 and 4 thousandths of an inch), were selected. The material selections were limited to brass and stainless steel. The steel was selected to its low reactivity and high resistance to corrosion. Conditions within the cell, high temperature and moisture content, are favourable for corrosion, and the presence of this phenomenon would be detrimental to the operation of the fuel cell. These shims would not only serve as a precise compression control, but would also allow for even GDL compression across the surface. By physically opposing over compression on any particular edge of the cell, the shims would guarantee that a consistent thickness on all edges was maintained.

While the shim offered a number of advantages to controlling cell compression, their presence could also potentially be a detriment to the cell. The biggest concern, was that the presence of a material with a high electrical conductivity close to the reaction surface could create a short in the system. This would cause the electron flow to pass through the shims as opposed to away from the reaction surface to the current collection plates. The solid polymer membrane was found to offer sufficient electrical resistance to prevent against such a scenario. However, if shims positioned on opposite electrodes were able to come in contact with one another, a short circuit would be created. This unwanted contact was found to arise through two different modes. The first was an electrical short created by shims that were in contact beyond the perimeter of the membrane. Care had to be taken to ensure that the shims were positioned in such a manner so as to remain within the total membrane area. The second mode was through a tear in the membrane. Though measures had been taken to soften the sharp edges of the steel, the compressive force of the cell combined with the fragility of the membrane material occasionally resulted in a tear in the surface. In this case the only solution was to replace the membrane as no current could be collected with the presence of the short circuit.

With proper precautions taken so as to avoid a short circuit of the current collection system, the integrity of the modified cell assembly was still in question, as the experimental response to the presence of the shims was still unknown. Though the theory behind the application of the shims was sound, a practical test was required to ensure proper pressure and performance response. The test would ensure that the cell displayed proper pressure change, to indicate a change in the flow field geometry. Also, an analysis of performance data was required in order to ensure this modified assembly displayed performance that was comparable to a conventional cell assembly. The results from the flow test for three varying shim assemblies are provided in Figure 4.21, this plot offers a comparison with the results from the high torque assembly and the low torque assembly, previously identified to have poor surface contact. Figure 4.21 displays that the three shim assemblies display varying

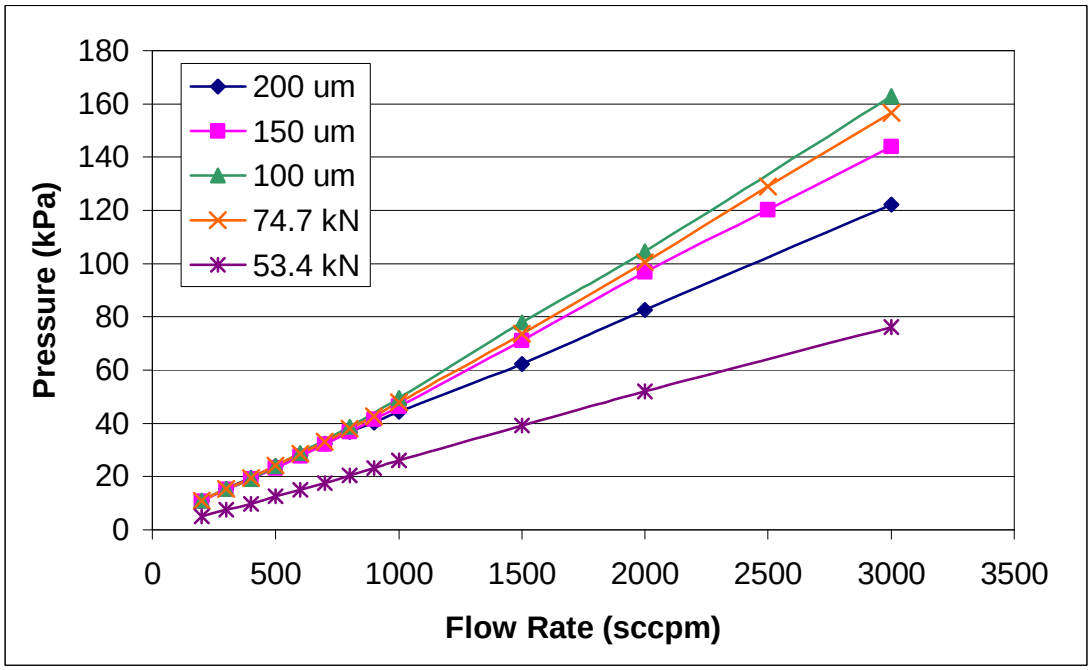

Figure 4.21: Integrity analysis of shim fuel cell assembly – pressure response

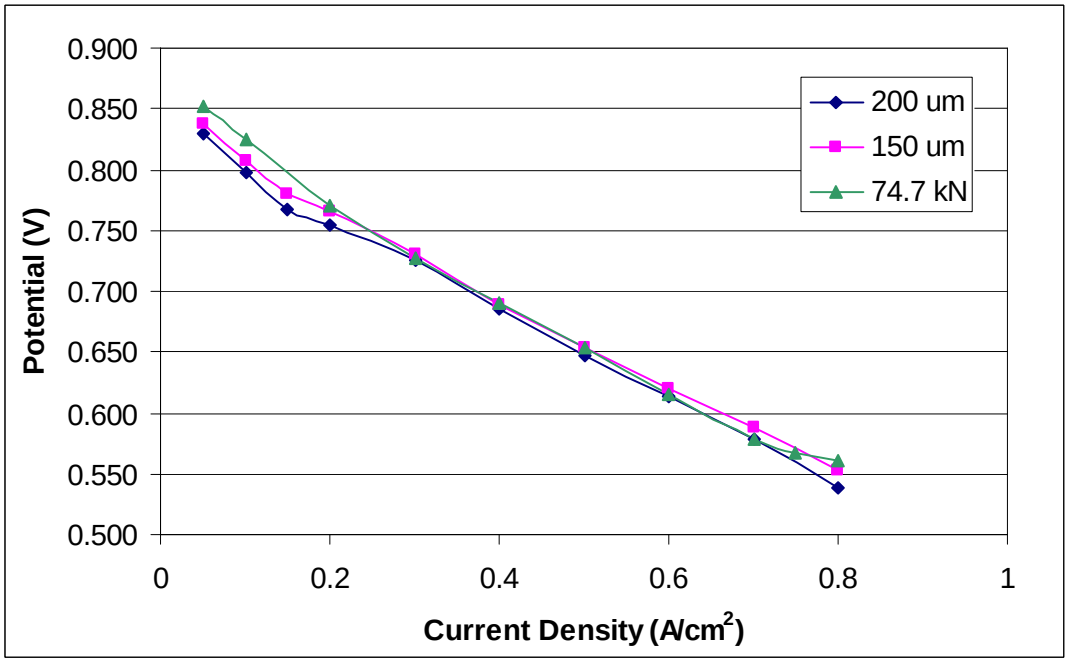

Figure 4.22: Integrity analysis of shim fuel cell assembly – cell potential

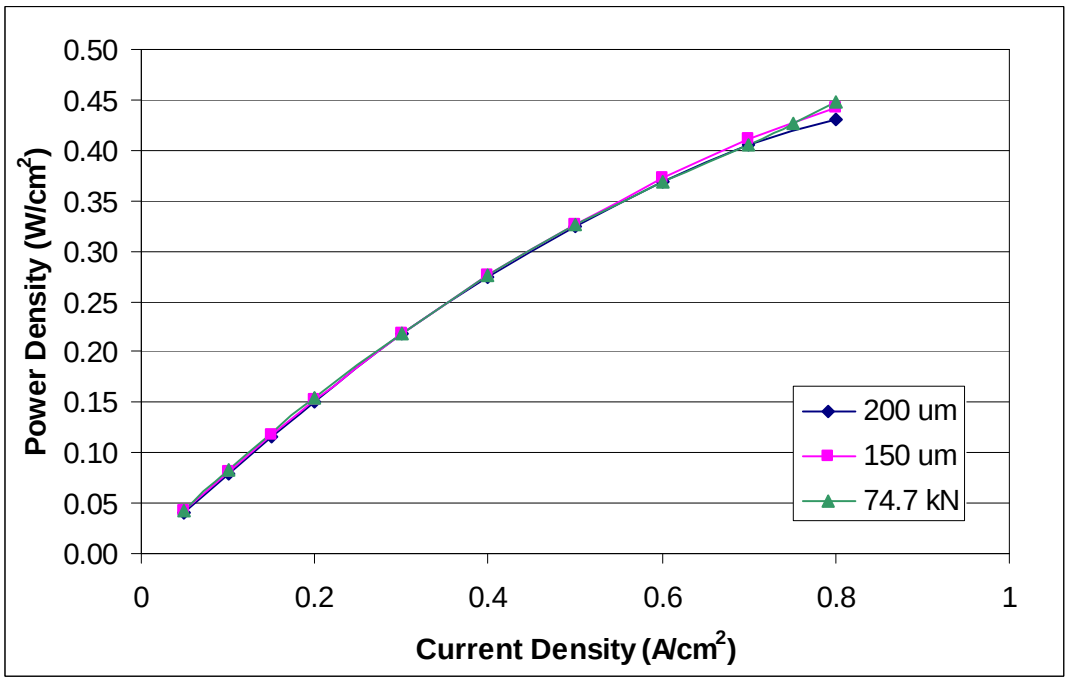

Figure 4.23: Integrity analysis of shim fuel cell assembly – power density

pressure response, indicating a change in flow geometry. While a comparison with the leakage flow test reveals that all three shim assemblies display pressure response indicative of proper sealing and surface contact.

Figure 4.22 and Figure 4.23 provide the results from a performance test for the 150 and 200 μm shim assemblies as well as the results from the conventional assembly with a compression torque of 74.7 kN. These plots reveal that the shimmed assembly displayed comparable performance with similar cell potential and power density results. The addition of the stainless steel shims to the fuel cell experimental assembly was found to have no negative impact on cell performance and flow fields. The shim compression method provided sufficiently accurate experimental data while offering precise compression control.

4.5.1 Pressure Analysis

The effect of varying pressure response, as a result of increased compression, was investigated as a performance variable and is presented in this section. In order to gain a better understanding of the mode of pressure variation in the flow field, a theoretical model was developed to simulate a known flow scenario. This scenario was then compared to the pressure drop results for the experiment in order to identify a trend in pressure response. Once a trend was identified, increased pressure drop for increasing compression, the pressure could be manipulated via the test station for performance tests of cells with varying compression, on the scale that it changed in the various compression thicknesses, in order to ensure equal pressure. Through a comparison of the performance results for the cells operating at equal pressure but varying compression, the contribution of pressure to changes in performance was then quantified.

As was mentioned in a previous section, an increase in cell compression force resulted in an increase in the slope of the pressure vs. flow rate curve, Figure 4.15. Leakage and lack of surface contact was presented as one cause of this phenomenon, however the physical change in the structure of the GDL can also contribute to this increase in pressure drop. In order to develop a better understanding of this phenomenon, a theoretical model was developed, in this section, to model the flow through the channel in the cell flow plate. This model, using fluid dynamic relations, would calculate the pressure drop of a flow passing through a rectangular flow channel with the same geometry as those found in the flow field plate in the experimental cell. This model could then be compared against the experimental pressure drop data in order to identify the mechanism for increasing pressure. The increased compression of the fuel cell was also found to result in an increase in performance, to a point. Following the theoretical analysis, this section investigated the relation of pressure and performance gains. Using the shim compression control method the effect of cell compression, and changing flow geometry on pressure drop was displayed, independent of any leakage effects. Once this change in pressure was quantified the effect of the magnitude of this pressure drop on cell performance was investigated. By creating an induced pressure drop, through manipulation of inlet pressure, in a low compression, 200 μm, cell, equal to or

greater than that experienced by the high compression cell, one could determine the effect of this change in pressure on performance. If the pressure was a significant causal factor, the low compression cell would display the performance increase similar to the found in the high compression cell.

Due to the difficulty in affectively modelling the flow with a porous boundary wall, the channel was assumed to have solid walls on all sides. Before the model was derived, a calculation of the Reynolds number was performed at all flow rate values, in order to determine nature of the flow, laminar or turbulent. The calculation for the Reynolds number in a rectangular duct, provided in equation 10, is based on the hydraulic diameter of the channel.

$$\mathrm{Re}_{D_h} = \frac{\rho \cdot V \cdot D_h}{\mu} \tag{10}$$

Table 4.3 summarizes the results from these calculations at the higher end of the flow domain, 1500-3000 sccpm. It was found that the flow entered the laminar-turbulent transition region, $2000 < \mathrm{Re} < 4000$, at a flow rate of 2000 sccpm and reached a maximum Reynolds number of 3175 at a flow rate of 3000. Despite the presence of turbulent transition, a majority of the flow domain was found to be laminar, for values less than 2000 sccpm, and since no reliable friction coefficient exists in the transition region the flow was assumed to be laminar throughout the entire domain. The total pressure drop through the

Table 4.3: Summary of Reynolds number calculations

Flow Rate (sccpm)	Reynolds Number
1500	1587
2000	2116
2500	2646
3000	3175

channel was modelled as the sum of two sources of pressure loss; losses due to friction and minor losses, represented by equation 11.

$$P_{TL} = P_f + P_m \tag{11}$$

The pressure drop due to friction was modelled by the formula presented in Equation 12 [71].

$$P_f = \rho \cdot g \cdot h_f \tag{12}$$

The head loss due to friction can be calculated, based on a hydraulic diameter of the flow channel, according to equation 13.

$$h_f = f \frac{L}{D_h} \frac{V^2}{2g} \tag{13}$$

The friction factor was extracted from tabulated values of $f\,\mathrm{Re}_{D_h}$, which was predetermined for a duct with a rectangular cross section for varying ratios of width and height. Using the previously calculated Reynolds number, these tabulated values could be isolated for the friction coefficient, presented in equation 14.

$$f = \frac{C}{\mathrm{Re}_{D_h}} \tag{14}$$

Equations 13 and 14 were substituted into equation 12 and simplified to form a more practical form of the friction loss relation, presented in equation 15. Velocity was taken to be the average velocity, determined by the flow rate, $V = Q / A_c$. The value of C for the flow channel in the experimental cell, for a width to height ratio of 0.91 (a/b = 1/1.1) was taken to be 56.91.

$$P_f = \frac{\mu \cdot C \cdot L \cdot Q}{2 \cdot A_c \cdot D_h^{\,2}} \tag{15}$$

The minor losses are also calculated with reference to minor head loss, displayed in equation 16.

$$P_m = \rho \cdot g \cdot h_m \tag{16}$$

In this case the head loss is also proportional to the flow inertia and is calculated by the relation provided in equation 17.

$$h_m = \frac{K \cdot V^2}{2 \cdot g} \tag{17}$$

After substituting equation 17 into equation 16 the minor loss equation takes the form provided in equation 18. Once again the average velocity has been calculated as the ratio of volumetric flow rate to the cross-sectional area of the duct.

$$P_m = \frac{\rho \cdot K}{2}\left(\frac{Q}{A_c}\right)^2 \tag{18}$$

The value for the loss coefficient can be taken from literature, Maharudrayya et al. [72] presented correlations for the minor loss coefficient in the laminar region. The correlations are provided for three flow regimes, and are presented in equations 19-21.

For Re < 100

$$K = 0 \tag{19}$$

For 100 < Re < 1000

$$K = 0.46\left(\mathrm{Re}^{\frac{1}{3}}\right)\left(1 - 0.18Cu + 0.016Cu^2\right)\left(1 - 0.2ar + 0.0022ar^2\right) \times \left(1 + 0.26\left(\frac{L_s}{D_h}\right)^{\frac{2}{3}} - 0.0018\left(\frac{L_s}{D_h}\right)^2\right) \tag{20}$$

For 1000 < Re < 2200

$$K = 3.8\left(1 - 0.22Cu + 0.022Cu^2\right)\left(1 - 0.1ar + 0.0063ar^2\right) \times \left(1 + 0.12\left(\frac{L_s}{D_h}\right)^{\frac{2}{3}} - 0.0003\left(\frac{L_s}{D_h}\right)^2\right) \quad (21)$$

Using the above equations the theoretical pressure drop for an air flow across the cathode flow channel was calculated. The fluid properties for air were taken at 20 ˚C and 1 atm. These values were then compared to the experimentally derived pressure curves at varying degrees of cell compression, illustrated in Figure 4.24. Inspection of the comparison reveals that the theoretical pressure curve increases at a greater rate than the experimental curves. This indicates that an air flow restricted to the flow channel would incur a much greater pressure drop than that of a flow enclosed by a porous media on one side. The flow within the experimental channel has deviated from the theoretical flow as a result of the presence of two physical factors, the presence of internal leakage and bulk motion into the porous GDL. Internal leakage, discussed in the previous section, is the result of poor surface contact which creates a flow gap. This gap allows for flow bypass as the gap offers a path of lower resistance, and results in a reduced pressure drop. When proper surface contact is ensured, the amount of void space contained in the porous GDL controls the deviation in the flow path from the channel, commonly referred to as cross flow. Using the controlled compression method, these flow tests were performed again, the results of which are provided in Figure 4.25. As compression of the GDL was increased, the void space within the porous GDL decreases. This would result in the GDL behaving more as a solid media and would therefore create a flow field within the channel closer to that represented in the theoretical model, enclosed by solid walls on all sides. Though this comparison reveals the mechanism behind the increased pressure drop, the effect of this pressure on cell performance, if any, must also be investigated.

As was previously revealed, increasing cell compression resulted in increased performance, to a point. To reveal the effects of pressure as an independent factor

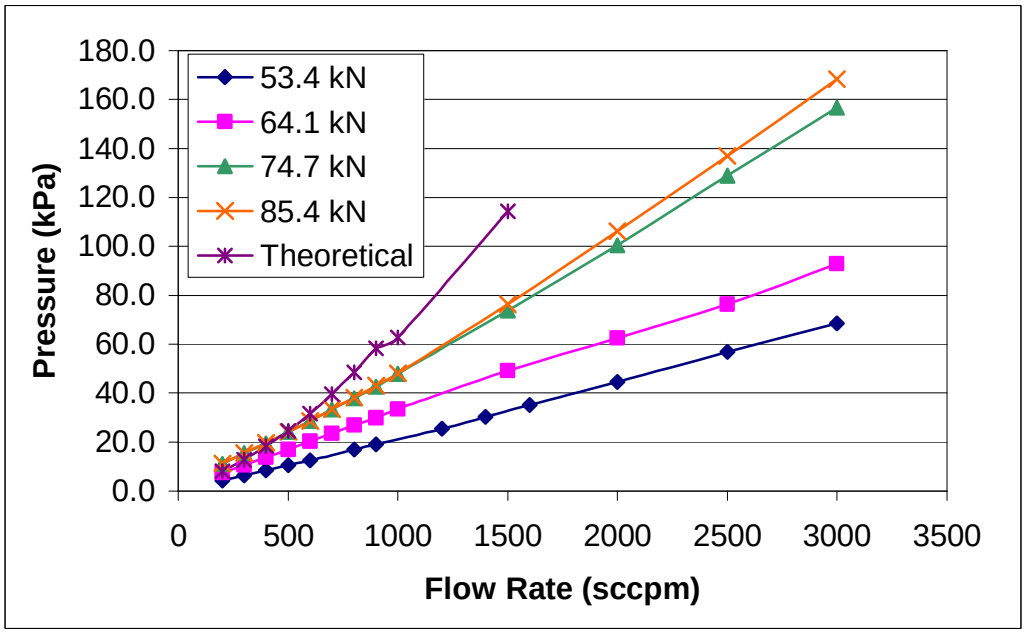

Figure 4.24: Theoretical cathode pressure drop comparison with experimental results at varying cell compressions

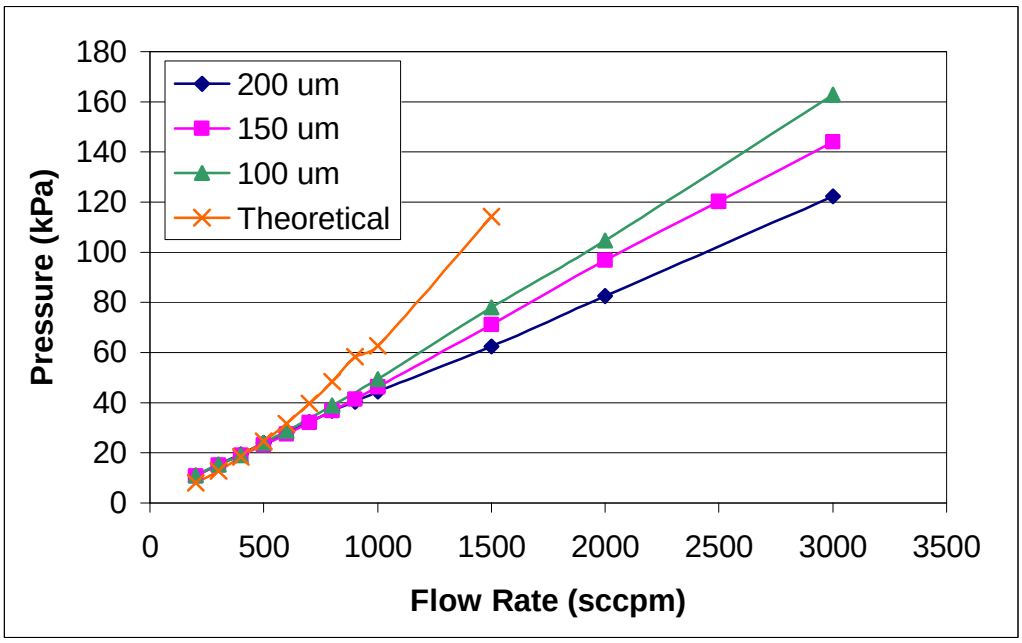

Figure 4.25: Theoretical cathode pressure drop comparison with experimental results for controlled compression technique

contributing to this increased performance two cells with different degrees of compression, 100 and 200 microns, were compared. The cell with the lesser degree of compression was then exposed to an induced pressurization, creating a pressure scenario similar to that of the cell with greater compression. The effect of this pressurization was then compared to the performance of the higher compression cell in order to display the effect of this relative pressure disparity on the increased performance. The logic being that if cell performance were a result of increased pressure, then a cell with poorer performance would see a performance boost as a result. All variables were controlled as both cells were assembled with the same specifications, with the exception of degree of compression. Figure 4.26 illustrates the dry pressure curves for the 100 and 200 micron cells. This plot reveals that these curves display the same pressure relationship of the previously analyzed varying torque curves that increased compression resulted in an increased pressure drop. Variation in these curves can be directly attributed to varying GDL porosity, as internal sealing was ensured in the shimmed assemblies. Figure 4.27 illustrates a comparison of the operational pressure curves of the two cell assemblies in question, as well as the pressure data for the induced pressure curve for the 200 micron cell.

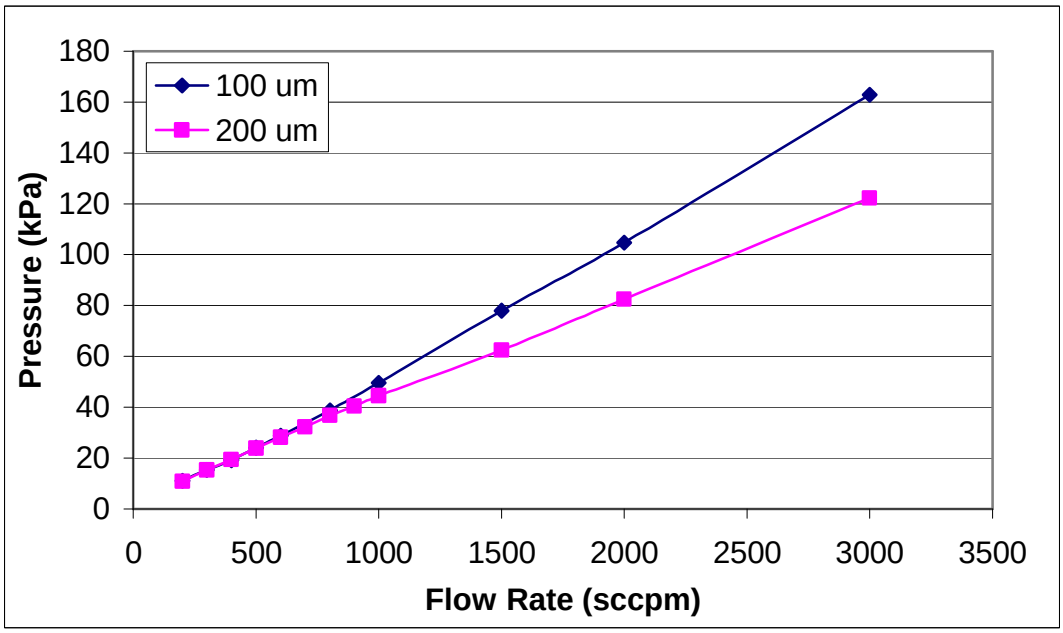

Figure 4.26: Comparison of cathode pressure drop for dry flow scenario at 100 and 200 μm

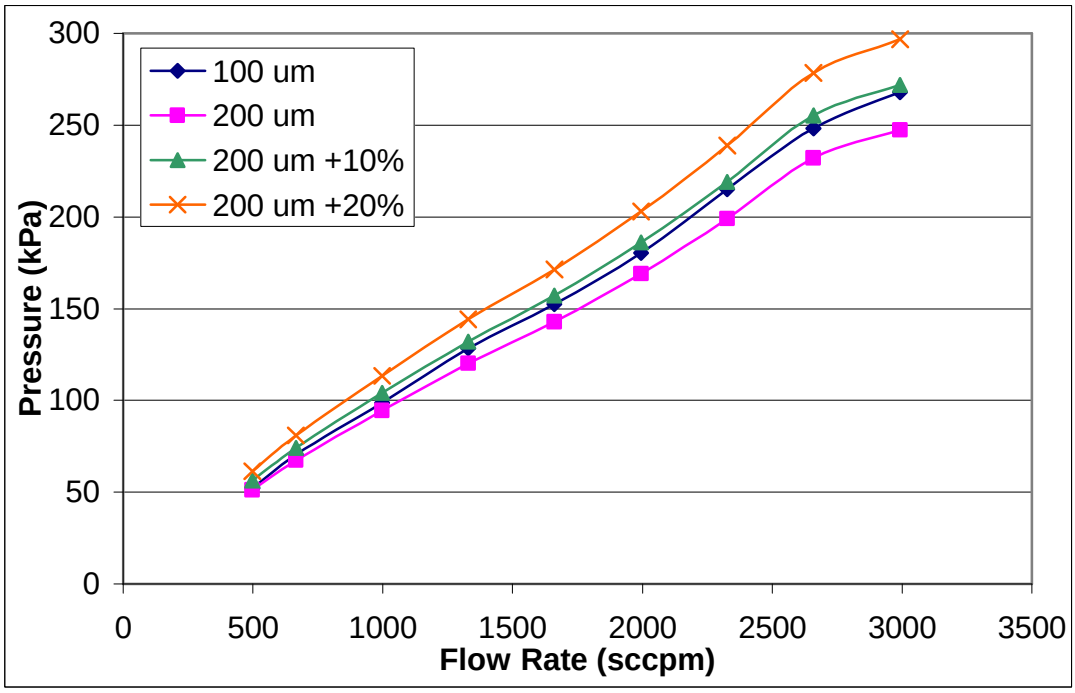

Figure 4.27: Comparison of cathode pressure drop for operational flow scenario and 100 and 200 μm

The artificially induced pressure was increased at an increment of 10% of the original operational pressure curve to a maximum of 120% of the original value, creating two additional sets of performance data. Inspection of the operational pressure plot reveals that the assembly, increased by a factor of 10%, displayed good agreement with the 100 micron pressure behaviour.

Performance data was generated for all of the aforementioned pressure configurations, the results of which are presented in Figure 4.28 and Figure 4.29. Inspection of the plots reveals that the induced pressure resulted in a negligible change increase in cell potential and power density, while the 100 micron cell displayed significant performance increase over the 200 micron assembly. To clarify these phenomenon a portion of the high current density data was isolated and displayed at a larger magnification and was provided in Figure 4.30. Analysis of the data, summarized in Table 4.4, reveals that at their peak value, for a current density of 0.7 A/cm^2, a 10% incremental increase in pressure resulted in a slightly greater

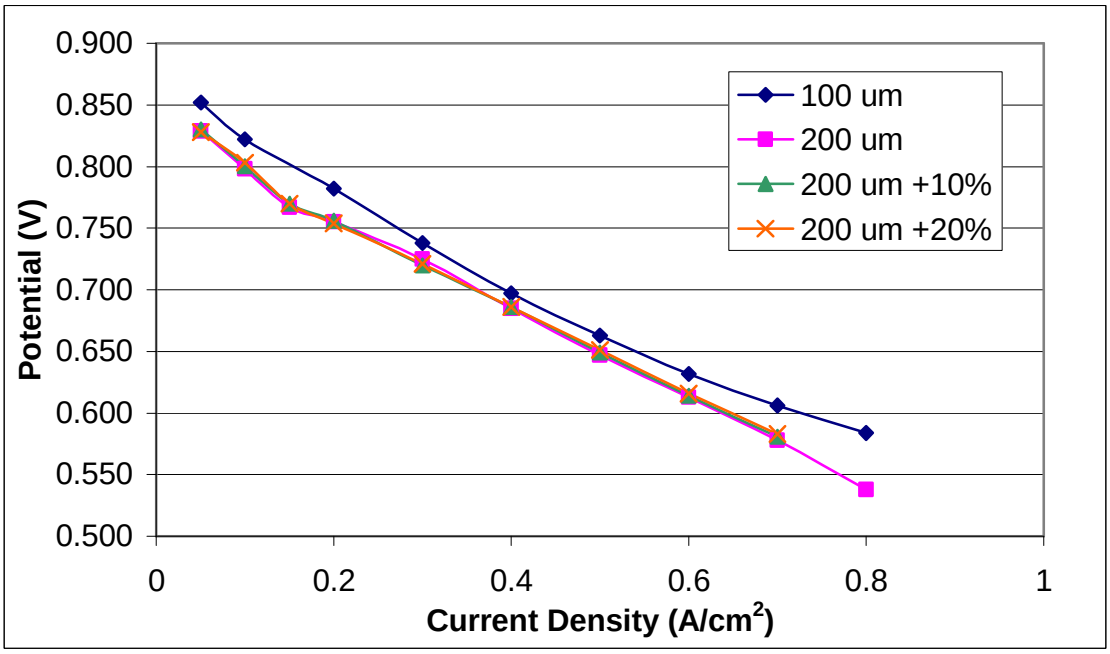

Figure 4.28: Effect of induced pressurization on cell potential

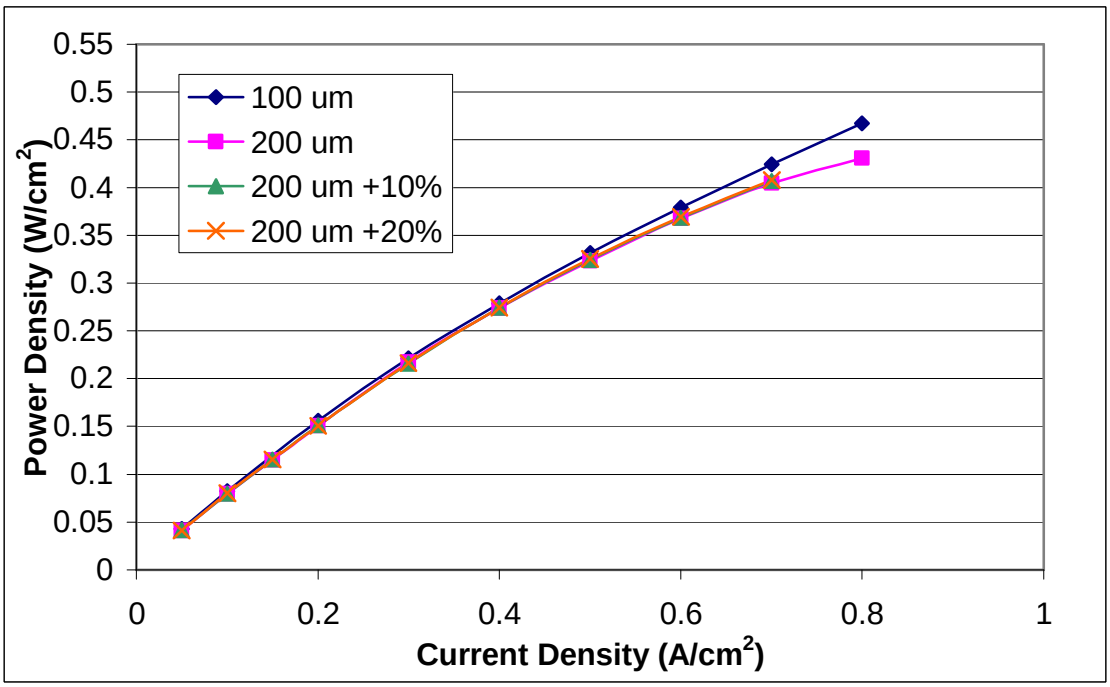

Figure 4.29: Effect of induced pressurization on cell power density

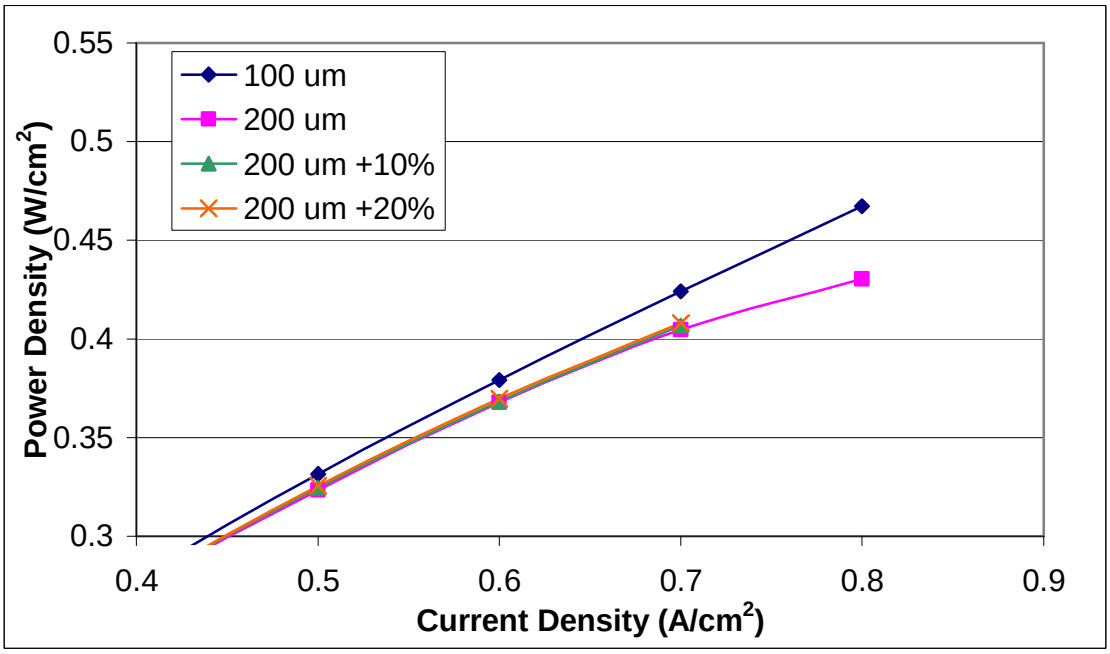

Figure 4.30: Effect of induced pressurization on cell power density for higher current density region (CD > 0.4 A/cm^2)

Table 4.4: Summary of pressure and power density changes at 0.7 A/cm^2 with reference to 200 micron base case

GDL Thickness (µm)	Pressure Increase (%)	Power Density Increase (%)
100	8.4	4.84
200	10	0.52
200	20	0.87

than 0.5% increase in performance. While the 100 micron cell displayed a performance increase of roughly 5%, with a similar increase in pressure as that displayed by the 200 micron configuration, with pressure induced to 110%.

An increase in cell compression was found to result in an increase in pressure drop across the cell flow channel. This pressure increase was investigated and was found to be inherent of a change in the flow field in the cell, forcing the flow to follow the channel in the flow

plate and limited bulk motion into the porous GDL. Following an analysis of experimentally generated cell potential and power density data, it was found that an increase in pressure, on the scale of changes found in the varying cell compressions, was a neutral, not a causal, factor in the performance behaviour of the experimental fuel cell assemblies.

4.5.2 Porosity Analysis

It was found that pressure was not a causal factor in the performance variation in a fuel cell, on the degree to which it varied due to changing compression. The performance response must then be attributed to variation in the physical properties of the GDL imposed by these varying degrees of compression. Compression of the GDL would decrease the porosity, as a compacted GDL would fold in on itself, filling the void space with its own solid media. The decrease in porosity would result in changes to the physical properties in the porous media. The properties of particular interest are permeability and electrical conductivity, as these would have the greatest impact on cell performance. In this section, changes in these properties, with respect to changes in porosity are estimated using correlations from literature. Once a general trend in physical properties was established, the effects of these changes on performance of the fuel cell were analysed. The performance behaviour was presented in terms of cell potential and power density data, collected through controlled compression, experimental testing. The limiting factor of fuel cell performance was identified and the benefits of precision fuel cell compression were quantified.

An increase in the degree of compression resulted in a decrease in the GDL porosity, which in turn altered the physical properties of the diffusion layer. A change in porosity was estimated by determining the volume of void space eliminated during each compression. Assuming that the total volume of solid remained constant, and that changes in GDL total volume were due to the reduction of void space alone, the porosity at varying degrees of compression were evaluated using equation 22.

$$\varepsilon_c = 1 - \frac{1-\varepsilon_o}{V_{GDL,c} \diagup V_{GDL,o}} \tag{22}$$

Compression in this manner would limit the GDL to change in the thickness dimension only, similar to the compression of an accordion, the GDL would fill in its own void space, thus satisfying conservation of mass, and not expanding in the surface plane direction as it would experience negligible solid plastic deformation. This was further confirmed through inspection of the GDL following testing. The thickness of each GDL was measured after each experimental run and was found to be equal to the value measured before compression. Had the GDL experienced plastic deformation, the thickness would have been found to be less than that of the uncompressed pre-test GDL.

Due to proprietary reasons the amount of material property data supplied for the GDL was limited. The manufacturers supplied porosity of the uncompressed sample, average filament diameter, and electrical resistivity in the through-plane direction. The through-plane is the direction perpendicular to the GDL surface. An important property, air permeability, however, was not supplied. This is not uncommon in the ever developing field of fuel cell material manufacturing, as companies wish to protect their product advancements. Also, even in cases where permeability has been supplied, no guarantee of the accuracy of this value is provided. The value is determined through any one of a number of permeability test methods, and is rarely identified when results are provided. It's also in the manufacturer's best interest not to provide accurate results, but rather, results that enhance their products standing in the market. However, this did not present an obstacle in quantifying permeability of the sample as a number of accurate estimation techniques have been developed to determine permeability as a function of porosity and filament size and orientation. One such correlation is the Kozeny-Carman relation, provided in equation 23.

$$K = \frac{\varepsilon}{K_c}\left(\frac{V_p}{S_p}\right)^2 = \frac{\varepsilon \bar{r}^2}{4K_c} \tag{23}$$

This is one of the most broadly used relations in the study of porous media, however, it has limitations. While the method offers an accurate estimation, it requires the evaluation of a constant, K_c, which typically is found through experimental methods. This constant can be estimated in most cases to be approximately equal to 5, but values that vary by two orders of magnitude have been reported in literature. A more accurate and robust model has been presented by Tomadakis and Robertson [57], displayed in equation 24. The correlation was developed through a conduction-based method, presented by Johnson et al. [73].

$$K = r^2 \frac{\varepsilon}{8\ln^2 \varepsilon} \frac{\left(\varepsilon - \varepsilon_p\right)^{\alpha+2}}{\left(1-\varepsilon_p\right)^{\alpha}\left[(\alpha+1)\varepsilon - \varepsilon_p\right]^2} \tag{24}$$

This equation provides the permeability constant, K, as a function of porosity, filament diameter, and filament orientation in the porous media. For the GDL used in the experimental study, the filaments were aligned randomly in the 2D direction, but were stacked in the thickness plane, illustrated in Figure 4.31. The variables and constants for this filament orientation are summarized in Table 4.5. Once the appropriate constants have been determined, equation 24 then becomes a function of porosity and can be evaluated at varying degrees of compression. The correlation was compared against experimentally determine permeability values and was found to be accurate, on average, to within 25%, for any range of porosity.

Table 4.5: Tomadakis-Robertson equation parameters 2-d random fibre structure

r (μm)	ε_p	α	
		through-plane	in-plane
3.5	0.11	0.785	0.521

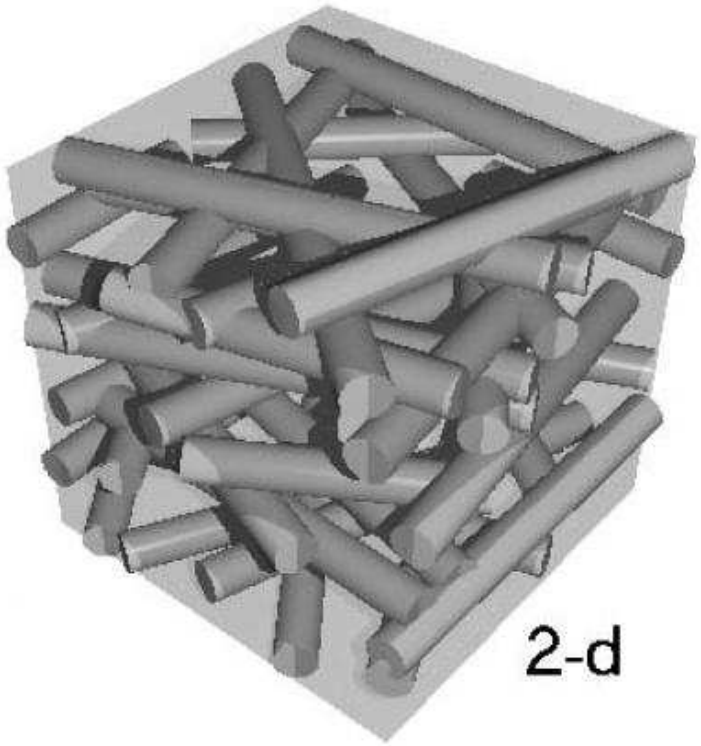

Figure 4.31: GDL filament arrangement – two dimensional random fibre structure [57]

The resistivity of the uncompressed GDL was supplied by the manufacturer, 80 mΩ-cm. This value was converted to conductivity by taking its inverse and converting to appropriate units and was found to be 1250 S/m. In order to model the change of conductivity over the domain of changing porosity the Bruggeman correction theory was applied, provided in equation 25.

$$\sigma^{eff} = (1-\varepsilon)^{1.5} \cdot \sigma_s \tag{25}$$

The solid media conductivity can be difficult to approximate due to the presence of multiple sold materials in the GDL, which includes the filament material, a proprietary matrix material, which is a carbon based adhesive, and PTFE, a Teflon coating. However, the model can be manipulated to determine the value for the initial condition, for which effective conductivity was provided. Following this procedure the solid media conductivity

was found to be 12,100 S/m. The above theoretical correlations were evaluated over the experimental domain of porosity. Values for through-plane and in-plane permeability as well as electrical conductivity were estimated. The results from these evaluations were summarized in Table 4.6.

Table 4.6: Summary of permeability and conductivity for changing cell porosity

		Permeability		Electrical Properties		% change	
ε	t (μm)	through-plane (m^2)	in-plane (m^2)	resistivity (mΩ-cm)	conductivity (S/m)	through-plane	conductivity
0.78	230	2.92E-10	6.47E-12	80.0	1250	0.0	0.0
0.75	200	2.40E-10	4.35E-12	64.9	1542	-17.9	23.3
0.66	150	1.61E-10	1.77E-12	42.1	2373	-45.1	89.9
0.49	100	9.21E-11	3.52E-13	22.9	4360	-68.5	285.4

The table confirms the previously mentioned changes in physical properties. Through-plane permeability was found to decrease by 68.5 % while conductivity through the GDL was found to increase by 250%. This information alone does not offer much insight to the resultant performance behaviour of the cell. Although the conductivity was found to increase at a relatively greater percentage, this alone would not necessarily be the dominant contributing factor as each variable contributes to performance in varying degrees. To determine the effects of these changes on the performance of the PEM fuel cell, controlled compression performance tests were conducted, the results of which are presented in figures 4.32-4.34

Figure 30 displays the pressure response for the cathode dry air flow. It reveals the increase in pressure drop, indicative of the increased GDL compression. This confirmed that the three cell assemblies were compressed at three sufficiently different compression values. Figures 4.33 and 4.34 display the cell potential and power density response for the exposed current density domain. These plots reveal that, when all other factors are controlled,

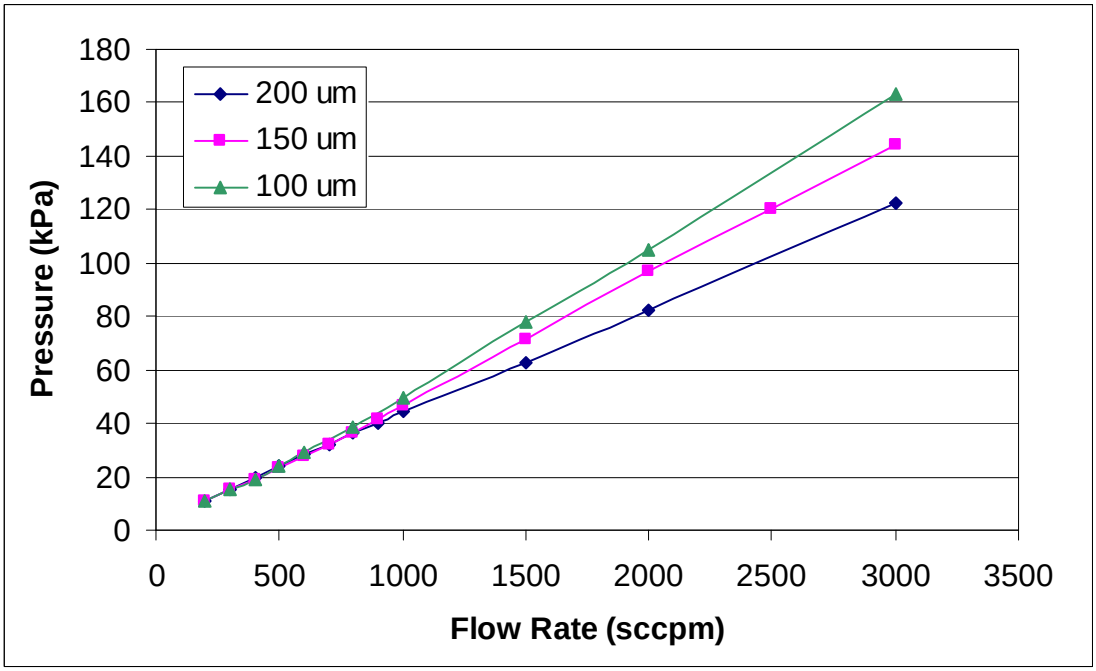

Figure 4.32: Effect of controlled compression on fuel cell pressure response

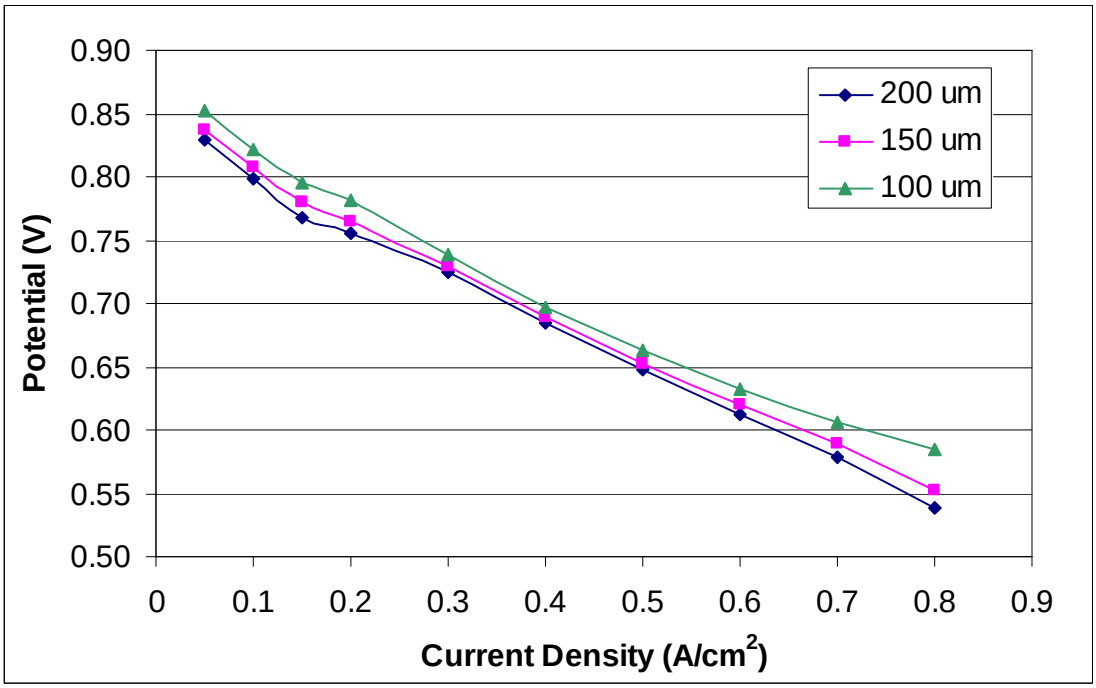

Figure 4.33: Effect of controlled compression on fuel cell performance – cell potential

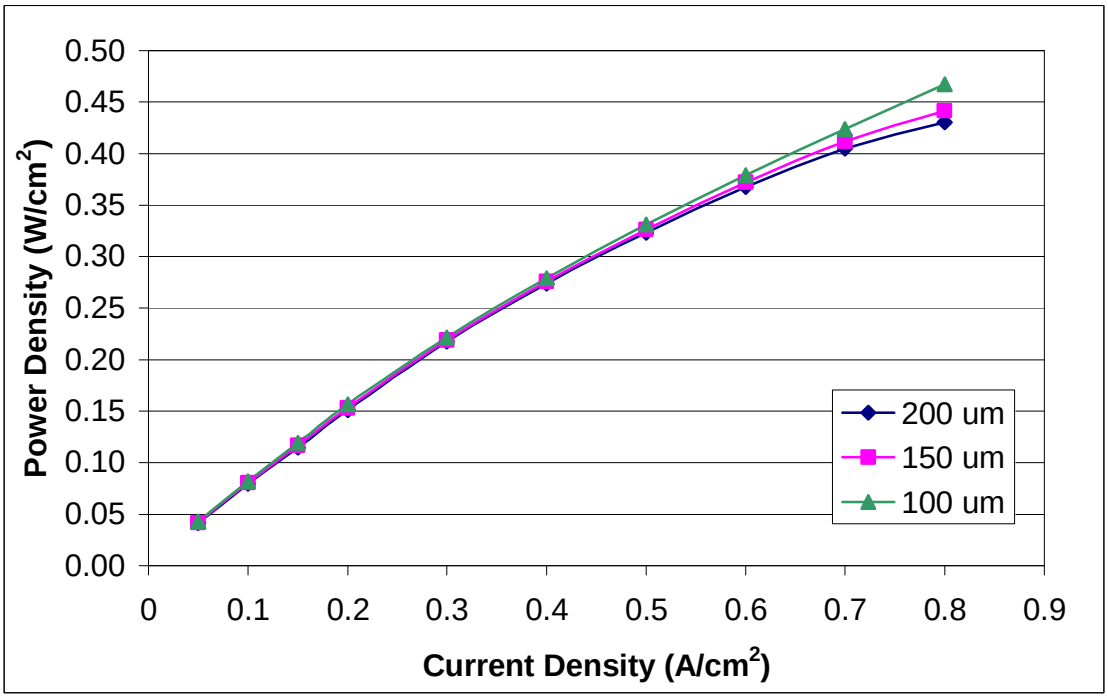

Figure 4.34: Effect of controlled compression on fuel cell performance – power density

compression still results in the increased performance over the current range in question. The 100 micron cell displayed the highest potential and power density values, with an increase of 8.6% with respect to the 200 micron cell, at a current density of 0.8 A/cm^2. As was discussed in the literature review, a number of sources have presented the concept of a proportional relationship between permeability and cell performance. Theorizing that for increased permeability, the cell can deliver a greater proportion of the reactants to the catalyst surface, and that this increase in mass transport would result in better performance. However these results suggest that this is not necessarily the case. For further insight into this phenomenon the polarization curve for the experimental results was compared to the general polarization curve for a PEM fuel cell, illustrated in Figure 4.35. From this figure we can see that the experimental curve follows the shape of the general curve in the activation and ohmic regions. However the experimental curve does not fully present the concentration region of the curve. The fuel cell experiment was limited by the operational cathode pressure, as it reached the maximum allowable value of 250 kPa beyond the current

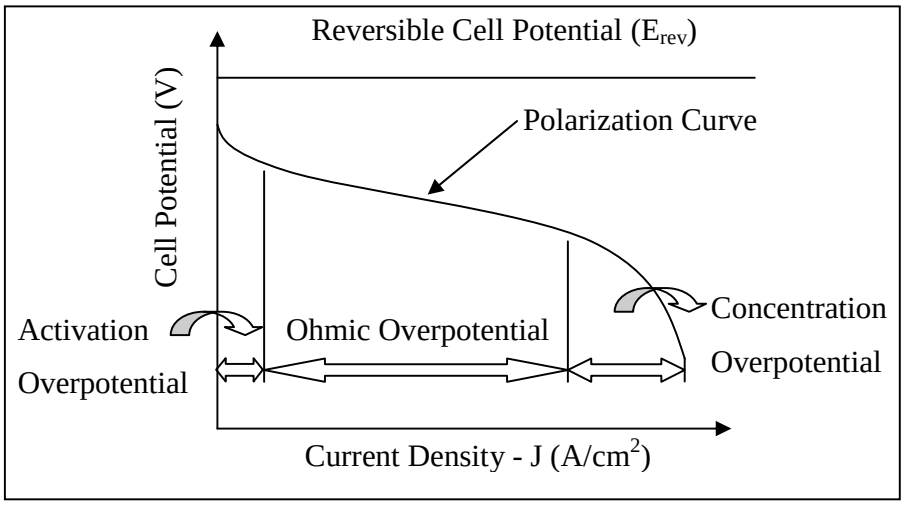

Figure 4.35: Typical PEM fuel cell polarization curve

density value of 0.8 A/cm^2. To proceed beyond this point would have compromised experimental accuracy and could have potentially damaged the station and the cell itself. Most fuel cells operate in the ohmic polarization region, as this is where peak power is obtained and where predictable performance behaviour is displayed, as current density is directly proportional to ohmic overpotential. For this reason ohmic overpotential is the limiting practical factor in fuel cell power density and cell potential. The physical changes found within the cell, caused by manipulating compression, were found to positively influence conductivity while negatively influencing permeability. An increase in conductivity would result in an increase in the overall cell conductivity which would contribute to decreasing ohmic overpotential. A decrease in permeability, which would increase the resistance to mass transfer to the reactant surface, would most significantly affect the concentration overpotential region, where reactant supply is most significant in dictating losses. Since the ohmic overpotential was found to be the limiting factor in the operational current density domain of the fuel cell, the increase in conductivity was the dominant factor in cell compression contributing to a change in cell performance. This is not to say that increased compression will always result in an increase in performance, there are limitations to this relationship. Park and Li [66] have found that through-plane permeability below 10^{-12} m^2 would result in the GDL behaving as a solid media, allowing for

very little mass transfer to the reactant surface. This would suggest that a minimum value of permeability, or reactant mass transfer, through the GDL must be maintained in order for performance benefits to be displayed. In the case of over compression, the reaction rate would be choked and this would result in the decreased permeability becoming the dominant limiting performance factor. Inspection of Table 4.6 reveals that the theoretical permeability was estimated at 9.21E-11, which would suggest that any compression beyond 100 μm would result in over compression. While no controlled compression was available beyond 100 μm, as this was the smallest available shim thickness, over compression could be investigated through a large increase in applied torque. Figure 4.36 and Figure 4.37 display a performance comparison of the 100 μm cell and one assembled with a compressive force of 85.4 kN, a result of an applied torque of 9.04 N-m (80 in-lb).

The cell compressed at 85.4 kN performs significantly poorer than the 100 μm cell. While the over compressed cell displays weaker performance over the entire current density domain, the discrepancy is the greatest at the higher current density region (CD>0.5 A/cm^2). At the highest measured value of 0.9 A/cm^2 the 85.4 kN assembly displays a 12.5% drop in potential and power density with respect to the 100 μm cell performance. This performance drop can be related to the early onset of the concentration polarization region. The increased demand for reactants placed on the over compressed cell in the high current density region cannot be met, due to the reduced mass transfer capabilities of the GDL.

Another factor that would result in the onset of concentration polarization would be liquid water flooding of the GDL. The accumulation of liquid water in the GDL can effectively decrease the porosity and limit the reactant mass transfer to the catalyst layer. The absence of the concentration polarization in the experimental performance results can also be attributed to the excellent water management capabilities of the test cell. It has been presented in literature that the micro-porous layer, PTFE GDL coating, and serpentine flow channel, all equipped in the test assembly, limit the accumulation of liquid water while maintaining sufficient electrolyte humidification [74].

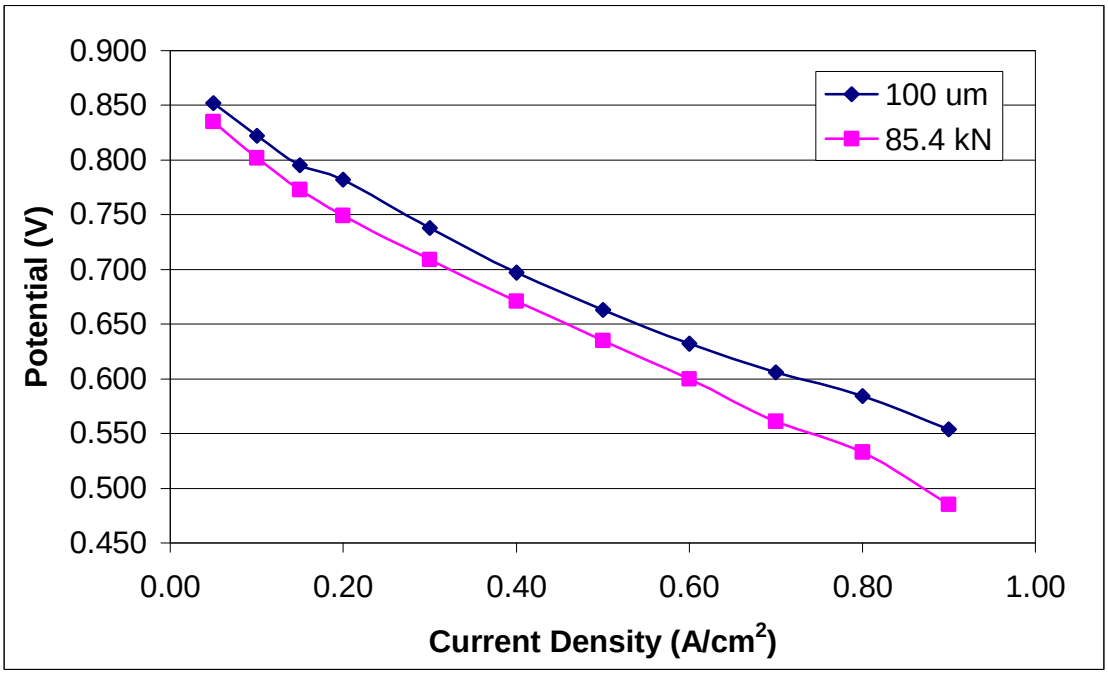

Figure 4.36: Effect of over compression on cell potential

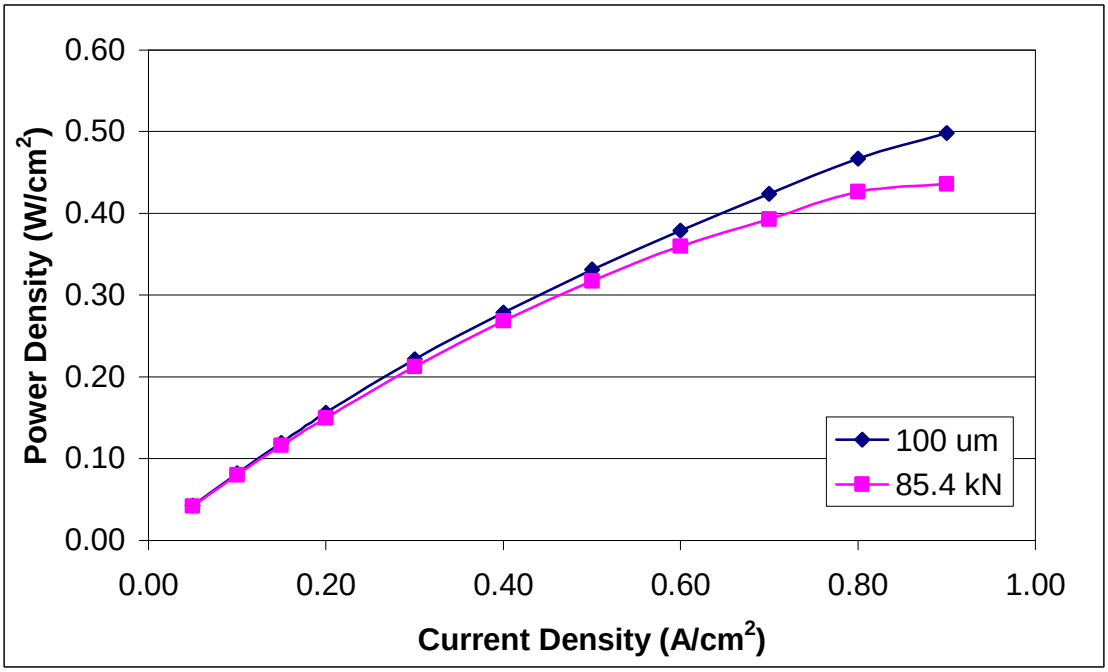

Figure 4.37: Effect of over compression of cell current density

This analysis reveals the importance of precise cell compression. Though increased compression was found to have significant performance benefits, due to improved electrical conductivity, the benefits occur only to a point. Beyond this point, continuing compression was shown to have significant negative impact on cell potential and power density, due to an inability to properly supply reactants to the electrolyte.

4.6 Platinum Loading

As is the goal with any PEM fuel cell research, it is hoped that this study will aid in the progress toward vast commercialization. As was previously mentioned, high cost of the system, a significant portion of which is due to the high cost of platinum loading on the catalyst layers, has been a major obstacle in this progression. As platinum loading is reduced in fuel cells, control of operational variables has been found to be more important in maintaining optimal performance. The sensitivity of cell compression to changes in platinum loading was investigated. To analyse this sensitivity, performance results of a given cell compression thickness were compared at two catalyst platinum loading values, 2 and 4 mg Pt/cm^2. The variation in this performance as platinum loading was increased could be compared at the varying thicknesses. This comparison would offer insight into the sensitivity of the previously studied performance benefits, resulting from varying cell compression, to changes in platinum loading. Figure 4.38 and Figure 4.39 display the performance results generated for a compression of 100 μm. While Figure 4.40 and Figure 4.41 provide the results for varying platinum loading for a cell with a 200 μm compression.

Visual inspection of the performance plots suggests that cells with lower compression display higher sensitivity to changes in platinum loading. The increase in performance for the 100 μm cell, due to the increase in platinum loading, was less than that of the 200 μm cell, or inversely, that a 200 μm cell would display a larger decrease in performance should the platinum loading be decreased. This suggests that as steps are taken to reduce the

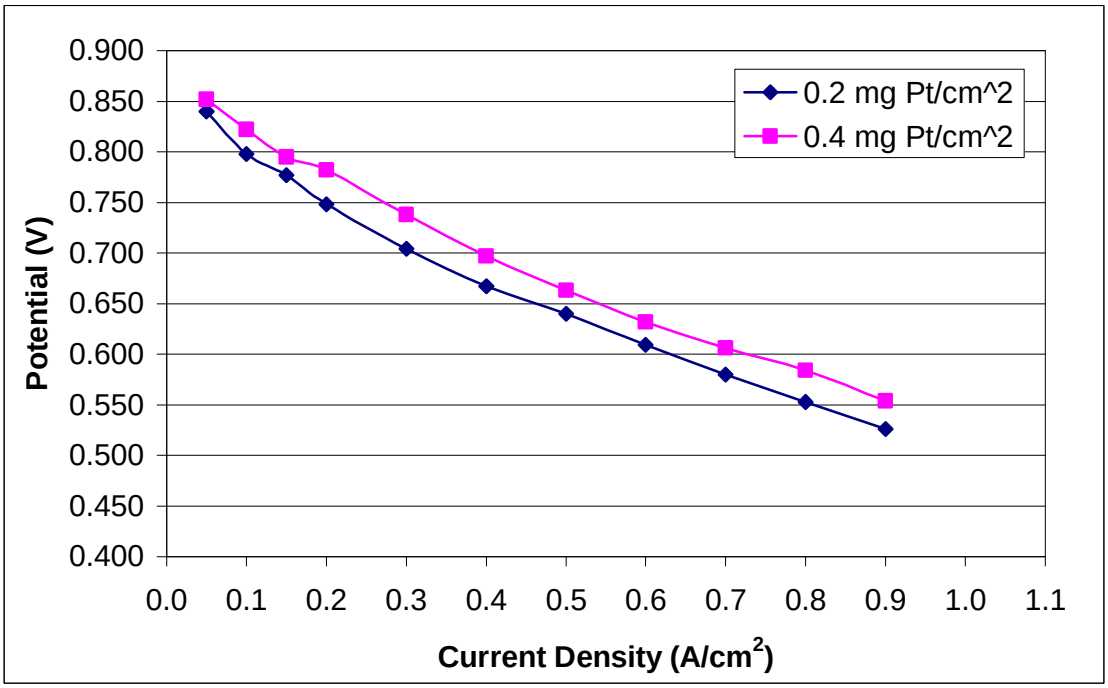

Figure 4.38: Effect of platinum loading on cell performance – cell potential(100 μm)

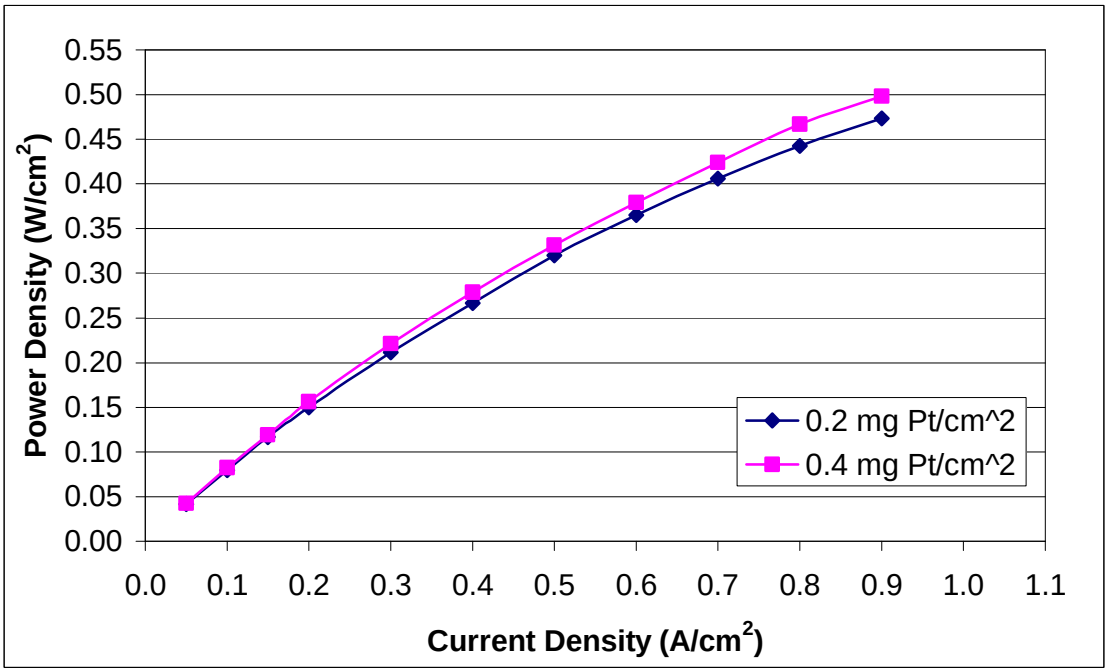

Figure 4.39: Effect of platinum loading on cell performance – power density (100 μm)

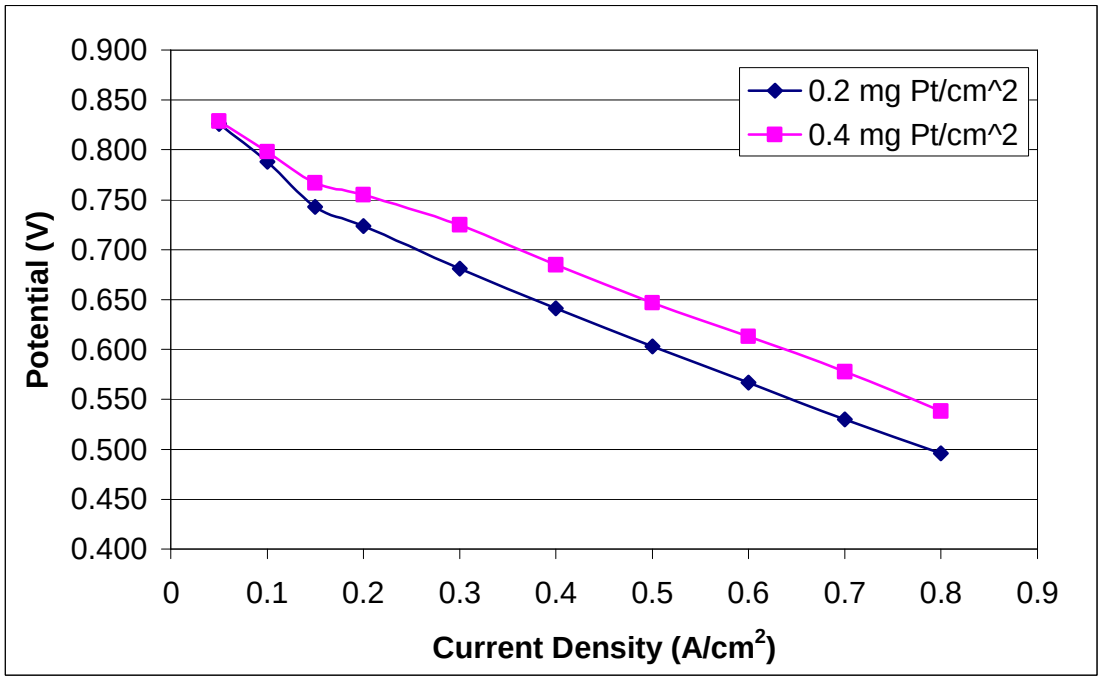

Figure 4.40: Effect of platinum loading on cell performance – cell potential(200 μm)

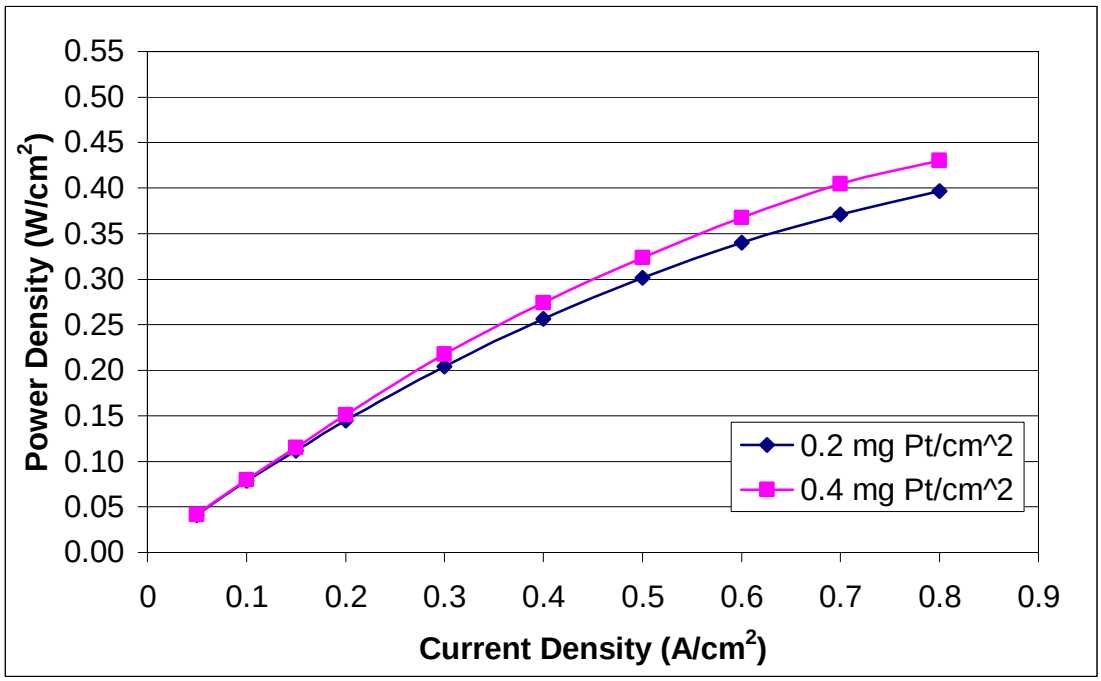

Figure 4.41: Effect of platinum loading on cell performance – power density (200 μm)

platinum loading in the catalyst layer, the control of compression can minimize the loss in performance. This once again illustrates the importance of precise compression control in a fuel cell assembly

Chapter 5
Conclusions

A significant amount of practical and analytical knowledge was gained from the study presented in this thesis. The experimental work performed allowed for development of a unique working, PEM fuel cell, skill set. This experience allowed for a great deal of growth in our lab setting, building upon existing designs and procedures to further improve our experimental techniques and fuel cell performance. This experience is not only important to the experimental studies, but offers valuable insight to be applied to our groups extensive computational models.

The faults of the five layer MEA, specifically its performance limitations was presented. It was found that the five layer construction, with the GDL fastened to the membrane electrolyte layer, was overly restrictive and fragile. Physical damage was incurred during the high compression test under normal operational conditions, which led to poor performance. Flow blockages, created by the GDL layer encroaching on the flow channel cross section, caused drastic operational pressure increases. These increases reduced the current density domain within which the cell could operate, and made extraction of meaningful performance results impossible. The lower compression configuration also revealed the shortcomings of the five layer MEA. Though the configuration displayed appropriate pressure response, the restrictive design led to GDL separation, which also resulted in poor performance results. The five layer assembly did not lend itself to the controlled compression procedure as accurate GDL measurements were unattainable. The five layer assembly was eliminated form the study.

Preliminary test results were compared to existing data from literature as well as commercially available fuel cell performance data. These comparisons revealed that the experimental cell assembly, in general, performed equal to or better than these pre-existing cells. In all cases, the experimental assembly significantly outperformed these cells in the mid to high current density region. The experimental assembly was found to perform at

sufficient level so as to provide cell potential and power density data relevant to the advancement of fuel cell research.

The compressive force exerted on the cell was varied for a number of test cell configurations, through the manipulation of applied bolt torque. The effect of this varying compression on flow and performance test results was examined. A general trend of increasing performance with increasing compression was found to exist. This trend was consistent to a peak level of performance, at which point further increases in compressive force were found to negatively impact this performance. Flow tests revealed that increases in performance were paralleled by an increase in pressure response from the cell. The increase in compression resulted in an increase in pressure drop across the flow channel. Pressure was identified as a potential causal factor in the performance behaviour of the cell, arising from changes in compression. Other causal factors, affected by compression, were identified to be changes in physical properties of the GDL, the improvement of cell sealing and surface contact, as well as both permeability and electrical conductivity. These factors and their individual effect on performance would have to be investigated.

The effect of improper sealing and surface contact on fuel cell performance was analysed. The concepts of internal and external leakages in a fuel cell were introduced and methods to limit these sources of flow losses were discussed. The gaskets and GDLs were found to be the most significant components contributing to internal losses. A comparison of varying compression experimental assemblies with a configuration designed to possess internal leakages was performed. The flow tests illustrated pressure drop results indicative of internal leakages, while performance tests revealed the significant drop in performance associated with these leakages and poor surface contact. The losses in performance were due to flow bypass, which limited the flow of reactants to the catalyst layer, and increased cell resistance, created by the increased electrical surface resistance due to poor surface contact.

Controlling compression through applied torque alone was inadequate as the ability to precisely control compression while also guaranteeing sufficient surface contact and sealing

was virtually impossible. The concept of using shims to control the thickness of the gasket and GDL layer was introduced as a precise method to control compression. The shim assemblies were compared to the conventional assembly configuration and were shown to provide comparable pressure response as well as cell potential and power density behaviour.

A model was used to analyse the pressure drop across the cathode flow channel. The pressure drop simulated by the model was found to be significantly higher than that found in the experimental cell, suggesting that the flow within the cell deviated from the flow channel path significantly. The deviation was found to be due to two factors, internal leakage and cross flow. As compression was increased pressure drop was found to increase as flow deviation was reduced. Increased compression limited flow bypass, a result of internal leakage, by closing gaps in the surface interface and forcing the flow through a path of higher resistance. Further pressure drop increase was found after the point of complete surface contact due to the reduction of cross flow. As the porous GDL was compressed, the amount of bulk motion into the GDL was reduced, again reducing the flow deviation from the flow channel. As more flow was forced through the channel, the pressure drop increased as this was the path of higher resistance. The effect of this increased pressure field on cell performance was examined. It was found that the pressure drop was merely a resultant factor of the changes in internal flow geometry and had negligible effects on cell performance.

The effect of changing porosity on cell performance, as a result of controlled GDL compression, was investigated. Compression of the GDL, resulting in reduction of porosity, would, consequently result in changes in the physical properties of that porous layer. Changes in these properties, specifically permeability and electrical conductivity, were estimated through the application of the Tomadakis correlation and the Bruggemann correction respectively. It was illustrated that compression of the GDL, and resultant reduction of porosity, would cause a significant decrease in permeability and increase in electrical conductivity. The effects of these changes in physical properties on performance were then examined. Contrary to many claims in literature of proportionality between permeability and cell performance, increased compression resulted in an increase in

performance. This was caused by the operational domain of the cell being located in the ohmic overpotential region of the polarization curve. Due to the dominance of ohmic overpotential the limiting factor in performance would be overall cell resistance and would respond more to changes in electrical conductivity than to the reduction of mass transfer. Changes in mass transfer would be a more dominant factor in the concentration polarization region. However, this relationship was found to be present only to a point, beyond which, further decreasing permeability became the limiting factor. This suggests that increasing conductivity was the dominant factor, only when sufficient permeability was maintained, greater than 10^{-12} m^2.

The effects of reduction in platinum loading on the compression related changes in performance were also examined. It was found that the decrease in performance associated with a reduction of platinum loading in the catalyst layer was found to be greater for cells that weren't optimally compressed. It was found that the cells with lower compression were more sensitive to the reduction of platinum loading. This shows that as steps are taken in future to further reduce platinum loading precision cell compression could become an even more significant factor in cell performance.

All of these conclusions reveal the importance of precision compression in fuel cell assemblies. The performance gains found in the single cell only multiply when analysed over the entire reaction surface, converting to total cell power from power density, and will multiply again when single cells are stacked in series. This meant that even small changes in power density result in significant large scale performance gains, on the order of kW.

Chapter 6
Future Work and Recommendations

This thesis presented an experimental fuel cell performance study, with emphasis on compressive effects. Though headway was made in the improvement of overall cell power production there are still areas in this field that require study.

It is recommended that this work be expanded and a more generally applicable compression relation be developed for fuel cell design purposes. In order to accomplish this further testing would be required, incorporating a larger sample of GDL constructions. The sensitivity to cell compression for a number of varying GDL compositions should be analysed, with specific attention paid to permeability and electrical conductivity. It is expected that there exists an optimal balance between these properties, which can be quantified, and would result in the peak fuel cell power performance. As a result, for a given GDL construction, one would then be able to determine the optimal degree of compression to apply.

Incorporated into these future performance studies should be experimental techniques to estimate permeability and electrical conductivity as they change with compression. This would require the development of a specific experimental assembly. The rig would require compression using a porous surface in order to allow for uniform compression while also allowing through flow, to measure permeability, and access for a four point probe measurement. As well, precision control of the compression of this assembly would be a must, with accuracy to the order of 10 μm.

Research in this field would also benefit from the development of a precision fuel cell test rig, one that would incorporate precision compression techniques. This would most likely require pneumatic actuation and precision control on the order of 10 μm.

The findings in this study, specifically the identification of conductivity as a limiting factor in fuel cell performance in its operational range can be applied to future fuel cell component design. With advancements in nano-scale constructions, GDL compositions can

be aligned to extreme precision, offering improved conductivity while limiting the impact on permeability.

Appendix A

Results Data

Data from figure 4.1:

3 layer		5 layer	
Flow Rate (sccpm)	Pressure (kPa)	Flow Rate (sccpm)	Pressure (kPa)
200	10.0	200	9.9
300	14.7	300	13.9
400	19.1	400	17.8
500	24.0	500	21.8
600	28.8	600	25.8
700	33.8	700	29.6
800	38.8	800	33.5
900	44.1	900	37.2
1000	49.5	1000	41.5
1100	54.7	1100	45.2
1200	60.2	1200	49.0
1300	65.6	1300	53.5
1400	71.1	1400	58.1
1500	76.6	1500	62.7
1600	82.2	1600	67.0
1700	87.8	1700	71.4
1800	93.4	1800	75.9
1900	99.1	1900	80.2
2000	104.7	2000	84.9
2100	110.4	2100	88.4
2200	116.1	2200	93.5
2300	121.8	2300	97.7
2400	127.6	2400	102.1
2500	133.4	2500	106.8
2600	139.2	2600	111.6
2700	145.1	2700	115.8
2800	151.0	2800	120.1
2900	156.9	2900	124.8
3000	162.9	3000	129.1

Data from figure 4.2 – 3 layer:

Time	Pressure		Time	Pressure		Time	Pressure		Time	Pressure
(min)	(kPa)		(min)	(kPa)		(min)	(kPa)		(min)	(kPa)
0	1.1		17.5	38.4		34.5	44.7		51.5	48.2
0.5	25.1		18	38.9		35	45.2		52	47.7
1	27.4		18.5	38.4		35.5	44.6		52.5	47.5
1.5	28.1		19	38.4		36	45.1		53	48.1
2	28		19.5	39.6		36.5	44.5		53.5	46.9
2.5	28.3		20	39.7		37	44.1		54	46.4
3	28.4		20.5	39.4		37.5	43.8		54.5	45.8
3.5	28.2		21	38.9		38	43.5		55	46.4
4	28.3		21.5	39.5		38.5	43.4		55.5	45.4
4.5	29.3		22	38.9		39	44.6		56	50
5	28.9		22.5	39.7		39.5	42.4		56.5	49.3
5.5	26.8		23	38.7		40	40.6		57	49.3
6	27.9		23.5	38.9		40.5	45.8		57.5	48.8
6.5	26.7		24	37.8		41	46.2		58	47.7
7	27.2		24.5	39.2		41.5	45.6		58.5	47.6
7.5	27.4		25	40.5		42	46		59	46
8	32.1		25.5	40.3		42.5	44.1		59.5	50.2
8.5	28.7		26	43.8		43	43.4		60	50.5
9	29.6		26.5	44		43.5	45.1		60.5	49.9
9.5	31.8		27	43.8		44	46.2		61	50.4
10	33.3		27.5	43.9		44.5	46		61.5	50.2
10.5	34.6		28	44.3		45	46.4		62	48.5
11	36.2		28.5	44		45.5	45.3		62.5	47.3
11.5	34.9		29	44.7		46	45.1		63	48.7
12	35.7		29.5	44.5		46.5	44.8		63.5	51.1
12.5	35.8		30	43.1		47	44.7		64	51.3
13	36.7		30.5	43.1		47.5	44		64.5	50.9
13.5	35.5		31	42.6		48	43.1		65	50.3
14	34		31.5	42.6		48.5	44.8		65.5	47.6
14.5	39.3		32	41.5		49	47.3		66	51.2
15	38.2		32.5	41.7		49.5	46.9		66.5	49.9
15.5	37.6		33	41.1		50	46.9		67	51.7
16	40.6		33.5	40.6		50.5	48.3		67.5	51.3
16.5	38		34	39.2		51	47.6		68	51.3
17	38.5									

Data from figure 4.2 – 5 layer:

Time	Pressure		Time	Pressure		Time	Pressure		Time	Pressure
(min)	(kPa)		(min)	(kPa)		(min)	(kPa)		(min)	(kPa)
0	1.4		17.5	80.4		34.5	105.4		51.5	138.6
0.5	47.4		18	79		35	111.8		52	131.6
1	47		18.5	81.6		35.5	109.3		52.5	137.6
1.5	44.6		19	80.7		36	113.5		53	139
2	47.2		19.5	82.4		36.5	108.3		53.5	137.8
2.5	46.4		20	80.3		37	116.5		54	140.6
3	43.7		20.5	81.3		37.5	107.7		54.5	137.8
3.5	47		21	79.6		38	114.1		55	145.3
4	43.5		21.5	81.7		38.5	113.9		55.5	144.9
4.5	46.8		22	89.6		39	110.9		56	142.1
5	45.7		22.5	94.7		39.5	114.8		56.5	138
5.5	48.3		23	91		40	109.9		57	143.3
6	45.5		23.5	94.4		40.5	114.4		57.5	146.1
6.5	48.2		24	89.6		41	107.4		58	144.3
7	47.1		24.5	91.3		41.5	113.4		58.5	149.2
7.5	51.2		25	88		42	122.5		59	158.3
8	53.2		25.5	92.1		42.5	121.8		59.5	154.6
8.5	50.4		26	89.3		43	125.9		60	158.3
9	55.6		26.5	92.4		43.5	120		60.5	167.5
9.5	58.4		27	87.5		44	124.8		61	154.1
10	59.9		27.5	98.4		44.5	118.1		61.5	150.8
10.5	58.3		28	98.2		45	124.7		62	149.1
11	63.3		28.5	103.7		45.5	125.2		62.5	153.4
11.5	70.4		29	103.6		46	126.3		63	144.7
12	66.4		29.5	102.7		46.5	127.8		63.5	149.7
12.5	69.9		30	104.1		47	122.6		64	156.2
13	68.6		30.5	101.4		47.5	125.2		64.5	161.9
13.5	72.5		31	102.8		48	120.5		65	165.1
14	68		31.5	104.4		48.5	132.6		65.5	165.4
14.5	70.2		32	104.9		49	138.1		66	159.9
15	68.4		32.5	101.5		49.5	139		66.5	165
15.5	71.4		33	98.9		50	138.9		67	162.6
16	77.8		33.5	101.9		50.5	137.4		67.5	165.6
16.5	81.7		34	105.4		51	136.5		68	172
17	78.1									

Data from figure 4.5:

3 layer		5 layer	
Flow Rate	Pressure	Flow Rate	Pressure
(sccpm)	(kPa)	(sccpm)	(kPa)
498.6	43.8	498.6	42
664.8	57.2	664.8	52
997.1	80.9	997.1	72.5
1329.5	102.5	1329.5	98
1661.9	124.4	1661.9	118
1994.3	148.6	1994.3	142.2
2326.7	176.3	2326.7	169.9
2659.0	198.1	2659.0	191.7

Data from figures 4.6 and 4.7:

3 Layer			5 Layer		
Current Density	Potential	Power Density	Current Density	Potential	Power Density
A/cm^2	V	W/cm^2	A/cm^2	V	W/cm^2
0.05	0.826	0.0413	0.05	0.756	0.0378
0.10	0.788	0.0788	0.10	0.69	0.069
0.20	0.724	0.1448	0.15	0.64	0.096
0.30	0.681	0.2043	0.20	0.594	0.1188
0.40	0.641	0.2564	0.30	0.517	0.1551
0.50	0.603	0.3015	0.40	0.441	0.1764
0.60	0.567	0.3402	0.50	0.368	0.184
0.70	0.530	0.3710			
0.80	0.496	0.3968			
0.90	0.464	0.4176			
1.00	0.434	0.4340			

Data from figures 4.8 and 4.9:

MacDonald			Sabir		
Current Density	Potenial	Power Density	Current Density	Potenial	Power Density
A/cm^2	V	W	A/cm^2	V	W
0.05	0.852	0.0426	0.0999	0.814	0.0813
0.10	0.822	0.0822	0.2000	0.761	0.1522
0.15	0.795	0.1193	0.3001	0.718	0.2155
0.20	0.782	0.1564	0.4000	0.650	0.2600
0.30	0.738	0.2214	0.5002	0.550	0.2751
0.40	0.697	0.2788	0.6002	0.430	0.2581
0.50	0.663	0.3315	0.7002	0.313	0.2191
0.60	0.632	0.3792			
0.70	0.606	0.4242			
0.80	0.584	0.4672			
0.90	0.554	0.4986			

Data from figures 4.10 and 4.11:

MacDonald			Nexa		
Current Density	Potential	Power Density	Current Density	Potential	Power Density
A	V	W	A	V	W
5.0	0.852	4.26	0	43.0	0.00
10.0	0.822	8.22	10	36.0	8.37
15.0	0.795	11.93	20	33.5	15.58
20.0	0.782	15.64	30	31.8	22.19
30.0	0.738	22.14	40	29.0	26.98
40.0	0.697	27.88	45	27.5	28.78
50.0	0.663	33.15			
60.0	0.632	37.92			
70.0	0.606	42.42			
80.0	0.584	46.72			
90.0	0.554	49.86			

Data from figures 4.12, 4.13, 4.19 and 4.20 – 254 μm:

53.4 kN			64.1 kN		
Current Density	Potential	Power Density	Current Density	Potential	Power Density
A/cm^2	V	W/cm^2	A/cm^2	V	W/cm^2
0.05	0.819	0.04095	0.05	0.824	0.04120
0.10	0.765	0.07650	0.10	0.770	0.07700
0.15	0.724	0.10860	0.15	0.727	0.10905
0.20	0.686	0.13720	0.20	0.695	0.13900
0.25	0.650	0.16250	0.25	0.664	0.16600
0.30	0.613	0.18390	0.30	0.634	0.19020
0.35	0.579	0.20265	0.35	0.606	0.21210
0.40	0.553	0.22120	0.40	0.578	0.23120
0.45	0.527	0.23715	0.45	0.549	0.24705
0.50	0.497	0.24850	0.50	0.530	0.26500
0.55	0.469	0.25795	0.55	0.510	0.28050
0.60	0.436	0.26160	0.60	0.490	0.29400
0.65	0.405	0.26325	0.65	0.467	0.30355
			0.70	0.445	0.31150
			0.75	0.425	0.31875
			0.80	0.411	0.32880
			0.85	0.396	0.33660
			0.90	0.368	0.33120
			0.95	0.331	0.31445
74.7 kN			85.4 kN		
Current Density	Potential	Power Density	Current Density	Potential	Power Density
A/cm^2	V	W/cm^2	A/cm^2	V	W/cm^2
0.05	0.852	0.04260	0.05	0.835	0.04175
0.10	0.825	0.08250	0.10	0.802	0.08020
0.20	0.770	0.15400	0.15	0.773	0.11595
0.30	0.728	0.21840	0.20	0.749	0.14980
0.40	0.690	0.27600	0.30	0.709	0.21270
0.50	0.653	0.32650	0.40	0.671	0.26840
0.60	0.615	0.36900	0.50	0.635	0.31750
0.70	0.578	0.40460	0.60	0.600	0.36000
0.75	0.568	0.42600	0.70	0.561	0.39270
0.80	0.560	0.44800	0.80	0.533	0.42640
0.85	0.550	0.46750	0.90	0.485	0.43650
0.90	0.537	0.48330			

Data from figures 4.15, 4.18, and 4.24 – 254 μm:

53.4 kN		64.1 kN		74.7 kN		85.4 kN	
Flow Rate	Pressure	Flow Rate	Pressure	Flow Rate	Pressure	Flow Rate	Pressure
(sccpm)	(kPa)	(sccpm)	(kPa)	(sccpm)	(kPa)	(sccpm)	(kPa)
200	4.2	200	7.4	200	11.0	200	10.9
300	6.4	300	10.5	300	15.4	300	15.4
400	8.4	400	13.7	400	19.5	400	19.4
500	10.6	500	17.0	500	24.2	500	23.9
600	12.6	600	20.3	600	28.7	600	28.1
800	16.9	700	23.6	700	33.2	700	32.3
900	19.0	800	26.9	800	38.0	800	36.8
1200	25.4	900	30.0	900	42.7	900	40.9
1400	30.4	1000	33.4	1000	47.9	1000	45.4
1600	35.1	1500	49.1	1500	73.7	1500	62.4
2000	44.6	2000	62.5	2000	100.6	2000	82.5
2500	56.8	2500	76.3	2500	128.9	2500	102.4
3000	68.4	3000	92.8	3000	156.6	3000	122.2

Data from figure 4.18 – 381 μm:

74.7 kN	
Flow Rate	Pressure
(sccpm)	(kPa)
200	4.2
300	6.4
400	8.4
500	10.6
600	12.6
800	16.9
900	19.0
1200	25.4
1400	30.4
1600	35.1
2000	44.6
2500	56.8
3000	68.4

Data from figures 4.19 and 4.20 – 381 μm:

74.7 kN		
Current Density	Potential	Power Density
A/cm^2	V	W/cm^2
0.05	0.809	0.040
0.10	0.761	0.076
0.15	0.725	0.109
0.20	0.692	0.138
0.25	0.660	0.165
0.30	0.628	0.188
0.35	0.598	0.209
0.40	0.567	0.227
0.45	0.540	0.243
0.50	0.510	0.255
0.55	0.484	0.266
0.60	0.455	0.273
0.65	0.424	0.276
0.70	0.390	0.273

Data from figure 4.21:

100 µm		150 µm		200 µm	
Flow Rate	Pressure	Flow Rate	Pressure	Flow Rate	Pressure
(sccpm)	(kPa)	(sccpm)	(kPa)	(sccpm)	(kPa)
200	11.0	200	10.7	200	10.9
300	15.4	300	15.2	300	15.4
400	19.1	400	19.0	400	19.4
500	24.0	500	23.2	500	23.9
600	28.8	600	27.6	600	28.1
700	33.8	700	32.1	700	32.3
800	38.8	800	36.7	800	36.8
900	44.2	900	41.5	900	40.4
1000	49.5	1000	46.3	1000	44.4
1500	78.0	1500	71.1	1500	62.4
2000	104.7	2000	96.8	2000	82.5
3000	162.9	2500	120.2	3000	122.2
		3000	144.0		

53.4 kN		74.7 kN	
Flow Rate	Pressure	Flow Rate	Pressure
(sccpm)	(kPa)	(sccpm)	(kPa)
200	4.2	200	11.0
300	6.4	300	15.4
400	8.4	400	19.5
500	10.6	500	24.2
600	12.6	600	28.7
800	16.9	700	33.2
900	19.0	800	38.0
1200	25.4	900	42.7
1400	30.4	1000	47.9
1600	35.1	1500	73.7
2000	44.6	2000	100.6
2500	56.8	2500	128.9
3000	68.4	3000	156.6

Data from figures 4.22 and 4.23:

74.7 kN			150 µm			200 µm		
Current Density	Potential	Power Density	Current Density	Potential	Power Density	Current Density	Potential	Power Density
A/cm^2	V	W/cm^2	A/cm^2	V	W/cm^2	A/cm^2	V	W/cm^2
0.05	0.852	0.0426	0.05	0.838	0.0419	0.05	0.829	0.0415
0.10	0.825	0.0825	0.10	0.807	0.0807	0.10	0.798	0.0798
0.20	0.770	0.1540	0.15	0.780	0.1170	0.15	0.767	0.1151
0.30	0.728	0.2184	0.20	0.765	0.1530	0.20	0.755	0.1510
0.40	0.690	0.2760	0.30	0.730	0.2190	0.30	0.725	0.2175
0.50	0.653	0.3265	0.40	0.690	0.2758	0.40	0.685	0.2740
0.60	0.615	0.3690	0.50	0.653	0.3265	0.50	0.647	0.3235
0.70	0.578	0.4046	0.60	0.620	0.3721	0.60	0.613	0.3678
0.75	0.568	0.4260	0.70	0.589	0.4120	0.70	0.578	0.4046
0.80	0.560	0.4480	0.80	0.552	0.4416	0.80	0.538	0.4304

Data from figures 4.24 and 4.25

Theoretical	
Flow Rate	Pressure
(sccpm)	(kPa)
200	8.0
300	12.8
400	18.3
500	24.6
600	31.7
700	39.6
800	48.5
900	58.3
1000	62.8
1500	114.2

Data from figure 4.25 and 4.26 :

100 µm		150 µm		200 µm	
Flow Rate	Pressure	Flow Rate	Pressure	Flow Rate	Pressure
(sccpm)	(kPa)	(sccpm)	(kPa)	(sccpm)	(kPa)
200	11.0	200	10.7	200	10.9
300	15.4	300	15.2	300	15.4
400	19.1	400	19.0	400	19.4
500	24.0	500	23.2	500	23.9
600	28.8	600	27.6	600	28.1
700	33.8	700	32.1	700	32.3
800	38.8	800	36.7	800	36.8
900	44.2	900	41.5	900	40.4
1000	49.5	1000	46.3	1000	44.4
1500	78.0	1500	71.1	1500	62.4
2000	104.7	2000	96.8	2000	82.5
3000	162.9	2500	120.2	3000	122.2
		3000	144.0		

Data from figure 4.27:

100 µm		200 µm	
Flow Rate	Pressure	Flow Rate	Pressure
(sccpm)	(kPa)	(sccpm)	(kPa)
498.6	52.0	498.6	51.1
664.8	70.4	664.8	67.4
997.1	98.8	997.1	94.5
1329.5	128.5	1329.5	120.1
1661.9	152.3	1661.9	142.9
1994.3	180.4	1994.3	169.2
2326.7	215.2	2326.7	199.1
2659.0	248.2	2659.0	232.0
2991.4	268.0	2991.4	247.3
200 µm + 10%		200 µm + 20%	
Flow Rate	Pressure	Flow Rate	Pressure
(sccpm)	(kPa)	(sccpm)	(kPa)
498.6	56.2	498.6	61.3
664.8	74.1	664.8	80.9
997.1	104.0	997.1	113.4
1329.5	132.1	1329.5	144.1
1661.9	157.2	1661.9	171.5
1994.3	186.1	1994.3	203.0
2326.7	219.0	2326.7	238.9
2659.0	255.2	2659.0	278.4
2991.4	272.0	2991.4	296.8

Data from figures 4.28-4.30:

100 µm			200 µm		
Current Density	Potential	Power Density	Current Density	Potential	Power Density
A/cm^2	V	W/cm^2	A/cm^2	V	W/cm^2
0.05	0.852	0.0426	0.05	0.829	0.0415
0.10	0.822	0.0822	0.10	0.798	0.0798
0.20	0.782	0.1564	0.15	0.767	0.1151
0.30	0.738	0.2214	0.20	0.755	0.1510
0.40	0.697	0.2788	0.30	0.725	0.2175
0.50	0.663	0.3315	0.40	0.685	0.2740
0.60	0.632	0.3792	0.50	0.647	0.3235
0.70	0.606	0.4242	0.60	0.613	0.3678
0.80	0.584	0.4672	0.70	0.578	0.4046
0.90	0.554	0.4986	0.80	0.538	0.4304
200 µm + 10%			200 µm + 20%		
Current Density	Potential	Power Density	Current Density	Potential	Power Density
A/cm^2	V	W/cm^2	A/cm^2	V	W/cm^2
0.05	0.830	0.0415	0.05	0.828	0.0414
0.10	0.800	0.0800	0.10	0.803	0.0803
0.15	0.770	0.1155	0.15	0.770	0.1155
0.20	0.756	0.1512	0.20	0.754	0.1508
0.30	0.720	0.2160	0.30	0.721	0.2163
0.40	0.686	0.2744	0.40	0.686	0.2744
0.50	0.649	0.3245	0.50	0.651	0.3255
0.60	0.614	0.3684	0.60	0.616	0.3696
0.70	0.581	0.4067	0.70	0.583	0.4081

Data from figure 4.32:

100 µm		150 µm		200 µm	
Flow Rate	Pressure	Flow Rate	Pressure	Flow Rate	Pressure
(sccpm)	(kPa)	(sccpm)	(kPa)	(sccpm)	(kPa)
200	11.0	200	10.7	200	10.9
300	15.4	300	15.2	300	15.4
400	19.1	400	19.0	400	19.4
500	24.0	500	23.2	500	23.9
600	28.8	600	27.6	600	28.1
700	33.8	700	32.1	700	32.3
800	38.8	800	36.7	800	36.8
900	44.2	900	41.5	900	40.4
1000	49.5	1000	46.3	1000	44.4
1500	78.0	1500	71.1	1500	62.4
2000	104.7	2000	96.8	2000	82.5
3000	162.9	2500	120.2	3000	122.2
		3000	144.0		

Data from figures 4.33 and 4.34:

100 µm			150 µm			200 µm		
Current Density	Potential	Power Density	Current Density	Potential	Power Density	Current Density	Potential	Power Density
A/cm^2	V	W/cm^2	A/cm^2	V	W/cm^2	A/cm^2	V	W/cm^2
0.05	0.852	0.0426	0.05	0.838	0.0419	0.05	0.829	0.0415
0.10	0.822	0.0822	0.10	0.807	0.0807	0.10	0.798	0.0798
0.20	0.782	0.1564	0.15	0.780	0.1170	0.15	0.767	0.1151
0.30	0.738	0.2214	0.20	0.765	0.1530	0.20	0.755	0.1510
0.40	0.697	0.2788	0.30	0.730	0.2190	0.30	0.725	0.2175
0.50	0.663	0.3315	0.40	0.690	0.2758	0.40	0.685	0.2740
0.60	0.632	0.3792	0.50	0.653	0.3265	0.50	0.647	0.3235
0.70	0.606	0.4242	0.60	0.620	0.3721	0.60	0.613	0.3678
0.80	0.584	0.4672	0.70	0.589	0.4120	0.70	0.578	0.4046
0.90	0.554	0.4986	0.80	0.552	0.4416	0.80	0.538	0.4304

Data from figures 4.36 and 4.37:

85.4 kN			100 µm		
Current Density	Potential	Power Density	Current Density	Potential	Power Density
A/cm^2	V	W/cm^2	A/cm^2	V	W/cm^2
0.05	0.835	0.04175	0.05	0.852	0.0426
0.10	0.802	0.08020	0.10	0.822	0.0822
0.15	0.773	0.11595	0.20	0.782	0.1564
0.20	0.749	0.14980	0.30	0.738	0.2214
0.30	0.709	0.21270	0.40	0.697	0.2788
0.40	0.671	0.26840	0.50	0.663	0.3315
0.50	0.635	0.31750	0.60	0.632	0.3792
0.60	0.600	0.36000	0.70	0.606	0.4242
0.70	0.561	0.39270	0.80	0.584	0.4672
0.80	0.533	0.42640	0.90	0.554	0.4986
0.90	0.485	0.43650			

Data from figures 4.38 and 4.39:

100 µm - 0.4 mg Pt			100 µm - 0.2 mg Pt		
Current Density	Potential	Power Density	Current Density	Potential	Power Density
A/cm^2	V	W/cm^2	A/cm^2	V	W/cm^2
0.05	0.852	0.0426	0.05	0.840	0.0420
0.10	0.822	0.0822	0.10	0.798	0.0798
0.15	0.795	0.1193	0.15	0.777	0.1166
0.20	0.782	0.1564	0.20	0.748	0.1496
0.30	0.738	0.2214	0.30	0.704	0.2112
0.40	0.697	0.2788	0.40	0.667	0.2668
0.50	0.663	0.3315	0.50	0.640	0.3200
0.60	0.632	0.3792	0.60	0.609	0.3654
0.70	0.606	0.4242	0.70	0.580	0.4060
0.80	0.584	0.4672	0.80	0.553	0.4424
0.90	0.554	0.4986	0.90	0.526	0.4734

Data from figures 4.40 and 4.41:

200 µm - 0.4 mg Pt			200 µm - 0.2 mg Pt		
Current Density	Potential	Power Density	Current Density	Potential	Power Density
A/cm^2	V	W/cm^2	A/cm^2	V	W/cm^2
0.05	0.829	0.0415	0.05	0.826	0.0413
0.10	0.798	0.0798	0.10	0.788	0.0788
0.15	0.767	0.1151	0.15	0.743	0.1115
0.20	0.755	0.1510	0.20	0.724	0.1448
0.30	0.725	0.2175	0.30	0.681	0.2043
0.40	0.685	0.2740	0.40	0.641	0.2564
0.50	0.647	0.3235	0.50	0.603	0.3015
0.60	0.613	0.3678	0.60	0.567	0.3402
0.70	0.578	0.4046	0.70	0.530	0.3710
0.80	0.538	0.4304	0.80	0.496	0.3968

Bibliography

[1] N. Zamel and X. Li. Life cycle analysis of vehicles powered by a fuel cell and by internal combustion engine for Canada. *Journal of Power Sources*, 155(2):297-310, 2006.

[2] X. Li. *Principles of Fuel Cells.* Taylor & Francis, New York, 2005.

[3] Ballard Power Systems. Ballard fuel cell power module Mark902™. Available at: http://www.ballard.com/files/pdf/Spec_Sheets/Mark902_-_SPC5000035_0D.pdf, Accessed October 14, 2008.

[4] Hydrogen Highway. Hydrogen Highway Business Plan Executive Summary. Available at: http://hydrogenhighway.ca/upload/documents/Business_Relations/HHWY_ExecSmmry_web.pdf, Accessed October 14, 2008.

[5] U.S. Department of Energy. Hydrogen, fuel cells & infrastructure technologies program: Multi-year research 2005-2015. Available at: http://www1.eere.energy.gov/hydrogenandfuelcells/mypp/, Accessed October 14, 2008.

[6] A. Rowe and X. Li. Mathematical modeling of proton exchange membrane fuel cells. *Journal of Power Sources*, 102(1-2):82-96, 2001.

[7] J. Baschuk and X. Li. A general formulation for a mathematical PEM fuel cell model. *Journal of Power Sources*, 142(1-2):134-153, 2005.

[8] X. Li and I. Sabir. Review of bipolar plates in PEM fuel cells: Flow-field designs. *International Journal of Hydrogen Energy*, 30(4):359-371, 2005.

[9] S. Litster and G. McLean. PEM fuel cell electrodes. *Journal of Power Sources*, 130(1-2):61-76, 2004.

[10] S. Gottesfeld and T. A. Zawodzinski. Polymer electrolyte fuel cells. In R. C. Alkire, H. Gerischer, D. M. Kolb and C. W. Tobias (eds.), *Advances in Electrochemical Science and Engineering Volume 5*, pages 195-301. Wiley-VCH, New York, 1997.

[11] V. A. Paganin, E. A. Ticianelli and E. R. Gonzalez. Development and electrochemical studies of gas diffusion electrodes for polymer electrolyte fuel cells. *Journal of Applied Electrochemistry*, 26(3):297-304, 1995.

[12] J. Jang, H. Chiu, W. Yan and W. Sun. Effects of operating conditions on the performances of individual cell and stack of PEM fuel cell. *Journal of Power Sources*, 180(1):476–483, 2008.

[13] Q. Yan, H. Toghiani and H. Causey. Steady state and dynamic performance of proton exchange membrane fuel cells (PEMFCs) under various operating conditions and load changes. *Journal of Power Sources*, 161(1):492–502, 2006.

[14] W. Yan, C. Chen, S. Mei, C. Soong and F. Chen. Effects of operating conditions on cell performance of PEM fuel cells with conventional or interdigitated flow field. *Journal of Power Sources*, 162(2):1157–1164, 2006

[15] I. Sabir. *Experimental investigation of proton exchange membrane fuel cell*. MASc Thesis, University of Waterloo, 2005.

[16] T. Sakai, H. Takenaka and E. Torikai. Gas Diffusion in the Dried and Hydrated Nations. *Journal of the Electrochemical Society*, 133(1):88-92, 1986.

[17] T. Sakai, H. Takenako, N. Wakabayashi, Y. Kawami and E. Torikai. Gas Permeation Properties of Solid Polymer Electrolyte (SPE) Membranes. *Journal of The Electrochemical Society*, 132(6):1328-1332, 1985.

[18] K. Broka and P. Ekdunge. Oxygen and hydrogen permeation properties and water uptake of Nafion® 117 membrane and recast film for PEM fuel cell. *Journal of Applied Electrochemistry*, 27(2):117-123, 1997.

[19] M. V. Williams, E. Begg, L. Bonville, H. R. Kunz and J. M. Fenton. Characterization of Gas Diffusion Layers for PEMFC. *Journal of the Electrochemical Society*, 151(8):A1173-A1180, 2004.

[20] T. V. Nguyen and R. E. White. A Water and Heat Management Model for Proton-Exchange-Membrane Fuel Cells. *Journal of The Electrochemical Society*, 140(8):2178-2186, 1993.

[21] K. Choi, D. Peck, C. S. Kim, D. Shin and T. Lee. Water transport in polymer membranes for PEMFC. *Journal of Power Sources*, 86(1-2):197-201, 2000.

[22] J. Larminie and A. Dicks. *Fuel Cell Systems Explained (2nd Edition)*. John Wiley and Sons Ltd., England, 2003.

[23] D. Bernardi and M. Verbrugge. A Mathematical Model of the Solid-Polymer-Electrolyte Fuel Cell. *Journal of The Electrochemical Society*, 139(9):2477-2491, 1992.

[24] G. Squadrito, G. Maggio, E. Passalacqua, F. Lufrano and A. Patti. An empirical equation for polymer electrolyte fuel cell (PEFC) behavior. *Journal of Applied Electrochemistry*, 29(12):1449-1455, 1999.

[25] S. Qu, X. Li, M. Hou, Z. Shao and B. Yi. The effect of air stoichiometry change on the dynamic behavior of a proton exchange membrane fuel cell. *Journal of Power Sources*, 185(1):302–310, 2008.

[26] S. Kim, S. Shimpalee and J.W. Van Zee. The effect of stoichiometry on dynamic behavior of a proton exchange membrane fuel cell (PEMFC) during load change. *Journal of Power Sources*, 135(1-2):110–121, 2004.

[27] H. Tawfik, Y. Hung and D. Mahajan. Metal bipolar plates for PEM fuel cell - A review. *Journal of Power Sources*, 163(2):755–767, 2007.

[28] A. S. Woodman, E. B. Anderson, K. D. Jayne and M. C. Kimble. Development of corrosion-resistant coatings for fuel cell bipolar plates. *AESF SUR/FIN '99 Proceedings*, 6:21-24, 1999.

[29] N. G. Vitale. Fluid Flow Plate for Decreased Density of Fuel Cell Assembly. *US Patent No. 5,981,098*, 1999.

[30] J. K. Neutzler. Brazed Bipolar Plates for PEM Fuel Cells. *US Patent No. 5,776,624*, 1998.

[31] J. A. Rock. Stamped Bipolar Plate for PEM Fuel Cell Stack. *US Patent No. 6,503,653*, 2003.

[32] L. G. Marianowski. Sheet Metal Bipolar Plate Design for Polymer Electrolyte Membrane Fuel Cells. *US Patent No. 6,261,710*, 2001.

[33] A. Pellegri and P. M. Spaziante. Bipolar Separator for Electrochemical Cells and Method of Preparation Thereof. *US Patent No. 4,197,178*, 1980.

[34] D. S. Watkins, K. W. Dircks and D. G. Epp. Fuel Cell Fluid Flow Field Plate. *US Patent No. 5,108,849*, 1992.

[35] D. S. Watkins, K. W. Dircks and D. G. Epp. Novel Fuel Cell Fluid Flow Field Plate. *US Patent No. 4,988,583*, 1991.

[36] N. J. Fletcher, C. Y. Chow, E. G. Pow, H. H. Wozniczka, G. H. Voss and D. P. Wilkinson. Canadian Patent No. 2,192,170, 1996.

[37] C. Cavalca, S. T. Homeyer and E. Walsworth. Flow Field Plate for Use in a Proton Exchange Membrane Fuel Cell. *US Patent No. 5,686,199*, 1997.

[38] L. Akyalcın and S. Kaytakoglu. Optimization of structural combinations on the performance of a PEMFC's MEA. *Journal of Power Sources*, 180(2):767–772, 2008.

[39] M. Amirinejad, S. Rowshanzamir and M. H. Eikani. Effects of operating parameters on performance of a proton exchange membrane fuel cell. *Journal of Power Sources*, 161(2):872–875, 2006.

[40] S. Y. Cha and W. M. Lee. Performance of Proton Exchange Membrane Fuel Cell Electrodes Prepared by Direct Deposition of Ultrathin Platinum on the Membrane Surface. *Journal of The Electrochemical Society*, 146(11):4055-4060, 1999.

[41] R. O'Hayre, S. Lee, S. Cha and F. B. Prinz. A sharp peak in the performance of sputtered platinum fuel cells at ultra-low platinum loading. *Journal of Power Sources*, 109(2):483-493, 2002.

[42] H. F. Oetjen, V. M. Schmidt, U. Stimming and F. Trila. Performance Data of a Proton Exchange Membrane Fuel Cell Using H_2/CO as Fuel Gas. *Journal of The Electrochemical Society* 143(12):3838-3842, 1996.

[43] V. M. Schmidt, H. F. Oetjen and J. Divisek. Performance Improvement of a PEMFC Using Fuels with CO by Addition of Oxygen-Evolving Compounds. *Journal of The Electrochemical Society* 144(9):L237-L238, 1997.

[44] T. A. Zawodzinski, C. Karuppaiah, F. Uribe and S. Gottesfeld. Aspects of CO tolerance in polymer electrolyte fuel cells: some experimental findings. In S. Srinivasan, J. McBreen, A. C. Khandkar and V. C. Tilak (eds), *Electrode Materials and Processes for Energy Conversion and Storage IV*, Proceedings of the Electrochemical Society, vol. 97-13: pages 139-146, The Electrochemical Society, Inc.: Pennington, 1997.

[45] J. Baschuk and X. Li. Carbon monoxide poisoning of proton exchange membrane fuel cells. *International Journal of Energy Research*, 25(8):695-713, 2001.

[46] S. Gottesfeld and J. Pafford. A New Approach to the Problem of Carbon Monoxide Poisoning in Fuel Cells Operating at Low Temperatures. *Journal of The Electrochemical Society*, 135(10):2651-2652, 1988.

[47] V. M. Schmidt, R. Ianneillo, H. F. Oetjen, H. Reger, U. Stimming, F. Trila. Oxidation of H_2/CO in a Proton Exchange Membrane Fuel Cell. In S. Gottesfeld, G. Halpert and A. Landgrebe (eds), *Proton Conducting Membrane Fuel Cells I*, Electrochemical Society Proceedings, vol. 95-23: pages 1-11, The Electrochemical Society, Inc.: Pennington, 1995.

[48] J. T. Gostick, M. W. Fowler, M. D. Pritzker, M. A. Ioannidis and L. M. Behra. In-plane and through-plane gas permeability of carbon fiber electrode backing layers. *Journal of Power Sources*, 162(1):228–238, 2006

[49] J. P. Feser, A. K. Prasad and S. G. Advani. Experimental characterization of in-plane permeability of gas diffusion layers. *Journal of Power Sources*, 162(2):1226–1231, 2006.

[50] A. Fischer, J. Jindra and H. Wendt. Porosity and catalyst utilization of thin layer cathodes in air operated PEM-fuel cells. *Journal of Applied Electrochemistry*, 28(3):277-282, 1998.

[51] M. S. Wilson, J. A. Valerio and S. Gottesfeld. Low platinum loading electrodes for polymer electrolyte fuel cells fabricated using thermoplastic ionomers. *Electrochimica Acta*, 40(3):355-363, 1995.

[52] L. R. Jordan , A. K. Shukla, T. Behrsing , N. R. Avery , B. C. Muddle and M. Forsyth. Diffusion layer parameters influencing optimal fuel cell performance. *Journal of Power Sources*, 86(1-2):250–254, 2000.

[53] Z. Qi and A. Kaufman. Improvement of water management by a microporous sublayer for PEM fuel cells. *Journal of Power Sources*, 109(1):38-46, 2002.

[54] G. Lin and T. V. Nguyen. Effect of Thickness and Hydrophobic Polymer Content of the Gas Diffusion Layer on Electrode Flooding Level in a PEMFC. *Journal of The Electrochemical Society*, 152(10):A1942-A1948, 2005.

[55] F. Lufrano, E. Passalacqua, G. Squadrito, A. Patti and L.Giorgi. Improvement in the diffusion characteristics of low Pt-loaded electrodes for PEFCs. *Journal of Applied Electrochemistry*, 29(4):445-448, 1999.

[56] L. Giorgi, E. Antolini, A. Pozio and E. Passalacqua. Influence of the PTFE content in the diffusion layer of low-Pt loading electrodes for polymer electrolyte fuel cells. *Electrochimica Acta*, 43(24):3675-3680, 1998.

[57] M. M. Tomadakis and T. J. Robertson. Viscous Permeability of Random Fiber Structures: Comparison of Electrical and Diffusional Estimates with Experimental and Analytical Results. *Journal of Composite Materials*, 39(2):163-188, 2005.

[58] M. Barber, T. S. Sun, E. Petrach, X. Wang and Q. Zou. Contact mechanics approach to determine contact surface area between bipolar plates and current collector in proton exchange membrane fuel cells. *Journal of Power Sources*, 2008, doi:10.1016/j.jpowsour.2008.08.091

[59] W. R. Chang, J. J. Hwang, F. B. Weng and S. H. Chan. Effect of clamping pressure on the performance of a PEM fuel cell. *Journal of Power Sources*, 166(1):149–154, 2007.

[60] Z. Y. Su, C. T. Liu, H. P. Chang, C. H. Li, K. J. Huang and P. C. Sui. A numerical investigation of the effects of compression force on PEM fuel cell performance. *Journal of Power Sources*, 183(1):182–192, 2008.

[61] I. Nitta, T. Hottinen, O. Himanen and M. Mikkola. Inhomogeneous compression of PEMFC gas diffusion layer Part I. Experimental. *Journal of Power Sources*, 171(1):26-36, 2007.

[62] T. Hottinen, O. Himanen, S. Karvonen and I. Nitta. Inhomogeneous compression of PEMFC gas diffusion layer Part II. Modeling the effect. *Journal of Power Sources*, 171(1):113–121, 2007.

[63] P. Zhou, C. W. Wu. Numerical study on the compression effect of gas diffusion layer on PEMFC performance. *Journal of Power Sources*, 170(2):93–100, 2007.

[64] W. Lee, C. Ho, J. W. Van Zee and M. Murthy. The effects of compression and gas diffusion layers on the performance of a PEM fuel cell. *Journal of Power Sources*, 84(1):45–51, 1999.

[65] J. Ge, A. Higier and H. Liu. Effect of gas diffusion layer compression on PEM fuel cell performance. *Journal of Power Sources*, 159(2):922–927, 2006.

[66] J. W. Park and X. Li. An experimental and numerical investigation on the cross flow through gas diffusion layer in a PEM fuel cell with a serpentine flow channel. *Journal of Power Sources*, 163(2):853–863, 2007.

[67] H. H. Voss and C. Y Chow. Coolant Flow Field Plate for Electrochemical Fuel Cells. *US Patent No. 5,230,966*, 1993.

[68] F. Cverna and S. D. Bagdade. *ASM Ready Reference: Thermal Properties of Materials*. ASM International, Ohio, 2002.

[69] Hydrogenics. *FCATS S-Series User Guide: Version 1.0*. Hydrogenics Inc., Mississauga, 2003.

[70] Ballard Power Systems. *Nexa™ (310-0027) Power Module User's Manual*. Ballard Power Systems Inc., Canada, 2003.

[71] F. M. White. *Fluid Mechanics: Fifth Edition*. McGraw-Hill, New York, 2003.

[72] S. Maharudrayya, S. Jayanti and A. P. Deshpande. Pressure losses in laminar flow through serpentine channels in fuel cell stacks. *Journal of Power Sources*, 138(1-2):1–13, 2004.

[73] D. L. Johnson, J. Koplik and L. M. Schwartz. New Pore-Size Parameter Characterizing Transport in Porous Media. *Physical Review Letters*, 57(20):2564-2567, 1986.

[74] H. Li, Y. Tang, Z. Wang, Z. Shi, S. Wu, D. Song, J. Zhang, K. Fatih, J. Zhang, H. Wang, Z. Liu, R. Abouatallah, A. Mazza. A review of water flooding issues in the proton exchange membrane fuel cell. *Journal of Power Sources*, 178(1):103–117, 2008.